UNIVERSIDAD POLITÉCNICA DE MADRID
Escuela Técnica Superior de Ingenieros de Telecomunicación

Applications of Graphene and 2D materials in supercapacitors: from large area to nano and from rigid to flexible devices

DOCTORAL THESIS

Submitted for the degree of Doctor by:

Assia Hamada

Master's Degree in Material Physics

Madrid, 2024


UNIVERSIDAD POLITÉCNICA DE MADRID
Escuela Técnica Superior de Ingenieros de Telecomunicación

Doctoral Degree in Electronic Systems Engineering

Applications of Graphene and 2D materials in supercapacitors: from large area to nano and from rigid to flexible devices

DOCTORAL THESIS

Submitted for the degree of Doctor by:

Assia Hamada

Master's Degree in Material Physics

Under the supervision of:
Dr. Javier Martínez Rodrigo
Dra. Yu Kyoung Ryu

Madrid, 2024

Title: Applications of Graphene and 2D materials in supercapacitors: from large area to nano and from rigid to flexible devices.

Author: Assia Hamada

Doctoral Programme: Electronic Systems Engineering

Thesis Supervision:

Dr. Javier Maritnez Rodrigo. Associate Professor. Department of Material Science. ETSICCP. Polytechnic University of Madrid. (Supervisor)

Dr.Yu Kyoung Ryu. Assistant Professor. Department of Applied Physics and Material Engineering.. ETSII. Polytechnic University of Madrid. (Co-supervisor)

External Reviewers:

Thesis Defense Committee:

Thesis Defense Date:

I dedicate this humble work to the pure soul of my grandmother Aicha Hamada,
who left us just a few days ago.

Acknowledgment

In the name of Allah, the Most Gracious and Merciful. Firstly, I am grateful to Almighty Allah for granting me the strength, knowledge, and ability to embark on and complete this study.

My sincere gratitude to all those who have supported and guided me throughout my academic journey, particularly in the culmination of this doctoral work, which signifies a significant milestone in my research. This journey has not only been about academic achievements but also personal growth and transformation. I am immensely thankful to my esteemed supervisors, Dr. Javier Martínez and Dr. Yu Kyoung Ryu, for their invaluable guidance, unwavering support, and insightful feedback during the research process. Their expertise, patience, and encouragement have been pivotal in shaping the direction and quality of this work. I am grateful for their willingness to share their knowledge, experience, and dedication to my success.

I extend my heartfelt appreciation to the members of my doctoral committee, Dr. Javier Grandal Quintana, Dr. María Belen Gómez Mancebo, and Dr. María Ángela Pampillón Arce, for generously dedicating their time, sharing their expertise, and providing constructive feedback that significantly enriched the content and bolstered the academic rigor of this thesis. Their invaluable insights and suggestions have played a crucial role in ensuring the excellence of this work.

I am indebted to the Algerian Ministry of Higher Education and Scientific Research for providing financial support throughout my PhD journey via the PhD Training Abroad scholarship program 2020-2023. I also extend my gratitude to the Algerian embassy in Madrid for their invaluable assistance and support.

To all members of the ISOM family, I express my gratitude and respect. Thank you for your warm smiles and greetings whenever we cross paths. To Prof. Fernando Calle, I express my gratitude and respect for your moral support towards my Algerian colleagues and me each time we encountered you and for your patience,

as I attempted to converse with you in Spanish despite my numerous mistakes. Montse, Fernando, Oscar, Manu, and Jesus, I thank you for your assistance in resolving administrative and laboratory issues and ensuring smooth operations. Special appreciation goes to my colleague, Dr. Andres Velasco, for training me during my first year and providing unwavering assistance throughout my academic journey. To my office mates Alejandro, Amalia, Jesus, Jovana, Malte, Laura, Lazar, and Nuño I am thankful for fostering a friendly atmosphere and positive energy and vibes.

To my Algerian colleagues at ISOM—Chahinaz, Hana, Serine, and Zahia—and Asma, thank you for your support, knowledge sharing, and valuable advice. With all my best wishes for you to succeed in your life.

I extend my sincere gratitude and thanks to my family, especially my parents. Your unwavering support and belief in me have been my driving force. Thank you, Father, for your strict guidance and for reminding me everywhere and every time that you would not accept anything but seeing me as a doctor. I hope my success brings you and my mother immense happiness and pride.

Finally, I extend my gratitude to all who have supported and inspired me along this journey, whether through encouragement, mentorship, or friendship. Your contributions have been immeasurable and deeply appreciated. I am grateful for your support and encouragement as we journeyed together.

Assia

"*I'd put my money on the sun and solar energy. What a source of power! I hope we don't have to wait until oil and coal run out before we tackle that. I wish I had more years left.*"

Thomas Edison, 1920.

".... sun does not shine during the night, wind does not blow on demand, and we all expect to drive our car with at least a few hours of autonomy, energy storage systems are starting to play a larger part in our lives."

Patrice Simon & Yury Gogotsi, 2008.

Abstract

Supercapacitors, also known as ultracapacitors or electrochemical capacitors, have emerged as a promising energy storage technology of considerable significance in shaping the trajectory of future energy storage systems. They offer distinct advantages, including exceptionally high-power density compared to conventional batteries, rapid charging and discharging capabilities, prolonged cycle life, efficient energy storage, and temperature resistance. These attributes position them as a definitive contender for future energy storage solutions.

The first successful isolation of graphene by Andre Geim and Konstantin Novoselov which allowed them to win the Nobel Prize in Physics in 2010. Graphene, hailed as a two-dimensional (2D) "Wonder Material," exhibits an array of extraordinary properties that include high electrical and thermal conductivity, remarkable mechanical strength, transparency, and biocompatibility. These qualities have spurred a diverse range of potential applications, with particular emphasis on energy storage, especially in the realm of our study on supercapacitors. However, challenges persist in the mass production of graphene and its cost-effectiveness, impeding the material's development at the commercial level. Various methods exist for synthesizing graphene, each of which presents distinct trade-offs in terms of cost, scalability, quality, and quantity.

The present doctoral research investigates the application of direct laser writing (DLW) as a novel method for graphene synthesis, encompassing laser-induced graphene (LIG) and laser-reduced graphene oxide (LrGO) techniques. In these approaches, we settle on infrared (IR) laser technology and Kapton polymid as precursors to fabricate graphene microsupercapacitor (MSC) electrodes through modulation of laser parameters and variation of Kapton polymer thickness, and through ultraviolet (UV) and IR laser reduction of graphene oxide (GO) to demonstrate the efficacy of LrGO in energy storage applications.

The first phase of the research focusses on the synthesis of rigid LIG-based MSCs through controlled IR laser ablation of Kapton polymer adhesive substrates with a thickness of 60 μm. This process yields porous graphene-like structures with

notable surface area. Varying laser parameters, including power, scan speed, and fluence, results in MSC electrodes characterized by remarkable electrical conductivity and surface morphology, culminating in robust electrochemical properties within MSC devices.

The second phase involves the transition from rigid to flexible MSCs by modifying the PI thickness to 125 μm and employing a non-adhesive polymer. Emphasis is placed on the impact of the laser pass count on flexible MSC performance. Multi-pass laser treatment unveils possibilities for enhanced LIG quality, underscoring the potential to amplify the electrochemical efficacy of bendable MSCs with minor laser parameter adjustments.

As a complement and an improvement to the results obtained in the previous part, the third phase consists of the integration of indium selenide (InSe) nanosheets prepared using liquid phase exfoliation (LPE) on LIG as a doping strategy to improve the overall performance of the flexible LIG MSC devices. Precise patterning and deposition techniques facilitate the incorporation of these materials.

This strategic incorporation of 2D materials holds promise for elevating electrode quality and increasing the LIG specific surface area (SSA) thus increasing MSC device functionality.

Within the framework of the REGRAP-2D project, an alternative laser direct writing technique, LrGO, employing GO as a precursor, was evaluated along with other thermal reduction processes. Notably, laser reduction methods possess a distinctive advantage in enabling intricate patterning on thin films with arbitrary geometries, epitomizing precision, and high resolution. With its shallow penetration depth and localized effects, we demonstrated that this technique is ideally suited for flexible and miniaturized devices in micro- and nanoelectronic applications, including flexible MSCs.

In conclusion, this doctoral thesis presents an investigation of the integration of laser direct writing of both types of LIG and LrGO. And LPE 2D-InSe material to advance in the production of MSCs, as facile, scalable, and low-cost methods, spanning from rigid to flexible configurations. The research not only showcases the potential of these advanced materials in improving energy storage performance,

but also provides a roadmap for the design and fabrication of adaptable, high-performance MSC devices for diverse applications ranging from microelectronics to wearable technologies.

Resumen

Los supercondensadores, también conocidos como “ultra condensadores” o condensadores electroquímicos, han surgido como una prometedora tecnología de almacenamiento de energía de considerable importancia en la configuración de la trayectoria de los futuros sistemas de almacenamiento de energía. Ofrecen ventajas distintivas, incluida una potencia excepcionalmente alta en comparación con las baterías convencionales, capacidades de carga y descarga rápidas, vida útil prolongada, densidad de energía eficiente y buena resistencia a temperaturas. Estos atributos los posicionan como contendientes definitivos para futuras soluciones de almacenamiento de energía.

La primera exitosa aislación del grafeno por Andre Geim y Konstantin Novoselov les permitió ganar el Premio Nobel de Física en 2010. El grafeno, aclamado como un "Material Maravilloso" bidimensional (2D), exhibe una serie de propiedades extraordinarias que abarcan alta conductividad eléctrica y térmica, notable resistencia mecánica, transparencia y biocompatibilidad. Estas cualidades han impulsado una amplia gama de aplicaciones potenciales, con un énfasis particular en el almacenamiento de energía, especialmente en el ámbito de nuestro estudio sobre supercondensadores. Sin embargo, persisten desafíos en la producción en masa del grafeno y su rentabilidad, lo que obstaculiza el desarrollo del material a nivel comercial. Existen diversos métodos para sintetizar el grafeno, cada uno presentando compromisos distintos en términos de coste, escalabilidad, calidad y cantidad.

La presente tesis doctoral investiga la aplicación de la escritura directa con láser (direct laser writing (DLW)) como un método novedoso para la síntesis de grafeno, que abarca las técnicas de grafitización inducida por láser (Laser Induced Graphene (LIG)) y reducción de óxido de grafeno por láser (Laser reduced Graphene Oxide (LrGO)). En estos enfoques, optamos por la tecnología láser de IR y el polímero Kapton (PI) como precursores para fabricar electrodos de microsupercondensadores (MSCs) basados en grafeno mediante la modulación de parámetros láser y la variación del grosor del PI, y la reducción de óxido de grafeno

(GO) mediante láser UV y láser de IR para demostrar la eficacia de LrGO en aplicaciones de MSCs.

La primera fase de la investigación se centra en la síntesis de MSCs basados en LIG mediante la ablación controlada con láser de IR de sustratos adhesivos de PI con un grosor de 60 μm. Este proceso produce estructuras porosas similares al grafeno con una notable área superficial. Variar los parámetros láser, incluida la potencia, la velocidad de escaneo y la fluencia, da como resultado electrodos de MSCs caracterizados por una notable conductividad eléctrica y morfología superficial, lo que culmina en propiedades electroquímicas robustas dentro de dispositivos MSCs.

La segunda fase implica la transición de MSCs rígidos a flexibles mediante la modificación del grosor del PI a 125 μm y el uso de un polímero no adhesivo. Se hace hincapié en el impacto del número de pasadas láser en el rendimiento de los MSCs flexibles. El tratamiento láser de múltiples pasadas revela posibilidades para mejorar la calidad de LIG, destacando el potencial para amplificar la eficacia electroquímica de los MSCs flexibles con ajustes menores en los parámetros láser.

Como complemento y mejora de los resultados obtenidos en la parte anterior, la tercera fase consiste en la integración de láminas de seleniuro de indio (InSe) preparadas mediante exfoliación en fase líquida (liquid phase exfoliation (LPE)) sobre LIG para fabricar dispositivos de MSCs como estrategia de dopaje. Técnicas de escritura láser y deposiciones precisas facilitan la incorporación de estos materiales. Esta incorporación estratégica de materiales 2D promete elevar la calidad de los electrodos y, por lo tanto, aumentar la funcionalidad de los dispositivos MSCs.

En el marco de una colaboración del proyecto REGRAP-2D, se evaluó una técnica alternativa de escritura directa con láser, LrGO, empleando GO como precursor, junto con otros procesos de reducción térmica. Es importante destacar que los métodos de reducción con láser poseen una ventaja distintiva al permitir un patrón intrincado en películas delgadas con geometrías arbitrarias, lo que ejemplifica alta precisión y resolución. Con su poca profundidad de penetración y efectos localizados, se demostró que esta técnica es ideal para dispositivos flexibles y

miniaturizados en aplicaciones micro- y nanoelectrónicas, incluidos los MSCs flexibles.

En conclusión, esta tesis doctoral presenta una investigación sobre la integración de la escritura directa con láser de ambos tipos de LIG y LrGO. Y materiales 2D-InSe LPE para avanzar en la producción de dispositivos MSCs, como métodos fáciles, escalables y de bajo costo, que abarcan desde configuraciones rígidas hasta flexibles. La investigación no solo muestra el potencial de estos materiales avanzados para mejorar el rendimiento del almacenamiento de energía, sino que también proporciona una hoja de ruta para el diseño y la fabricación de dispositivos MSCs adaptables y de alto rendimiento para diversas aplicaciones que van desde la microelectrónica hasta las tecnologías ponibles.

Table of Contents

List of Figures

List of Tables

Abbreviations and Acronyms

2D	Two dimensional
3D	Three dimensional
AFM	Atomic force microscopy
Aluminene	2D aluminum
APCVD	Atmospheric pressure CVD
Ar	Argon
BET	Brunauer–Emmett–Teller
Borophene	2D boron
CIEMAT	Centro de investigaciones energéticas, medioambientales, and tecnológicas
CO_2	Carbon dioxide
CTB	Centro de Tecnología Biomédica
CV	Cyclic voltammetry
CVD	Chemical vapor deposition
CW	Continuous-wave laser
DLW	Direct laser writing
EDLCs	Electric double-layer capacitors
EES	Electrochemical energy storage
EIS	Electrochemical impedance spectroscopy
FeOOH	Ferric oxyhydroxide
FETs	Field effect transistors
FWHM	Full width at half maximum
GCD	Galvanostatic charge-discharge

Germanene	2D germanium
GO	Graphene oxide
hBN	Hexagonal boron nitride
Ils	Ionic liquids
Indiene	2D indium
InSe	Indium selenide
IOTs	Internet of things
IPA	Isopropyl alcohol
IR	Infrared
ISOM	Instituto de sistemas optoelectrónics y microtecnología
LIG	Laser-induced graphene
LPCVD	Low-pressure CVD
LPE	Liquid phase exfoliation
LrGO	Laser-reduced graphene oxide
MnO_2	Manganese dioxide
MoS_2	Molybdenum disulfide
MSC	Microsupercapacitor
N_2	Nitrogen
NMP	N-methylpyrrolidone
O_2	Oxygen
OCGs	Oxygen-containing groups
PAN	Polyacrylonitrile
PANI	Polyaniline
PDMS	Polymethylsiloxane
PECVD	Plasma-enhanced CVD

PEG	Polyethyelene glycol
PET	Polythylene terephthalate
PI	Polyimide
PMMA	Polymethyl methacrylate
PVA	Poly (vinyl alcohol)
PVDF	Poly (vinylidene fluoride)
PVP	Polyvinylpyrrolidone
SDBs	Sodium dodecylbenzene sulfonate
SDGs	Sustainable development goals
SEM	Scanning electron microscopy
Silicine	2D silicon
SiO_2	Silicon dioxide
SSA	Specific surface area
STM	Scanning tunnelling microscopy
tc	Charging time
TCVD	Thermal CVD
td	Discharging time
TEM	Transmission electron microscope
TMDs	Transition metal dichalcogenides
UPM	Universidad politécnica de Madrid
UV	Ultraviolet
WSe_2	Tungsten diselenide
XPS	X-ray photoelectron spectroscopy
XRD	X-ray diffraction
Π	Pi

σ	Sigma

1. Introduction

The need for efficient energy storage systems has become essential in a world struggling with climate change, the decrease in fossil fuel resources, and a continuously growing population that increases the energy demand, for example by mid-year 2023, the global population density had exceeded 8 billion people [1] (Figure 1.1.a), this leads to an increase in electricity consumption by 2,2% [2], on the other hand, according to the Statistical Review of World Energy, June 2023 [3] 80% of global energy sources are non-renewable and environmentally harmful, as shown in Figure 1.1.b, which contradicts the Sustainable Development Goals (SDGs) number 7, 11, and 13 which aim to use affordable and clean energy sources to obtain sustainable cities and clean climate (Figure 1.1.c) [4], this makes us think of relying more on renewable and green energy sources such as solar cells and wind power across various industries, including construction, telecommunications, transportation, and more, however, this environmentally friendly energy generation remains intermittent since the sun does not shine at night, and the wind does not blow everywhere and at all times [5], hence it is becoming increasingly evident that there is a need for efficient and high-performance energy storage systems which plays a crucial role in achieving long-term sustainable energy solutions, as it has the potential to extract and store energy from renewable sources for future consumption and help to bridge the gap between energy generation and utilization by ensuring a stable and consistent energy supply [6][7].

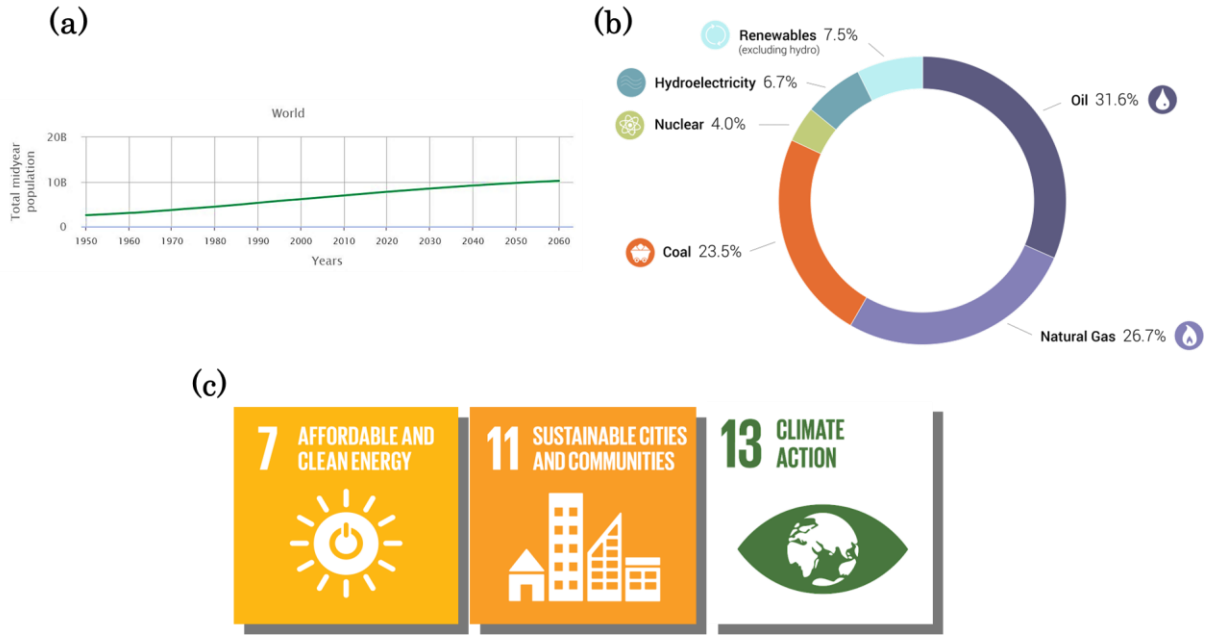

Figure 1.1: (a) Global population density by mid-year 2023 [1], (b) statistical analysis of worldwide energy sources [3], (c) SDG 7, 11, and 13 of the United Nations [4].

Energy storage systems have numerous types, which involve electrochemical, mechanical, chemical, hybrid, and thermal approaches; among these types of electrochemical energy storage (EES) devices, they are the most widely used energy storage systems due to their high suitability for future applications due to their efficiency, minimized environmental impact, lightweight, flexibility and stretchability, and cost-effectiveness [8], as shown in Figure 1.2

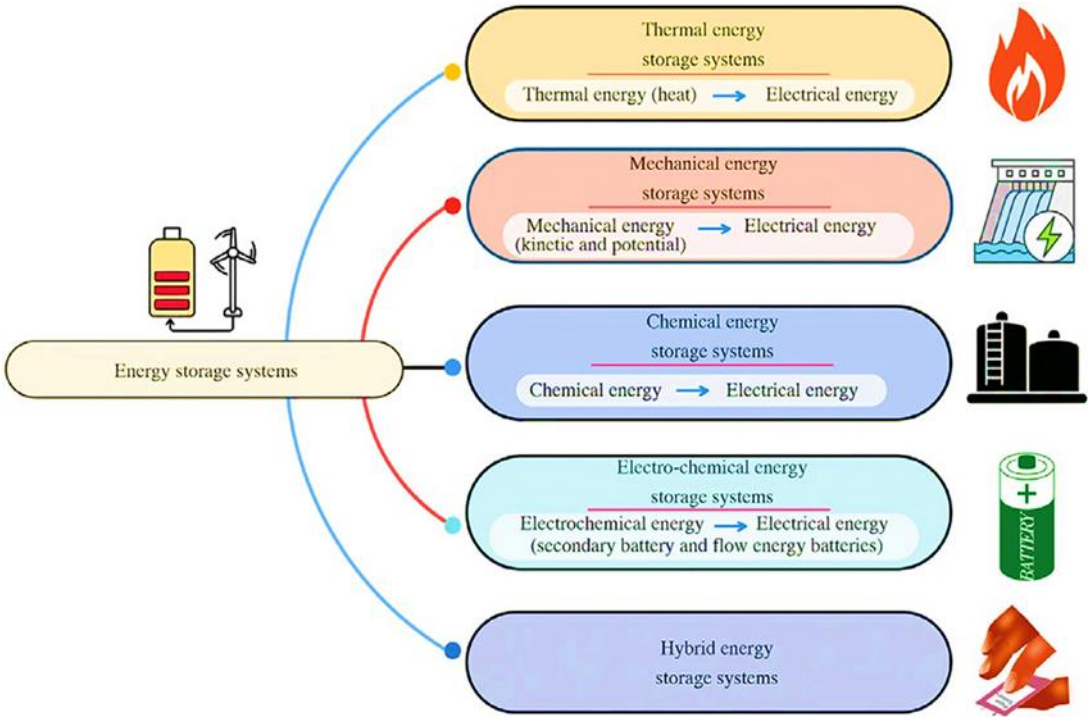

Figure 1.2: Categorization of key energy storage systems [8].

Figure 1.3 presents a Ragone plot, a graphical representation that provides a visual analogy of the power density versus the energy density of different EES systems, including fuel cells, batteries, supercapacitors, and capacitors. Fuel cells and batteries boast the highest energy density but the lowest power density, whereas supercapacitors and capacitors exhibit the highest but lowest energy density. Fuel cells exhibit advantages such as high energy conversion efficiency, low pollution emissions, long lifetime in the case of solid oxide fuel cells, noiseless operation, and versatility. However, they face challenges related to hydrogen storage, high fabrication costs, slower start-up times compared to batteries, and degradation over time. Batteries offer portable power and high energy density but have several limitations, such as limited cycle life, long charging period, environmental impact, weight and size limiting factors, and chemical dangers.

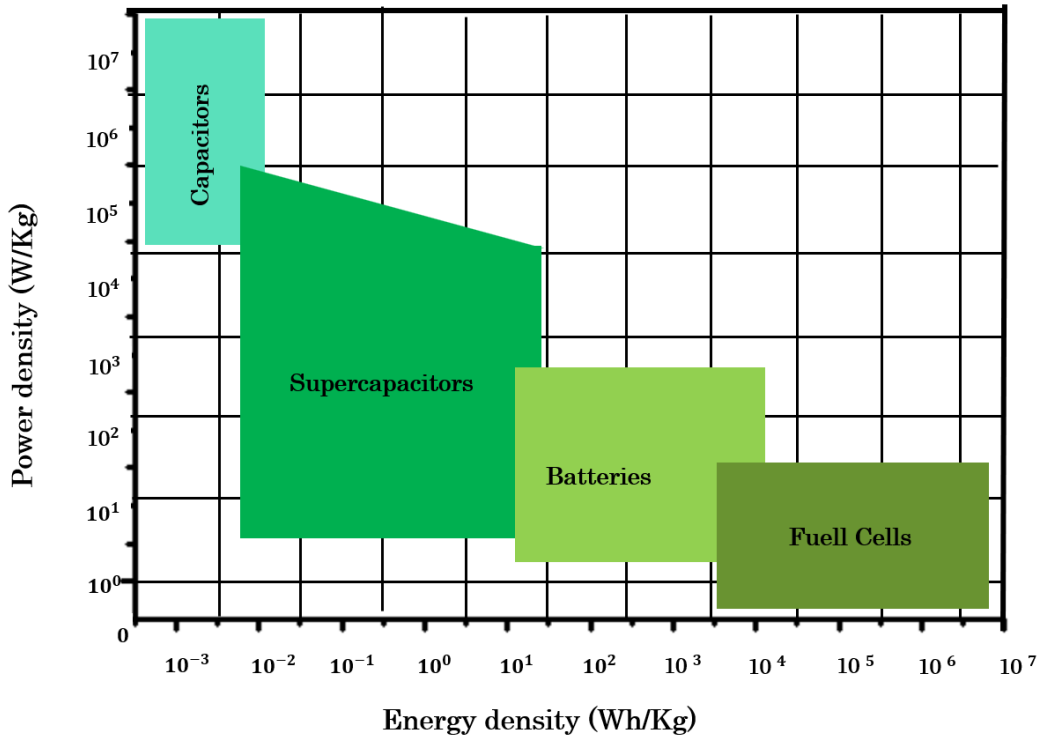

Figure 1.3: Ragone plot representing the power density versus the energy density of various electrochemical energy storage systems.

Capacitors have fast charging and discharge rates, long cycle life, and low maintenance requirements. However, they also have limitations, such as lower energy density compared to other energy storage devices, such as batteries, voltage limitations, and the necessity for high-voltage components to store significant energy. Supercapacitors are an upgraded generation of capacitors that bridge the gap between capacitors and batteries by providing rapid charging and discharging, long service life, low maintenance, affordability, reliability, and green qualities. The main drawback of supercapacitors, in comparison to batteries and fuel cells, is their insufficient energy density. Electric double-layer capacitors (EDLCs) are a type of supercapacitors that typically have an energy density of less than 10 Wh/kg, while even pseudocapacitors and hybrid capacitors (two other MSC types)generally have energy densities of less than 50 Wh/kg, which is insufficient to meet the increasing demand for applications that require high energy density. To address the challenge of limited resources.

The energy storage capacity in supercapacitors has been extensively investigated, and extensive research has focused on developing electrode materials that have high capacitance and electrolytes that can support a wider range of voltages. Furthermore, researchers are exploring new structures for integrated systems, as well as optimizing the types and thicknesses of current collectors and separators [9]. In this work, we aim to investigate high-quality electrode structures. We will focus on improving the electrode material and studying its influence on device performance, while ensuring the electrolyte, separator, and current collector types are fixed as crucial supercapacitor components.

The discovery and exploration of two-dimensional materials, particularly graphene, have revolutionized energy storage research, which is a single layer of carbon atoms arranged in a hexagonal lattice that exhibits remarkable electrical, mechanical, and thermal properties. Its exceptional conductivity, large surface area, and atomic thickness make it a compelling candidate for several applications such as environment, biomedical, sensors, and energy of our interest, where graphene shows a great impact in improving the performance of supercapacitor devices when used as electrodes see Figure 1.4 [10].

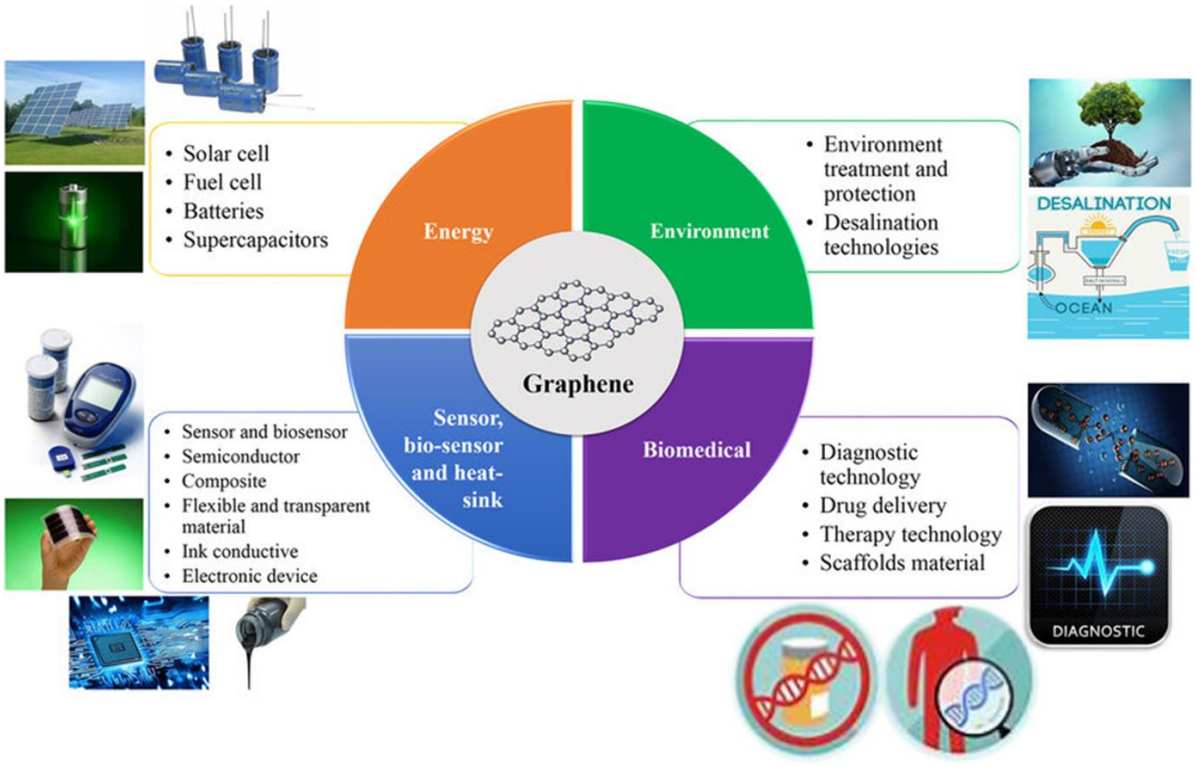

Figure 1.4: Application of graphene in scientific exploration and industrial sectors [10].

Graphene has several synthesis methods, and in this work, we adopted the DLW technique as a powerful tool and a single fabrication step to produce graphene-like materials with no requirement for masks, expensive materials, post-processing, and cleanroom operations; it is based on natural precursor, inexpensive, abundant, and biodegradable; this process is facile, rapid, cost-effective, and offers a flexible patterning; it is versatile for several applications (MSCs, sensors, field effect transistors (FETs), hologram, and water purification…), this technique is divided into two main types Laser-induced graphene when we use any carbon source as a precursor, and Laser-reduced graphene oxide when we use GO as a precursor.

The general objective of this thesis is to enhance the performance of MSCs using graphene-like electrodes fabricated by the LIG technique. I started fabricating low-cost, high-performance, and rigid MSCs first, this step was an introduction and training that made me learn how to use the laser and understand more about how to control its parameters and their effect on the resulting material structure and quality, following I aimed to upgrade our devices by maintaining the same fabrication cost and enhancing their performance more and shifting from rigid to flexible devices because flexible MSCs have a broad range of applications in flexible and wearable electronics, power sensors, and the healthcare industry compared to solid devices.

Since graphene is a semimetal material, it has some limitations in electronic applications, so I proposed to apply a heteroatom doping of the LIG with the indium selenide 2D material prepared via LPE preparation methods of nanomaterials. This heteroatom doping process is a standard and successful process that changes and tunes the band gap of the LIG modifies its electronic structure, and has a very important impact on the LIG by increasing its SSA. An essential part of the LDW technique is the LrGO process that I worked on in the frame of the REGRAP-2D (PID2020-114234RBC22) project, which was funded by MCIN/AEI/10.13039/501100011033., which is a project between the Instituto de Sistemas Optoelectrónicos y Microtecnología (ISOM) at the Universidad Politécnica de Madrid (UPM) and the Centro de Investigaciones Energéticas, Medioambientales, and Tecnológicas (CIEMAT), which is based in the development of materials based on 2D and three-dimensional (3D) graphene and

other 2D compounds for applications in energy generation and storage (supercapacitors), in this thesis we worked on reducing graphene oxide using the laser technique and comparing our results with the thermal reduction technique made at the CIEMAT center.

The timeline of this thesis started in 2021, during the COVID-19 pandemic period. When the laboratory was not available all the time because of the safety rules in our laboratory that the capacity of users per room should be less than 3 people, therefore the training was not daily even though I started working on the project by reducing the GO using the UV laser, and at the same time training on how to fabricate MSCs, preparing their contacts and the electrolyte, electrodes, and characterization; during my second year, we start our work on rigid MSCs, at the same time I was working on the preparation of LrGO using another laser type, the IR laser, and trying to prepare flexible MSCs, using polyethylene terephthalate (PET) and acetate as substrates for Kapton 60 μm. In my third and final year, because my scholarship founded by the Algerian Ministry of Higher Education and Scientific Research was only for 3 years, I started fabricating flexible MSCs using Kapton 125 μm as a precursor, and at the same time trying to achieve the InSe-LIG doping process. I also trained two master students who were working on LIG MSCs and LIG strain sensors and their transfer to flexible and stretchable substrates such as polydimethylsiloxane (PDMS) and Fixomull.

This thesis is divided into 5 chapters. Chapter 1 is an introduction explaining our motivations, objectives, and the timeline of this work. Chapter 2 presents the theoretical concept of graphene and supercapacitors, explaining the graphene discovery journey, its properties, synthesis methods, and a detailed explanation of our chosen method LDW for supercapacitor applications. It also presents some general concepts about these devices, and comparison between them and batteries, explaining their types, structures, along with a brief overview of the crucial electrolytes used in MSC devices. Chapter 3 explains the methodology and materials that we have used during our work in preparing and characterizing LIG, LrGO, and InSe materials and MSC devices. Chapter 4 is the results chapter of this work. It starts by reporting first the results depending on the rigid, flexible,

InSe-LIG flexible MSC, then the results related to LrGO. Chapter 5 serves as the concluding chapter of this thesis, providing a comprehensive summary of the research work presented throughout the previous chapters. The key findings made in the field of MSCs based on LIG electrodes are highlighted.

2. State of the art

2.1. Graphene and 2D Materials

Two-dimensional materials are a category of materials that are built in only a two-dimensional plane - length and width - with a thickness that measures just a few atomic layers or nanometers (10^{-9}meters). The discovery of graphene by Andre Geim and Konstantin Novoselov, together with their collaborators [11] in 2004, demonstrating its exceptional mechanical, electrical, thermal, and optical properties, has generated interest in the investigation of other 2D materials, which also display fascinating characteristics. These materials find applications in a wide range of fields, including electronics, optoelectronics, and energy storage. Geim and Novoselov were honored with the Nobel Prize in Physics for their groundbreaking graphene work in 2010.

This chapter will begin with a brief background on the steps of graphene discovery. Then, we will pass through the crystalline and electronic structures, which play a crucial role in the supernatural features for which graphene is known. We will go over its list of attributes that match with some other materials that graphene outperformed with its advantages. Some other 2D materials will highlight that graphene meant a revolution: it has boosted the research of the single-layer materials family as promising new-generation nanomaterials that have the capacity to overpower the barriers faced by the traditionally employed semiconductors in the nano-industry.

Ultimately, graphene and 2D materials synthesis methods will be described. Several methods branch out from the two principal procedures, bottom-up and top-down. A brief explanation of the most used methods will be provided. Thereafter, liquid phase exfoliation and direct laser writing techniques will be explained in depth, due to the fact that this thesis is based on these two synthesis methods, top-down and bottom-up, respectively. These two approaches were chosen because we took into account the following requirements: eco-friendly, cost-effective and time-

effective, sustainable, the quality and quantity of the produced graphene and the 2D dopant material, and their suitability for our target application in the MSCs field.

2.1.1. Graphene background

Graphene is a single layer of carbon atoms arranged in a 2D honeycomb lattice. It is a primary structural element of other carbon allotropes such as graphite (3D), carbon nanotubes (1D), and fullerenes (0D).Figure 2.1[12].

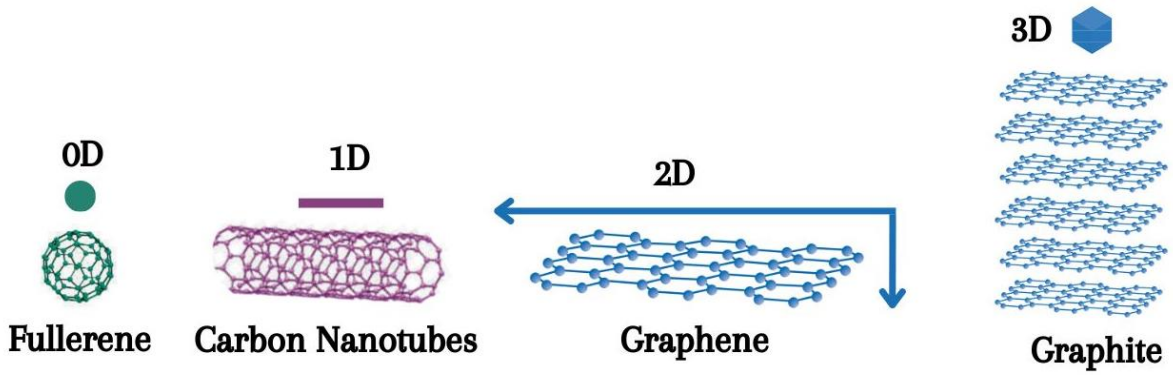

Figure 2.1: Graphene different allotropes: 0D fullerenes when wrapped, transforms into 1D nanotubes through rolling, or arranges into 3D graphite structures when stacked. Updated from ref [2].

As a theoretical concept, graphene was a subject of scrutiny for the first time by the German researcher Schefhaeutl, who reported the intercalation and exfoliation of graphite using acids [13]. In 1859, a British chemist, Benjamin Brodie, made observations of the resulting material from the exfoliation of graphite in strong acids, and he called it "carbonic acid" or "graphon", which was later revealed that he was studying graphene layers surrounded by oxygen-containing groups currently known as graphene oxide [14]. In 1947, Phill Wallace investigated the electronic properties of bulk graphite, he made the pioneering calculations of the band structure of monolayer graphite. One year later, Ruess and Vogt dried a GO droplet, and using a transmission electron microscope (TEM), they observed flakes of a few nanometers thickness. These studies were resumed by Ulrich Hofman and

Hanns-Peter Boehm et al. in 1962, achieving the determination of the thinnest fragment of GO monolayer at that time. The 1970s were the years of epitaxial growth of graphene in Ru and Rh by John Grant and in Ni by Blakely et al. Another growth for the first time in SiC was demonstrated by van Bommel et al. In 1975, Chuhei Oshima developed other suitable carbides such as TiC to grow graphene [15]. In these early results, ultrathin graphitic films and sometimes even monolayers were obtained. However, the supportive metal surface influenced the properties of graphene. Above all, the electronic properties through the interactions between the electrons of the base substrate and the grown graphene

[16]. Boehm and his colleagues introduced the term "graphene" in 1986, deriving it from the combination of the words "graphite" and "-ene," the suffix that refers to polycyclic aromatic hydrocarbons. Their study proposed the hypothesis that graphene is a single-layer material, a proposition that was later confirmed. From 1the 990s to 2000, the creation of graphene has shifted from growth to more exfoliation methods. Yoshiko Ohashi achieved the separation of the graphite layers at approximately 20 nm in thickness, 60 times the real thickness of graphene. During this process, they investigated the electrical characteristics and observed a remarkable electric field effect leading to unstable resistivity. Before 2004, significant advances in graphene research were made through reduction of layer thickness, in conjunction with extensive characterizations using techniques such as scanning electron microscopy (SEM), atomic force microscopy (AFM), and scanning tunnelling microscopy (STM) [15]. In 2004, graphene was first isolated and characterized as a single layer of stable carbon atoms under ambient conditions[17]. In parallel, Berger et al. also succeeded in epitaxial growth on crystalline SiC and the characterization of a monolayer graphene sheet [18]

Innovative achievements were realized by A. Geim and K. Novoselov at the University of Manchester (Home of graphene). They employed a mechanical exfoliation method using scotch tape, repeatedly peeling, folding, and separating layers of graphite until they obtained a single layer of graphene. In honor of their seminal contribution to the study of graphene, which scientists had pursued since the 19th century, Geim and Novoselov were awarded the Nobel Prize in Physics in

2010. Their work not only marked a significant advancement in graphene research but also aroused interest in exploring other 2D materials with similar enticing.

Figure 2.2 summarize the timeline of graphene discovery.

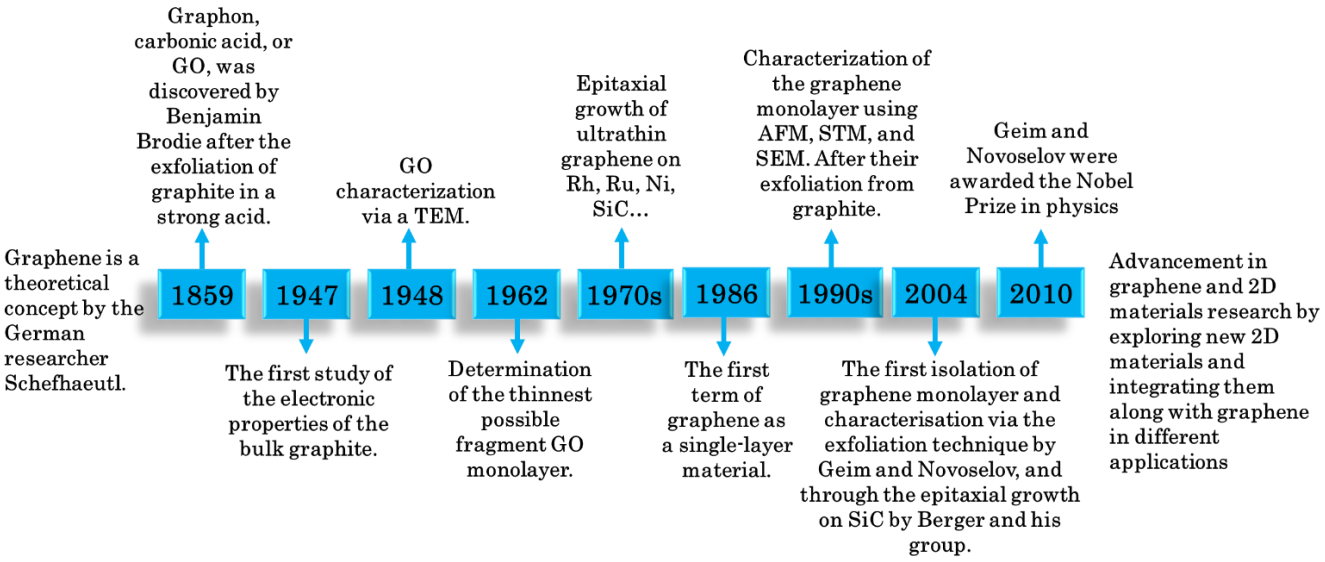

Figure 2.2: Graphene discovery timeline.

2.1.2. Crystalline and Electronic Structures

Graphene is structurally composed of a regular hexagonal lattice of carbon atoms. The carbon atoms are separated by an interatomic uniform carbon-to-carbon atoms distance of a_{c-c}= 0,142 nm, and form angles of 120° between them. Although the lattice exhibits some symmetry, it is not a Bravais lattice, since graphite is an accumulation of graphene layers relocated in succession [19]. Instead, it is an overlapping of two triangular Bravais sublattices, formed by carbon atoms of types A and B. In this configuration, the atoms of one sublattice are positioned at the centers of the triangles formed by the atoms of the other sublattice as shown in Figure 2.3. a.

The primitive triangular lattice is defined by its vectors [19]:

$$\vec{a}_1 = \frac{a_{c-c}}{2}(3;\sqrt{3}) \text{ and } \vec{a}_2 = \frac{a_{c-c}}{2}(3;-\sqrt{3}).$$

Considering that $\vec{a}$ is the vector that connects two nearest carbon atoms of the same type, therefore:

$$\|\overrightarrow{a_1}\| = \|\overrightarrow{a_2}\| = \sqrt{3}\, a_{c-c} = 0{,}246 \text{ nm}.$$

Selecting an atom type, A for example. It has three nearest neighbors, all of which are essential type B, and they are joined by the following vectors [19]:

$$\vec{\delta}_1 = \frac{a_{c-c}}{2}(1;\sqrt{3}),\ \vec{\delta}_2 = \frac{a_{c-c}}{2}(1;-\sqrt{3}),\ \vec{\delta}_3 = -a_{c-c}(1;0).$$

Indicating that $\left\|\overrightarrow{\vec{\delta}_1}\right\| = \left\|\overrightarrow{\vec{\delta}_2}\right\| = \left\|\overrightarrow{\vec{\delta}_3}\right\| = a_{c-c}$, being the interatomic spacing between two adjacent carbon atoms as was explained previously (displayed in Figure 2.3. b).

The reciprocal lattice, or the indirect space, is the space of the K wave vectors in the Brillouin zone. It is also a primitive hexagonal lattice and has the property of being able to represent all the properties of the real direct lattice. Its base vectors $\overrightarrow{b_1}$ and $\overrightarrow{b_2}$ can be calculated from the following relation [19]:

$$\overrightarrow{b_1} = \left(\frac{2\pi}{a_{c-c}};\frac{2\pi}{\sqrt{3}a_{c-c}}\right),\ \overrightarrow{b_2} = \left(\frac{2\pi}{a_{c-c}};-\frac{2\pi}{\sqrt{3}a_{c-c}}\right)$$

Inside this zone, we identify points of high critical points for graphene. The K, K', M, and Γ points are particularly useful.

The Γ point is the point where the momentum is zero located in the center of the Brillouin zone, M is in the middle of one side of the hexagon. The curve in (Figure 2.3. c, left) shows that the valence band and the conduction band of graphene touch each other at highly symmetrical six K points, which are the corners of the hexagon at the first Brillouin zone, presenting Dirac points [20]. Zooming at one edge of the hexagon, (as presented in Figure 2.3. c, right), K and K are two energetically inequivalent symmetric points. In Dirac cones, the band energy with momentum has a linear relationship, making the graphene charge carriers an effective massless Dirac fermion that are able to transit with a high speed between the two bands. Thus, as well, the valence band and conduction band overlap slightly at Fermi level. Due to these characteristics, graphene is considered a zero-band-gap semiconductor or semi metallic material [21]. At the ground state, the carbon atom has 6 electrons with an electronic configuration $1s^2 2s^2 2p_x^1 2p_y^1 2p_z^0$, 4 of them are

valence electrons $2s^2 2p_x^1 2p_y^1$ which are the responsible of the three-hybridization types of carbon atom [22]. One of them is the sp^2 hybridization, the primary building block of graphene in which each carbon atom has three sp^2 hybrid orbitals arranged in a trigonal planar configuration (2D) and the one that remains is the $2p_z$ orbital, which is perpendicular to the plane of the sp^2 hybrid orbitals. The three sp^2 hybrid orbitals form three strong-short sigma (σ) bonds and an angle 120° with three neighboring carbon atoms within the same layer, equivalent to the crystalline lattice we have discussed earlier. The $2p_z$ unhybridized orbital does not participate in bonding, but it is responsible for the Pi (π) bonds [23] that form the weak Van der Waals liaisons between adjacent carbon atoms. See Figure 2.3. d.

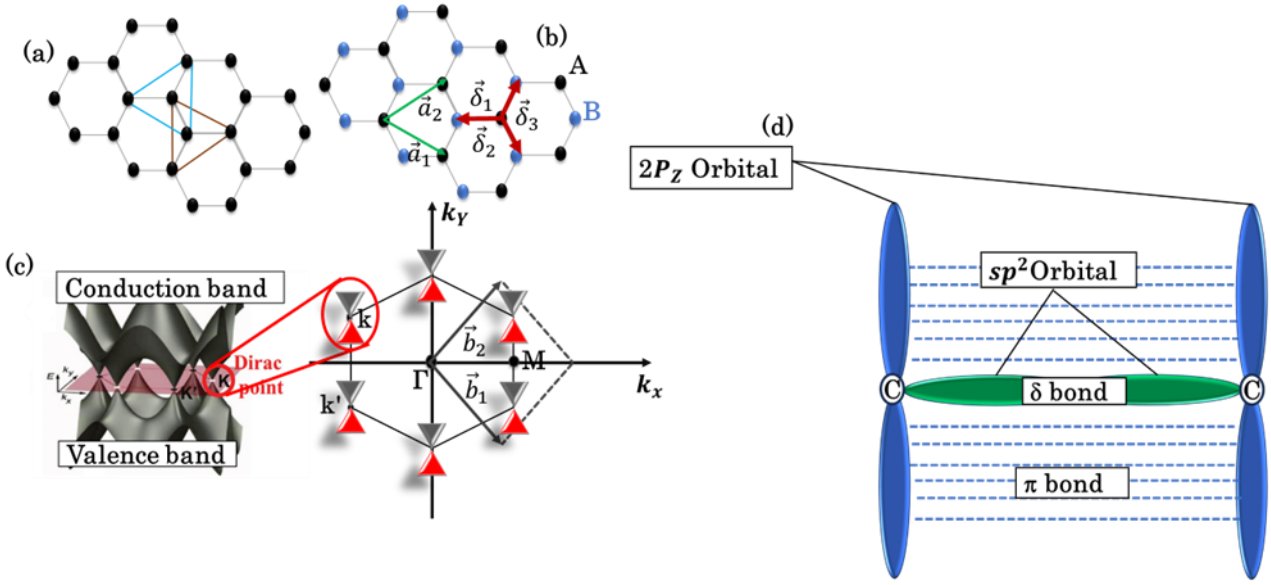

Figure 2.3: The crystalline structure of graphene. (a) the overlap of Bravais sublattices, (b) the primitive vector's atomic structure $\vec{a}_1$and $\vec{a}_2$ are the basic vectors of the Bravais lattice, δ vectors are the first-nearest-neighbor vectors of an atom type A or an atom of type B, (c) graphene band structure in 3D updated from ref [12], their reciprocal space with basic vectors $\overrightarrow{b_1}$ and $\overrightarrow{b_2}$, and an illustration of Dirac cones, (d) the atomic structure and presentation of the sp^2 hybridization, δ and π bonds.

2.1.3. The outstanding properties

The rearrangements among the carbon atoms play a pivotal role in creating the distinctive crystalline structure and conferring exceptional properties on graphene, as shown in Figure 2.4:

- The World's thinnest material, measuring only 0,334 nm [24].
- It is also the strongest material, boasting a tensile strength of 130 GPa [25], with an elastic or Young modulus of 1 TPa [24], which is about 100 times greater than that of steel. This makes graphene a very stretchable material.
- Graphene exhibits a remarkable thermal conductivity of more than 3.000 W m/K [25], which enables it to transfer heat efficiently.
- With an outstanding electron mobility of 250.000 cm^2/Vs, graphene has the potential to maintain huge electric current densities at levels a million times greater than copper [25].
- Graphene has a theoretical large specific surface area up to 2630 m^2/g [20], making it a very good adsorbent working area for many applications and stands as an entirely transparent material, with a transmittance of 97,4% [24].

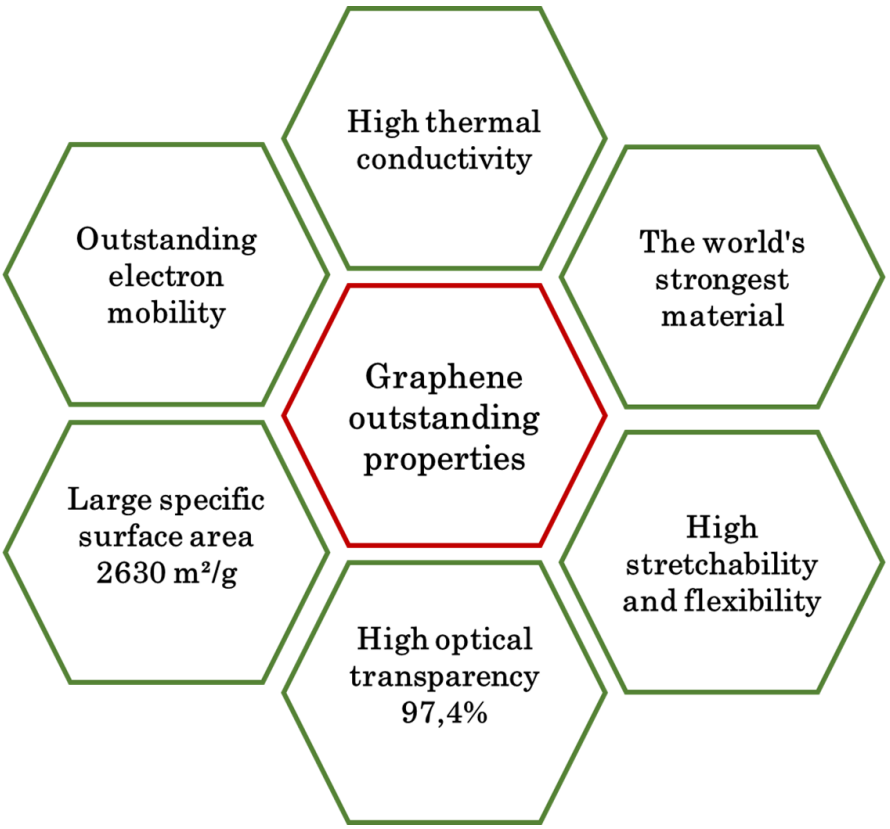

Figure 2.4: Outstanding properties of graphene.

2.1.4. Other 2D materials

Semiconductors, especially silicon, are currently considered the leading materials in the electronics industry, but according to Moore's law for device scaling, which states that every two years the number of transistors on a chip will increase [26], there is a fear that their properties will reach their limits when attempting to further miniaturize in the near future. Concurrently, the discovery and the characterization of the outstanding graphene properties have aroused a great deal of curiosity to explore more 2D materials analogous to it. Inspired by the graphene exfoliation technique, several interlayered Van der Waals materials have been studied up to their monolayer features and demonstrate the potential to overcome the limitations that traditional semiconductor materials present to modernize the electronics industry by enabling the creation of smaller, faster, and more energy-efficient miniaturized device generation. Hexagonal boron nitride (hBN) has an identical hexagonal lattice structure to graphene, with two different atoms of boron and nitrogen alternatively forming a honeycomb arrangement that produces an irregular sublattice with a large band gap of 5-6 eV [27]. Therefore, it is an electric insulator, key in different applications such as electronics, optics, fuel cells, and biomedicines. The properties of hBN properties can be adjusted by doping or hybridization [27]. 2D transition metal dichalcogenides (TMDs) are another interesting group that have a standard formula MX_2, where M refers to a transition metal: Mo, W, V, Nb, etc., and X represents the chalcogen: S, Se, and Te. It is worth drawing attention to molybdenum disulfide (MoS_2). Monolayer MoS_2 is exploited in photovoltaic devices and photocatalysis due to the narrow band gap (i.e. 1,9 eV). Tungsten diselenide (WSe_2) has also gained a great interest among the other materials in this group.

This 2D materials group is formed by chemical compounds that have several structures and consequently different properties, with an increase in the band gap energy from a minimum of 0,9 eV in the bulk form to a maximum of 2 eV in the monolayer structure, which presents a remarkable shift from an indirect to a direct band gap [26]. Beyond, there are abundant other 2D materials such as black

phosphorous[28], MXenes [29], as well as up to 15 new bidimensional materials from the main elemental group predicted theoretically such as 2D indium (indiene) and 2D aluminium (aluminene), and experimentally obtained as 2D silicon (silicine), 2D germanium (germanene), and 2D boron (borophene) [30]. All of them demonstrate their fascinating properties and motivate the investigation of more comparable elements for the purpose of integrating them in a broad area of nano-fields: electronics, optoelectronics, energy storage and beyond.

2.1.5. Graphene Synthesis Methods

The efficiency of graphene, together with the other revolutionary monolayer materials, has triggered the attempt to integrate them into the industry. There is an increasing demand for mass production considering high quantities, high quality, low cost, and time consumption. These requirements gave rise to the creation of several synthesis methods that differ from each other in terms of process complexity, materials consumption expenses, and properties of the resulting material. These methods can be classified into two basic approaches: top-down and bottom-up, as shown in Figure 2.5. The top-down technique was the first successful process in the isolation of the first monolayer graphite. Accordingly, the fundamental concept of this method is to break down the Van der Waals forces in the bulk material to decrease the thickness and obtain the thinnest possible layer. Unlike the previous technique, the bottom-up process centers on growing a thin layer sheet that starts from the basic atom element that forms the resulting material. GO, carbon atoms and organic materials are examples of certain precursors to produce graphene through a bottom-up technique.

In the next section, we will discuss several popular methodologies for synthesizing graphene concretely. Most of these techniques are also applied to the other 2D materials.

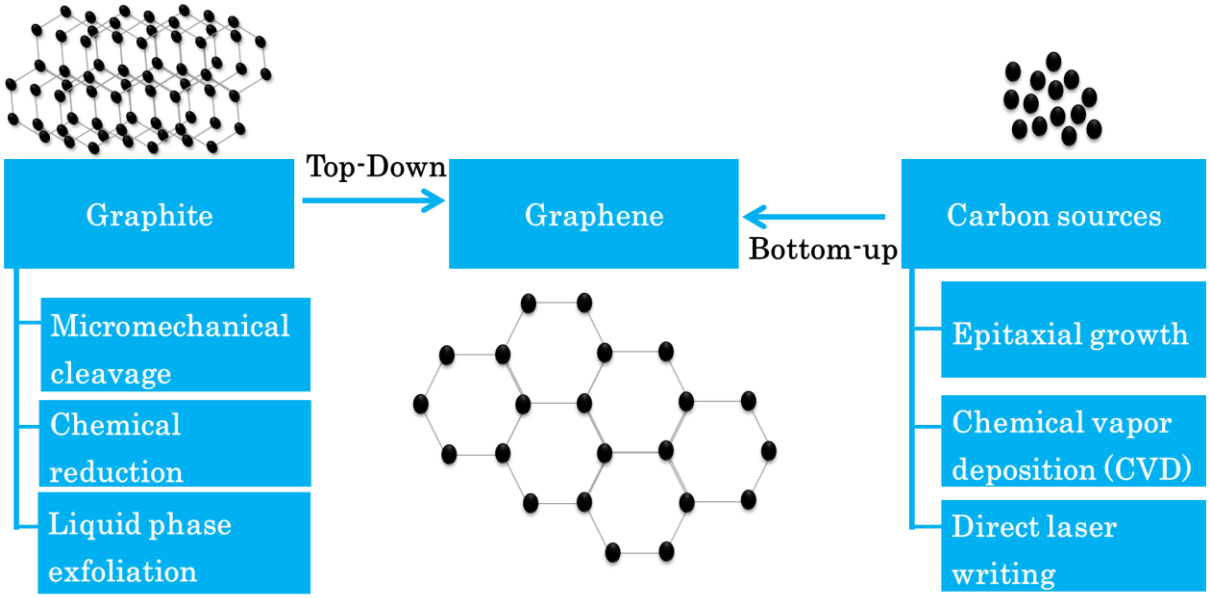

Figure 2.5: The basic methods of graphene synthesis and examples of the most popular techniques from the bottom-up and top-down methods.

2.1.5.1. Top-Down

There are several methods, but they basically share the principal trait of commencing with a bulky graphite material and then cleaving it down into a few layers of graphene by breaking the van der Waals forces. Micromechanical cleavage, chemical oxidation and reduction, and liquid phase exfoliation are the foremost utilized approaches of the top-down method.

2.1.5.1.a. Micromechanical Cleavage

Also known as micromechanical exfoliation, scotch tape or peel-off technique consists of the successive separation of the bulk material, in this case, graphite layers. An adhesive tape is used to break down the Van der Waals force between the interlayers of the bulky crystals without breaking the in-plane covalent bonds.

This simple method allowed the Nobel prize-winning winner to cleave the graphite from a pencil to obtain a monolayer graphene pressing the scotch tape onto the

graphite surface and then carefully pulling it off. The continuous peeling of graphene generates a decrease in the number of graphite layers, and the produced graphene sheet exhibits a high quality, but the modest quantity obtained, and the time-consuming process avoid the use of this technique in the commercial application. It is fundamentally recommended for academic research [31]. Figure 2.6 represents a simulation of the trials using the scotch tape technique using graphite.

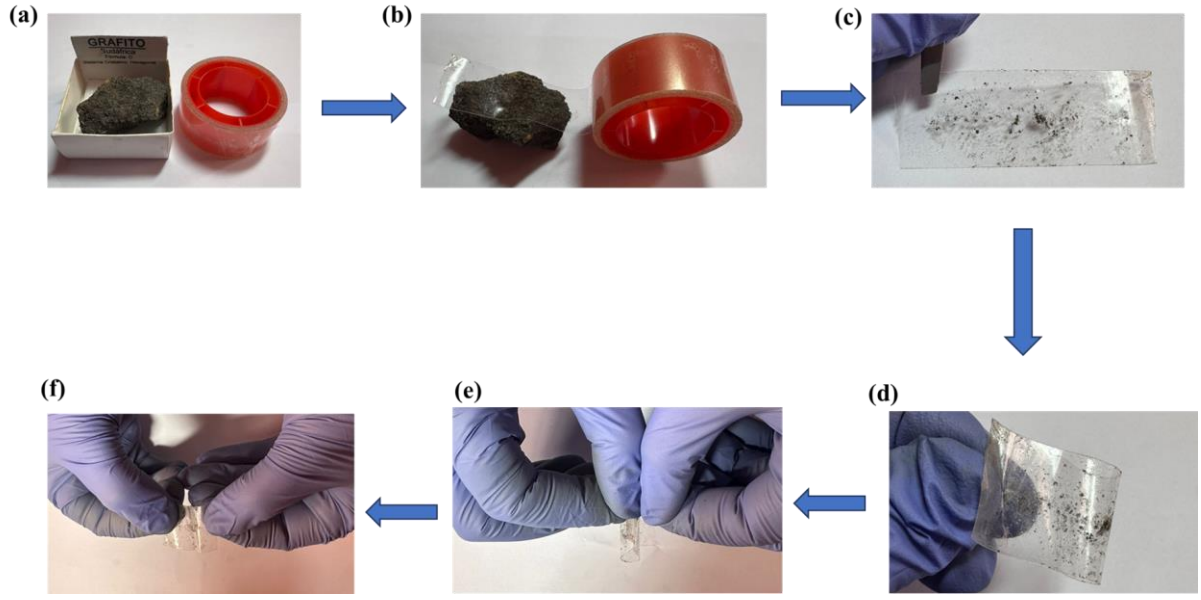

Figure 2.6: Top-down synthesis method. Graphite exfoliation with scotch tape (an attempt to simulate the first successful strategy to isolate single-layer graphene). Letters (a) to (f) indicate the sequence order of the process.

2.1.5.1.b. Chemical reduction

In preparation for the reduction step, graphene oxide is first needed in this method. There are a significant number of reports that investigate the synthesis of GO. M.B. Gómez-Mancebo et al. [32] reported a detailed methodology of Hummer´s Method, presented in Figure 2.7, which is one of the most traditional approaches to prepare graphite GO, using a strong acid in combination with other components of chemical oxidizers (H_2SO_4, HCl, $NaNO_3$), followed by mixing this compound under meticulous temperature regulation, then introducing reducing and reaction

stopping agents such as H_2O_2 in the final stages of the procedure [32]. A great number of studies improved the following reduction steps considering the key parameters: GO amount, time, and temperature. An essential aspect is to keep the process environmentally friendly by using safe chemical reducing agents to remove the maximum extent of oxygen-containing functional groups that decorate the few layers of graphene [33]. Alternative reagents such as ascorbic acid known as vitamin C, plant-based extracts such as Tulsi leaf, and more prove that they can be used as a substitute of the most frequently utilized reducing agent hydrazine, which is non-environmentally friendly. By this way, GO can also be successfully bio reduced [34]. This method seems to provide higher productivity compared to micromechanical exfoliation. However, because it involves two distinct steps, it is relatively complex. Firstly, the Hummer method requires various steps to synthesize graphene oxide from graphite, and graphene oxide can be prepared in various structural forms [33]. Subsequently, to reduce the oxygen content, it is necessary to select an appropriate and safe reducing agent while also adjusting the other reduction parameters, as we have previously discussed. However, this technique is a promising candidate for numerous applications, including FETs, solar cells, energy-related applications, and the fabrication of flexible composite materials.

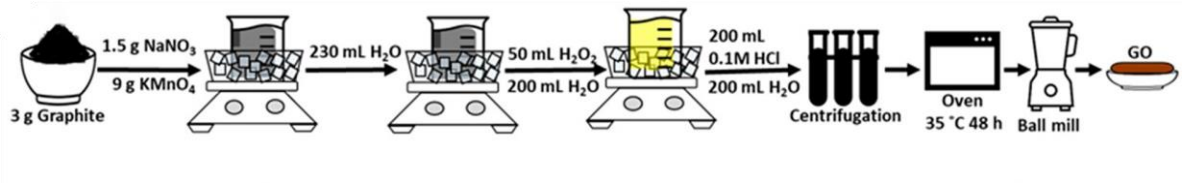

Figure 2.7: GO preparation steps using Hummer´s method [32].

2.1.5.c. Liquid phase exfoliation

Liquid phase exfoliation is an advanced and economical top-down method which consists of natural flaking of a 3D material using high-shear mixing, jet cavitation, or sonication, the most popular technique. Each of them is performed in a liquid medium that includes organic solvents, ionic liquids, a solution of water / polymer or surfactant, green dispersants, or by mixing more than one solvent (mixed solvent strategy) [35]. Coleman and his group had a pioneering achievement in the preparation of graphene by LPE, by the sonication of the graphite powder in the organic solvent N-methylpyrrolidone (NMP) followed by a centrifugation to differentiate between the mass at the macroscopic and microscopic scale [36]. A successful exfoliation was achieved, wherein the graphite powder changed into a homogeneous, stable dark dispersion for a long time.

The key parameter in this procedure is to select the correct LPE media considering several characteristics: personal health, being environmentally friendly, affordable, and having a low boiling point [37], which is also crucial for safety by reducing the risk of explosions or fires that can occur with solvents of high boiling point. The ideal media makes exfoliation quicker, more efficient, and simplifies the specific production of high-quality nanomaterial. NMP is an effective solvent in the LPE process, not only with graphite but also with many other materials. As an illustration, Zhang et al. [38] conducted 48 LPE experiments with numerous solvents such as isopropyl alcohol (IPA) and acetone in addition to NMP. Different sonication times and powers were applied on indium selenide, demonstrating that NMP was the optimum solvent, which produced a good concentration dispersion and uniform InSe sheets. However, NMP is incompatible with the safety rules we have discussed before. For this reason, scientists innovated several LPE strategies by combining solvents or by increasing sonication time. Coleman [39] a new safe exfoliation using low boiling point organic solutions such as acetone, isopropanol, and chloroform, but resulted in less concentration in the graphene dispersion; this drawback can be compensated by adjusting the power and sonication time. The same group studied the influence of these factors, whereas increasing sonication time leads to a decrease in graphene flakes lateral dimensions. Another option to fill this gap is to use an agent solvent or surfactants. Lotya et al., for example,

obtained a graphene concentration of up to 0,05 mg/ml using water and the surfactant sodium dodecylbenzene sulfonate (SDBS) with only 30 min of sonication [35]. However, the use of surfactants is generally an unwelcome suggestion [37] because it generates a defective product that has a structure containing a combination of the surfactants and the exfoliated material. It is extremely difficult to separate them, affecting the properties and effectiveness of the 2D material. Also, the quality of the bulk material itself is another factor to be considered. Sonication and centrifugation times needed to exfoliate large flake materials are different to the time needed for exfoliating powder and the size of the prepared nanomaterial to fit in our application is another aspect we must consider. All these factors will be fixed through ongoing experimentation.

Top-down graphene production faces several challenges, such as the separation of the graphene layers, while conserving the planar interatomic. The graphene layers in graphite are very weakly bonded together, so it is difficult to separate them without damaging them. Once the graphene layers have been exfoliated, they tend to re-agglomerate or stick back together. This can make it difficult to process graphene and to use it in applications. Top-down approaches for graphene production typically involve several steps, which can make the process complex and expensive. Graphene production typically has low yields, meaning that only a small fraction of the starting graphite is converted into graphene. Among the described top-down methods, LPE seems more relevant in terms of price, effectiveness, and ease of operation, but we must pay attention to pick nontoxic solvents to follow the safety standards (check Figure 2.8).

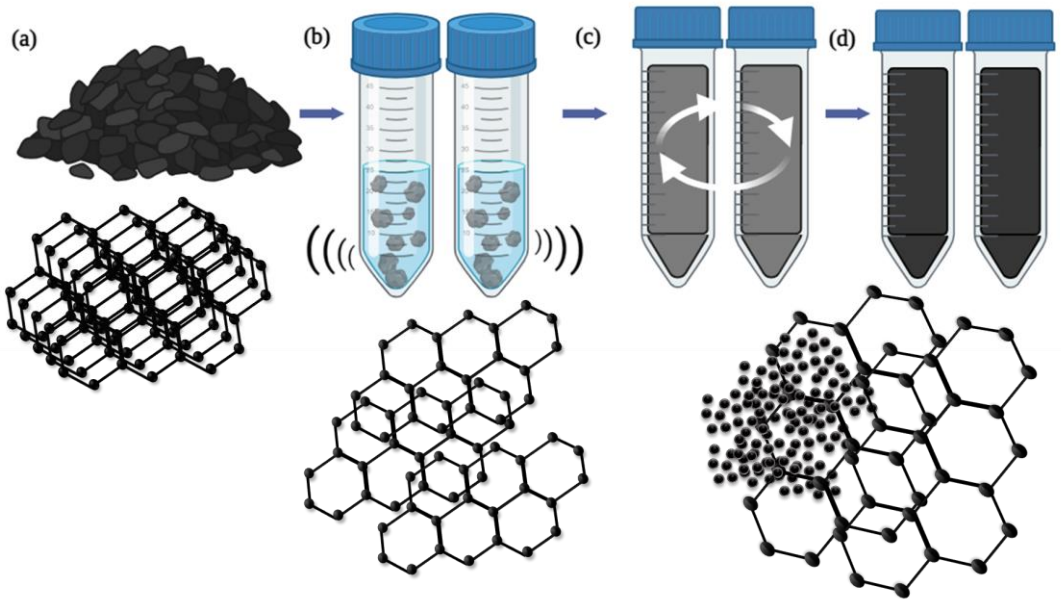

Figure 2.8: The basic concepts of the liquid phase exfoliation technique, starting from (a) the 2D bulk material graphene (for example). (b) Sonicating it in the appropriate solvent, followed by (c) the centrifugation step, and (d) the resulting black solution after the LPE, which characterizes the color of graphene.

2.1.5.2. Bottom-up

With respect to the synthesis of graphene, the bottom-up method has a broad range of applications. In contrast to the top-down method, which is based principally on the thinning of graphite, in the case of the bottom-up methods, several starting materials can be used as carbon sources to arrange carbon atoms to form graphene single layer structures. Epitaxial growth, chemical vapor deposition (CVD), and direct laser writing are the most common bottom-up techniques.

2.1.5.2.a. Epitaxial growth

Epitaxial growth is a deposition technique that produces a monocrystalline film on a monocrystalline substrate using gas or liquid precursors. This method has been used since the 1970s for growing graphene, as we have seen previously in Section 2.1.1, using metallic substrates like Ru (0001), Rh (111), Re (0001), Ir (111) Au (111), Cu (111), and Cu (100). However, SiC is the most frequently used substrate. By heating to high temperatures, the silicon on the SiC surface sublimates, leaving

behind carbon atoms that form a carbonic surface [40]. By precisely controlling the growth conditions, these atoms can align themselves to create a graphene film. The Berger group synthesized ultrathin epitaxial graphite films, only a few monolayers thick, on the Si-terminated (0001) face of single-crystal 6H-SiC by thermal desorption of Si. Samples were etched with H_2 and heated by electron bombardment in an ultra-high vacuum to remove the oxide. Multilayered prepared films, composed of typically three graphene sheets, were grown with a size of 10^{-9} nm; this layer thickness can be determined by controlling the temperature [41]. Figure 2.9 presents a scheme that presents the basics of the epitaxial growth method.

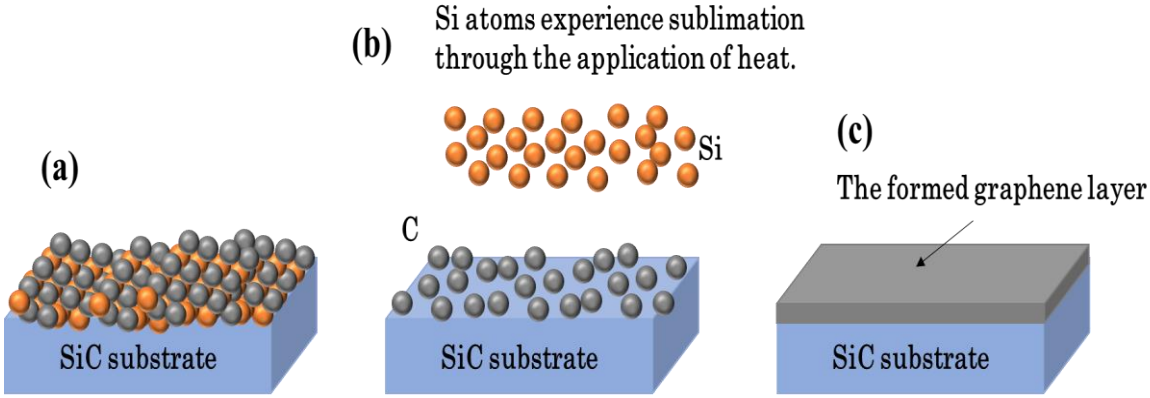

Figure 2.9: Scheme presenting the epitaxial growth technique.

2.1.5.2.b. Chemical vapor deposition

CVD synthesis has become a reliable and scalable method for producing large-area graphene. This method has been successful in synthesizing high-quality graphene in vast areas. The process involves the activation of gaseous reactants and the subsequent chemical reaction. Hydrocarbon gases such as methane, ethane, ethylene, acetylene, liquids such as methanol, benzene, toluene, acetone, and solids (polystyrene, polymethyl methacrylate (PMMA), poly (ethylene glycol) (PEG), polyvinylpyrrolidone (PVP), carbohydrates, etc.…) are examples of precursors used as a source of carbon in CVD synthesis [42]. This leads to the formation of a stable solid deposited on a suitable substrate usually composed of various transition

metals like Ni, Pd, Ru, Ir, and Cu, where copper and nickel are the most used substrates [43]. The energy required for the chemical reaction can be supplied through various sources, such as heat, light, electric discharge, laser-assisted, or plasma-assisted [44]. Therefore, this process has several subtypes such as low-pressure CVD (LPCVD), atmospheric pressure CVD (APCVD), thermal CVD (TCVD), and plasma-enhanced CVD (PECVD) [42]. R. Muñoz and C. Gómez-Aleixandre have provided a detailed summary of the steps involved in CVD. These steps include heating, annealing, growing, and cooling [44]. Finally, to use graphene in various applications, it is necessary to separate the catalytic metal substrates from the graphene and transfer the latter onto different substrates using PMMA separation steps [45].

2.1.5.2.c. Direct laser writing

Direct laser fabrication of graphene is a new graphene production technique that includes two strategies: laser-reduced graphene oxide starting from graphene oxide as a precursor and laser-induced graphene coming out from commercial plastics and organic sources. This modern technology is a powerful tool that has proven its effectiveness compared to other manufacturing methods as (a) it is a facile and flexible one-step process, (b) it does not require additional chemicals or masks or a clean room environment, (c) it is sustainable, ecological, and economical, (d) it is fast and has the potential to produce large-scale solid-state graphene [46]. The produced graphene structure and morphology depend on several parameters. The laser sources that have been used to create graphene are classified into two types: continuous-wave lasers (CW) and pulsed lasers. The CW lasers generate continuous energy and low output power such as diode lasers and semiconductor lasers. The pulsed laser offers a discontinuous wave with high output power and the laser is named femtosecond, picosecond, nanosecond, and microsecond as a function of its pulse duration [46]. The working mechanism of this technique depends on the laser wavelength and the photon energy that will be absorbed by the precursor: the photoreduction can be photothermal, photochemical, or a combination of both processes. In general, a laser wavelength

> 400 nm produces a photothermal effect and a laser wavelength < 400 nm, a photochemical effect. In some cases, both processes occur. Smirnov et al. reported that the GO photoreduction threshold was 3,2 eV for a laser with short wavelength [46]. GO will be reduced via a photochemical effect generated by the laser, when the C−O chemical bonds break and the oxygen-containing groups (OCGs, e.g., epoxy, hydroxyl, and carboxyl) are removed, especially when the dissociation energy is shorter than the absorbed photon energy [47]. In another work, a photothermal reduction of GO was reported within a temperature ranging between 200 to 230 °C [48]. The high temperature yielded by the laser can easily break C−O and C=O bonds, resulting in the reduction of GO. Lin et al. [49] used a CO_2 laser with a wavelength and long pulse of 10,6 μm and 14 μs, respectively. To generate graphene from a polymer photothermally, the energy produced from the laser high temperature, up to 2.500 °C, can smoothly break down the C—O, C=O, and N—C bonds. Basically, the photoreduction occurs via two sub-processes: carbonization by removing the other atoms (O, N, H), which are emitted as gases, and keeping only carbon atoms and rearranging them to build the graphene structure[46].

Strong et al. [50] reported for the first time a successful laser reduction of a GO film using a diode laser LightScribe DVD optical drive [47] with a wavelength of 788 nm and an output power of 5 mW. The characterization of the reduced film demonstrated the film transformation to graphene, with the film color changed from grey to black and becoming darker under high laser intensities. The SEM images before and after reduction showed that the film morphology exhibits a significant modification in the GO structure, with an expanding sheet thickness and 3D porous graphene. The reduced GO film also presented high electrical conductivity.

Another photoreduction was achieved by Tour´s group from a commercial polymer, polyimide [49]. Using a IR carbon dioxide (CO_2) commercial laser, a graphene-like material was produced. Raman characterization of the polyimide before and after applying the laser demonstrated the existence of prominent graphene peaks. The intensity of the G peak was higher than that of the D peak, meaning that there was more graphitization and less defects. The 2D peak, related to the graphene material, was well centred at 2.700 cm^{-1}.

The characteristics of laser-induced graphene produced by DLW are affected by environmental parameters such as pressure and temperature, including the pores' diameter and material thickness, the conductivity, and the surface hydrophilicity. Tour´s group [51] has prepared LIG in different controlled atmospheres. In an air environment, the laser writing process led to graphitization accompanied by oxidation, forming thicker graphene films with a rough surface texture. The pores in the LIG were found to be micrometer-sized and widely dispersed and to contain a significant amount of oxygen. Conversely, oxidation was suppressed, and carbonization dominated when the laser writing process occurred under an inert atmosphere, such as that of argon (Ar). This static environment favored the creation of thinner LIG films with smoother surfaces, a narrower distribution of pore sizes, a higher carbon content, and an increased electrical conductivity. Additionally, altering the surrounding gas atmosphere impacted profoundly the water contact angle on the LIG surface. When oxygen (O_2) or air was used, the contact angle was reduced to 0 ° (super hydrophilic). On the contrary, the use of inert or reducing gases (Ar, H_2, or SF_6) resulted in a contact angle exceeding 160 ° (super hydrophobic); these different wetting properties could be attributed to changes in surface morphology and the chemistry of the LIG structure.

The laser parameters are critical key factors that can make significant modifications to the produced graphene material. Lamberti and his group [52] have investigated the fluence of scan speed and frequency on the morphology of LIG; this variation results in a different structuring, ranging from needle, sheets to pores. X-ray photoelectron spectroscopy (XPS) and Raman spectroscopy demonstrated that the different morphologies had graphene-like structures with a high degree of graphitization in the porous structure and high atomic percentage of carbon, up to 98%. With these differences in the chemical structure, the morphology of the LIG sheets showed the smallest contact angle. This meant that they were more hydrophilic and exhibited good electrochemical performance in their application on MSCs because of the smooth absorption of the electrolyte.

Velasco et al. [53] studied the optimization of laser parameters (power, scan speed, fluence) and their impact on LIG quality and therefore on the performance of MSCs. The scanning electron microscopy images clearly exhibited different

numbers and sizes of pores. By adjusting the laser parameters, a more uniform pore size and distribution was obtained. Raman mapping on the optimized LIG showed less defect, and a high graphitization with a good I_G/I_D peaks intensity ratio, as expected from a high quality LIG. El Kady et al. [54] demonstrated the efficacy of LrGO in fabricating high-performance flexible MSCs with ultrahigh power and energy densities compared to a commercially available activated carbon-based supercapacitor. One year later, Lin et al. [49] reported highly porous laser-induced graphene from Kapton after testing around 15 polyimides; Kapton exhibited high graphene quality. Other organic precursors proved a successful transformation into LIGs using a laser. Chyan et al. [55] prepared LIG from bread, coconut, and potato skin, clothing, wood, and paper. In
Figure 2.10, a summary of the direct laser writing technique to produce graphene is presented.

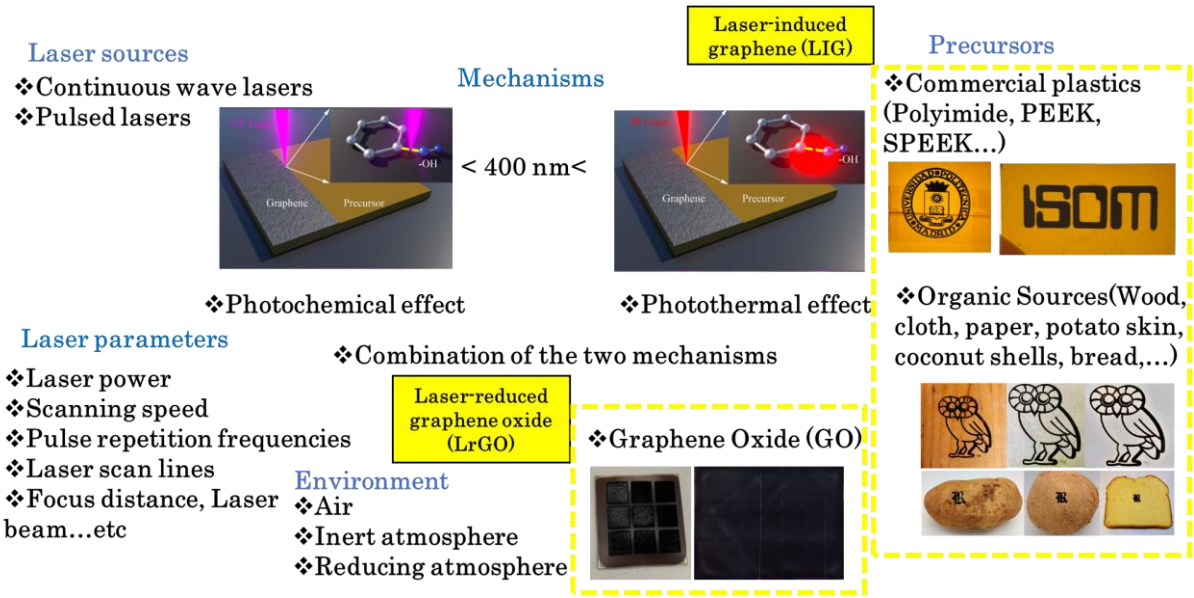

Figure 2.10: Summary of some of the critical parameters in the DLW technique, and illustration of the two main DLW applications LIG and LrGO [55][56].

Regarding the classification of graphene synthesis methods by K. S. Novoselov and his group, we could introduce LDW in the middle of the graph presented Figure

2.11, because this technique has a broad appeal in many aspects: (1) a wide range of choices for precursors, (2) it is easy and safe, (3) it is a mass-production strategy that allows a wide choice of preparations of graphene-like materials in terms of size, quality and quantity with cost-effectiveness, (4) a high tunability of graphene quality by adjusting different parameters which are a fast and uncomplicated method, besides it as we have discussed in detail. DLW is considered a promising and versatile technique for various applications such as flexible and wearable electronics, energy storage, strain and biosensors, optoelectronics, and more.

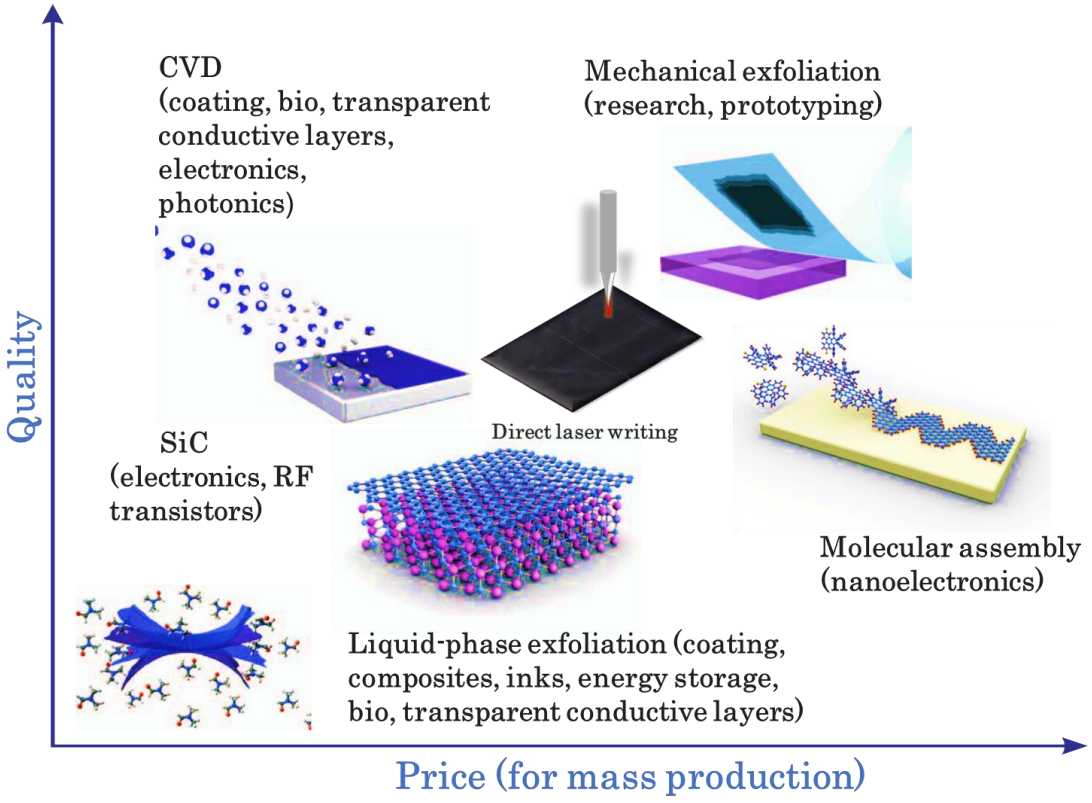

Figure 2.11: Comparison between graphene preparation methods in terms of quality and price updated from ref [25].

2.1.6. Laser-induced graphene heteroatom doping

As we have seen in Section 2.1.2 where we discuss the electronic properties of graphene that this material has a zero-band gap or is a semimetal, which affects

and limits its application, especially in the electronics field. Hence, heteroatom doping has become a successful approach that involves replacing carbon atoms with heteroatoms such as boron, nitrogen, phosphorus, etc. [57] to enhance its electronic properties and improve the energy storage of the devices.

In the application focus of this thesis, the introduction of heteroatoms creates more electrochemically reactive areas, improving the potential of graphene for energy storage [57] and when we talk about LIG, heteroatom doping proves to be a significant improvement of the material by increasing its conductivity, flexibility, stretchability, and specific surface area (SSA). Several works have proved the efficacity of this approach with LIG MSCs field such as H. Liu et al. [58] whose prepared flexible LIG-MSCs doped with Fe_3O_4 nanoparticles that increased the areal capacitance to 719,28 mF/cm^2 over 100 times higher compared to the LIG-MSCs, C. Zhou et al. [58] manufactured flexible LIG-MSCs decorated with MoS_2/MnS and this increased the areal capacitance of the devices from 2 to 15 times compared to MSCs based on pristine LIG, C. Zhang et al. [60] doped the LIG with ZnP nanosheets to produce flexible and stretchable MSCs, this process results in a high capacitance 1425 F/g and also the increase in the increase in the SSA from 320 pristine LIG to 345 m^2/g ZnP-LIG and larger the pore size distribution from 374 to 435 nm; also, the devices exhibit a stable performance up to 100% against reversibly bending and stretching deformations, these results and more presented in Table 2.1 motivated us to apply this approach in our study, we focus more on the studies that they used a CO_2 laser machine and polyimides as precursors because this thesis is based on these similar materials, the outcomes presented in this table gave us huge information about the dopant preparation, doping methods, and laser applications technique which provides us with an overview for our study in the heteroatom LIG doping approach.

Table 2.1:LIG heteroatoms doping from polymers using CO_2 laser for MSCs application.

Laser	Product with dopant(s)	Precursor/substrate	Structure	Electrolyte	Voltage (V)	Capacitance	Power	Energy	Ref
CO_2	LIG+PEDOT	PI	In-plane	1,0 M H_2SO_4	0_1	115,2 F/g at 0,5 A/g	/	/	[61]
CO_2	LIG-N LIG-N(HNO_3)-PEDOT	Silicon Rubber	In-plane	PAAK-KOH	0_0,8	790 µF/Cm^2 at 50 µA/cm^2 720 µF/Cm^2 at 75µA/Cm^2	/	/	[62]
CO_2	NiO/Co_3O_4/LIG NiO/Co_3O_4/LIG-WPU	WPU	In-plane	PVA-H_3PO_4	0_0,8	2,4 mF/Cm^2 at 10 mV/Cm^2	/	/	[63]
CO_2	Co_3O_4/LIG-80J/Cm^2 Co_3O_4/LIG-80J/Cm^2	PI WPU	In-plane In-plane	PVA-H_3PO_4 PVA-H_3PO_4	0_1 0_1	15,3 mF/Cm^2 1,8 mF/Cm^2	/	/	[64]
CO_2	MoS_2/MnS/GR	PI	In-plane	PVA-Na_2SO_4	0_1	58,3 mF/Cm^2 at 50 µA/Cm^2	49,9 µW/Cm^2	7 µWh/Cm^2	[58]
CO_2	LIG+Ni-CAT MOF	PI	In-plane	PVA-LiCL	0_1,5	15,2 mF/Cm^2 at 0,2 mA/Cm^2	7 mW/Cm^2	4,1 µWh/Cm^2	[65]
CO_2	LIG+PANI LIG+MnO_2 LIG+FeOOH LIG+FeOOH//LIG+MnO_2	PI	In-plane In-plane In-plane In-plane asymmetric	PVA-H_2SO_4 PVA-LiCL PVA-LiCL PVA-LiCL	0_0,8 0_1 / 0_1,8	361 mF/Cm^2 at 0,5 mA/Cm^2 934 mF/Cm^2 at 0,5 mA/Cm^2 / 21,9 mF/Cm^2 at 0,25 mA/Cm^2	649 µW/Cm^2 2334 µW/Cm^2 / 11853 µW/Cm^2	8 µW/Cm^2 32,4 µW/Cm^2 / 9,6 µW/Cm^2	[66]
CO_2	LIG+Fe_3O_4//LIG	PI	In-plane asymmetric	PVA-H_2SO_4	0_1	719,28 mF/Cm^2 at 1 mV/s	0,75 mW/Cm^2	60,20 µW/Cm^2	[65]
CO_2	PDMS+PI+ ZnP Ink PDMS+PI+ZNP	PDMS	In-plane	PVA-KCL	0_0,6	4,9 F/Cm^2 at 1 A/g	12,5 mW/kg	145 mWh/Cm^2	[60]
CO_2	H_3BO_3-B-LIG	PI	In-plane	PVA-H_2SO_4	0-1	16,5 mF/Cm^2 at 0,05 mA/Cm^2	/	/	[67]
CO_2	LIG/KC (KOH Cristal) LIG/KS (KOH Solution)	PI	In-plane	PVA-H_3PO_4	0_1	30,06 mF/Cm^2 32 mF/Cm^2 at 0,05 m A/Cm^2	/ /	4,01 µWh/Cm^2 4,27 µWh/Cm^2	[68]
CO_2	LIG/MOS_2	PI	In-plane	PVP-NaCl	-1,4_-0,4 0_1	/	/	/	[69]
CO_2	N-LIG	M/PI	In-plane	PVA-H_2SO_4	0_1	35,20 mF/Cm^2 at 0,05 mA/Cm^2	0,025 mW/Cm^2	4,89 µWh/ Cm^2	[70]
CO_2	d-LIG	PI	In-plane	PVA-H_2SO_4	0_1	19,8 mF/Cm^2 at 0,05 mA/Cm^2	/	/	[71]
CO_2	NB-dLIG	PI	Sandwich	PVA-H_2SO_4	0_1	40,4 mF/Cm^2 at 0,05 mA/Cm^2	/	5,61 µWh/Cm^2	[72]
CO_2	NP3-H3PO4-LIG-3.5	PI	Sandwich	PVA-H_2SO_4	0_1	69,7 mF/Cm^2 at0,05 mA/Cm^2	/	9,67 µWh/Cm^2	[73]
CO_2	Co_3O_4-NLIG	PI	Sandwich	PVA–H_3PO_4	0_1	17,96 mF/Cm^2 at 0,5 mA/Cm^2	0,05 mW /Cm^2	2,49 mWh /Cm^2	[73], [74]
CO_2	MnO_2/LIG-W	PI	In-plane	PVA-KOH	0_1	15,04 mF/Cm^2 at 5 mV/s	1,278 mW/Cm^2	1,22 mWh/Cm^2	[75]

CO_2	B/LIG_6 N/LIG_6	PI	In-plane	PVA-H_2SO_4	0_0,8	60,6 mF/Cm² 54,5 mF/Cm²at 0,08 mA/Cm²	/ /	5,393 µWh/Cm² /	[76]
CO_2	ZnO/LIG	PI	In-plane	PVA-KCL	0_1	0,98 F/Cm² at 0,007A/Cm²	0,110 W/Cm²	0,07 Wh/Cm²	[77]
CO_2	P-LIG	PI	Sandwich	KOH	0_0,6	206 F/g at 0,025A/g	/	/	[78]
CO_2	LIG/Co-X	PI	In-plane	PVA-H_2SO_4	0_0,8	110.11 mF/Cm² at 0,1 mA/Cm²	/	9,79 µWh/Cm²	[79]
CO_2	sLIG /O /S x-N (N laser power)	PI	In-plane	PVA-H_2SO_4	0_0,8	53,2 mF/Cm² at 0,08mA/Cm²	1,6 mW/Cm²	4,73 µWh/Cm²	[80]
CO_2	LIGNFs-1,06W	PI	In-plane	PVA-H_2SO_4	0_0,8	57,96 mF/Cm² at 0,02 mA/Cm²	/	0,61Wh/Cm²	[81]
CO_2	LIG-P-20	PI	In-plane	PVA-H_2SO_4	0_0,9	55,5 mF/Cm² at 0,052 mA/Cm²	/	6,24 µWh/Cm²	[82]
CO_2	LING_25mm/s	PI	In-plane	PVA/H_3PO_4	-0,5_0,5	1260 mF/Cm² at 10mV/s	/	/	[83]
CO_2	LIG/Co_3O_4-m	PI	In-plane	PVA-H_2SO_4	0_0,8	10,9m F/Cm² at 5 mV/s	0,43 mW/Cm²	286,38 µWh/Cm²	[84]
CO_2	PI/PCS/LIG	PI	In-plane	PVA.H_3PO_4	0_10	389,6 µF/Cm² at 10 mV/s	3,38 mW/Cm²	37,68 µWh/Cm²	[85]

2.2. Supercapacitors

EES devices have a pivotal impact on numerous applications such as the Internet of Things (IOTs), intelligent and portable electronics, sensors, wearable units, e-skin [86][87], and others illustrated in Figure 2.12. Supercapacitors become the major candidate among the EES devices for these applications since they demonstrate great features of high-power density, rapid charge, and discharge cycling in seconds, long lifetime of over 1 million cycles, cost-effectiveness, and safety [6][86][87], in addition to these properties, the miniaturized supercapacitors or MSCs and especially their planar design are lightweight, small size, flexible, and portable [88] thus they have been the subject of intense research interest over the past decade, due to their compact size and potential as energy storage components where can be directly integrated with silicon-based electronics on a chip, facilitating the creation of miniaturized self-powered systems [89]. However, supercapacitors have some issues; perhaps the most important is low energy density (about 5 Wh/kg) compared to batteries which is up to ~300 Wh/kg in case of Li-ion batteries [5]; hence with the discovery of graphene and since it showed outstanding properties, typically of high conductivity and significant SSA, there is a desire to solve this problem and improve the supercapacitor's overall performance using this material as supercapacitor electrodes.

As we have seen in the previous section (2.1.5.2.c), where we explain the potential of DLW technology, our objective is to use it to prepare graphene-like materials as MSC electrodes to contribute to producing low-cost and highly effective devices.

Here, we will discuss some critical points about supercapacitors, the history of their development, define their types, and present some examples of LIG-MSC applications to prove the validity of this approach in our MSC field; after discussing the supercapacitor types; the reader may have some doubt about the difference between them and batteries, thus we will try to explain this point briefly, following with a description of their design and structures. Shortly we will talk about the electrolyte as an essential component in supercapacitor devices. Finally, this

supercapacitors section ends with an explanation of their electrochemical characterizations.

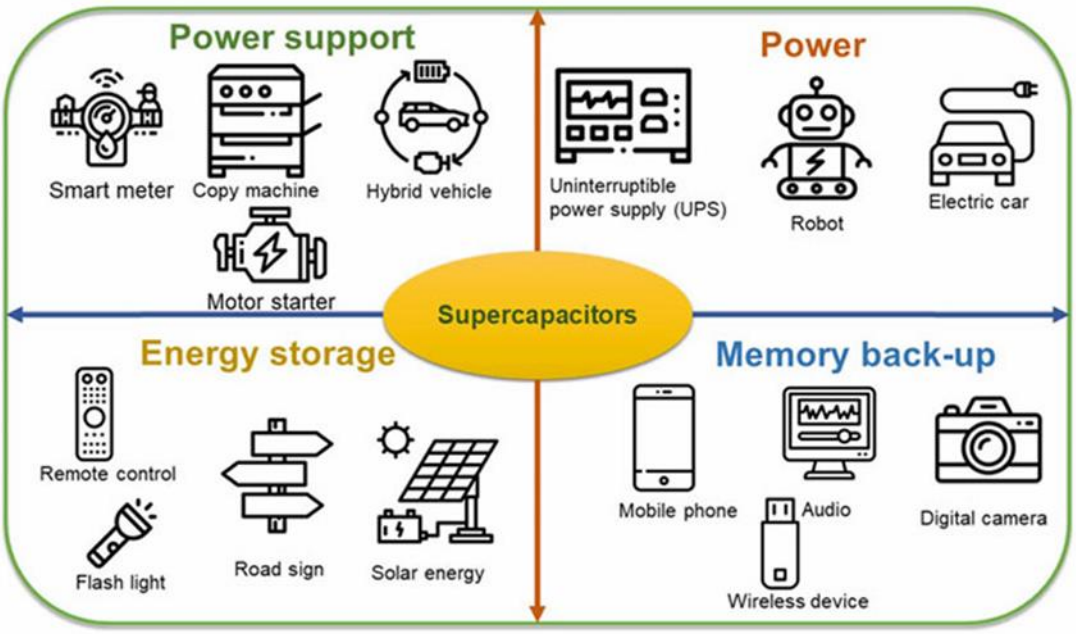

Figure 2.12: Supercapacitors functions [86].

2.2.1. Supercapacitors progression

The birth of electrochemical capacitors can be traced to the early 1800s. The Leyden jar was the first capacitor fabricated by Ewald Georg in 1745, representing an early electrical capacitor used to charge and discharge electrical energy [90]. It was made up of a bottle or glass jar with a metal foil covering both the inner and outer parts of the bottle; a conducting wire was connected to the internal foil, while the outer film was exposed to the outside of the bottle. This jar can be charged by applying discharge voltage on the inner foil from an electrical source to generate an accumulation of the electrical charge, storing the electrical energy inside and discharging it, when necessary, through the outer foil. Afterward, Benjamin Franklin fabricated a flat capacitor. Typically, it consisted of two electrode foils separated by a glass, indicating the theory of separating the two electrodes using an insulator [91]. The Helmholtz capacitor model is considered the basic building

block of the electric double-layer capacitor, which uses an electrolyte instead of the insulator to separate the two capacitor plates. By applying a voltage across the two electrodes and the electrolyte, the opposite charges accumulate on the electrodes, generating a potential difference along the layers, representing the electrical energy stored. Later, the Gouy-Chapman model produced enhancements on the previous model, using electrodes that carried an electric charge or a solid surface that results in charges from the chemical reactions between the electrodes and the electrolyte, which contains cations and anions, unlike the EDLC model. These ions hold mobility and can be managed by electric fields. The Stern model is considered an advanced Gouy-Chapman model with the same concept; however, Stern considered the adsorbed ions to be strongly bound to the charged surface [91]. In 1957, the first supercapacitor was commercialized after the pioneering electrochemical device fabricated by Becker and Ferry based on carbon material. Later, the Pinnacle Research Institute 1982 improved a supercapacitor with low internal resistance; at that time, the supercapacitor´s performance was relatively low.

In 1970, Conway introduced a new concept named pseudocapacitance, which consists of fast reversible redox reactions at the active material surface [7]. Metal oxides are an appropriate candidate for the pseudocapacitance mechanism due to their high energy and capacitance density [90]. RuO_2 is commonly used for pseudocapacitance applications owing to its conductivity and the three different oxidation states with 1,2V that can be obtained [7]. Conway and his group achieved a high pseudocapacitance using RuO_2 as an electrode material with the aqueous H_2SO_4 electrolyte [91].

In the 1990s, supercapacitors saw a huge development as they aroused the interest of researchers by studying different electrode materials and electrolytes [91]. In the 2000_s, the concept of hybrid capacitors was proposed by combining an EDLC electrode with a battery-type electrode to profit from the advantages of both electrode types and achieve “dual high”: high energy and power density [91]. A timeline that displays the evolution of the supercapacitors over time is represented in Figure 2.13.

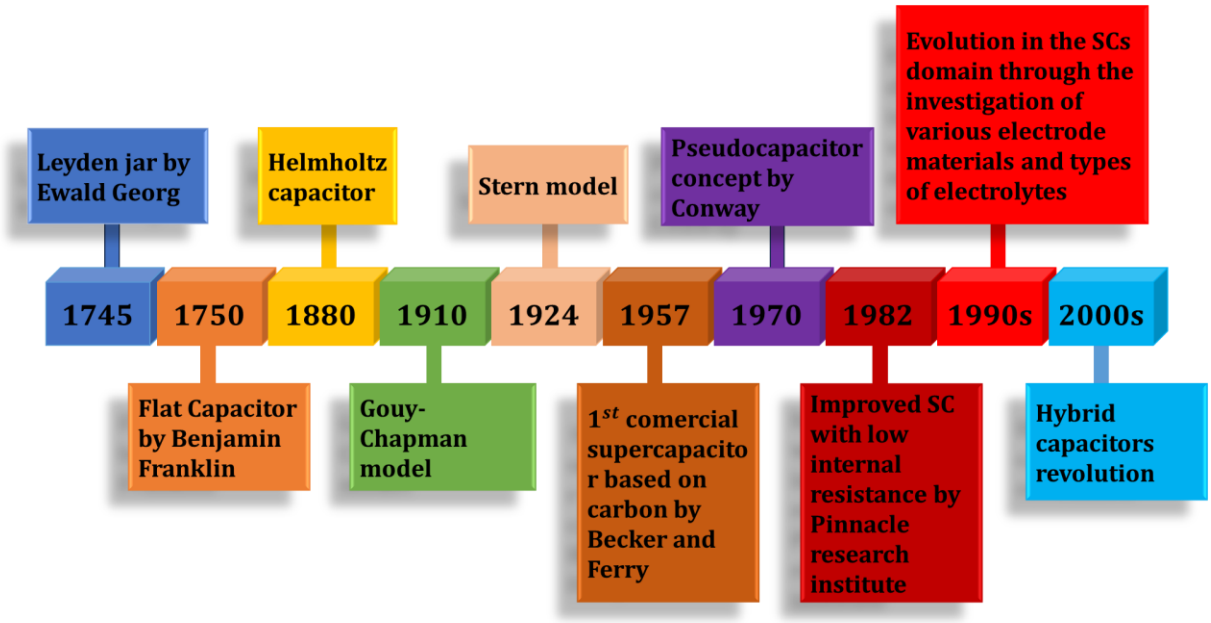

Figure 2.13: Supercapacitors progression timeline.

2.2.2. Type of supercapacitors

Based on the working mechanisms and the electrode material types, supercapacitors can be classified into two main categories: electric double-layer capacitors and pseudocapacitors [91] presented in Figure 2. 14. EDLCs physically store energy by accumulating charge through the reversible non-faradaic adsorption/desorption of electrolyte ions onto electrochemically stable surfaces at the electrode-electrolyte interface [6][92], due to the absence of chemical reactions and material transformations during charge and discharge cycles; these devices offer a longer cycle life comparing to the pseudocapacitors device. The critical factor in achieving high capacitance is utilizing electrode materials that are both electronically conductive and highly accessible in terms of surface area [93], such as activated carbon, carbon aerogel, carbon nanotubes, graphene, laser-induced graphene, laser-reduced graphene oxide…etc. El-Kady et al.[54] produced a low-cost and high performance LrGO based ELDCs which exhibited a high electrical conductivity (1738 S/m), a specific surface area (1520 m^2/g), an energy density of 1,36 mWh/cm^3 and a power density around 20 W/cm^3. Pseudocapacitors have a

different energy storage mechanism than EDLCs; they use a fast reversible faradic redox process, which increases their specific capacitance and energy density but reduces their lifetime compared to the EDLCs. Conductive polymers such as polyaniline, polypyrene, polythiophene, and metal oxides like RuO_2, Fe_3O_4, or MnO are examples of electrode materials used in pseudocapacitors, Tour et al.[64] fabricated high-performance pseudocapacitors by electrodeposition of the pseudocapacitor materials manganese dioxide (MnO_2) or ferric oxyhydroxide (FeOOH), and polyaniline (PANI) on LIG surface in order to fabricate the symmetric pseudocapacitors LIG–MnO_2-MSC achieved high energy density of

32,4 μWh/cm² > 1200 times than LIG-MSC, the energy density of LIG–PANI-MSC was 649 μWh/cm² 41 times higher than the energy density of pristine LIG-MSC, and the asymmetric LIG–FeOOH//LIG–MnO_2 MSC which demonstrated high level of energy density which reach 9,6 μWh/cm².

Hybrid systems provide an attractive option compared to traditional pseudocapacitors or EDLCs because they combine a battery-like electrode (energy source) with a capacitor-like electrode (power source) within a single cell [5] or a combination of two electrodes EDLC and Faradaic [93]. Correct electrode coupling can improve cell voltage, increasing Energy and power density[6][7]. As an example, about hybrid capacitors based on LIG materials H. Liu et al [65] successfully fabricated flexible in-plane hybrid MSC based on Fe_3O_4 nanoparticle anchored porous LIG-Fe_3O_4 as the anode and high capacitive LIG as the cathode. This device exhibited an areal capacitance of 719,28 mF/cm² which is higher than LIG-MSC up to 100 times and a highly improved areal energy density of

60,20 μWh/cm² at 1 mA/cm² exceeding the capabilities of most reported in-plane hybrid MSCs. It is worth mentioning that in this work, our samples are micro EDLCs, but we name them MSCs.

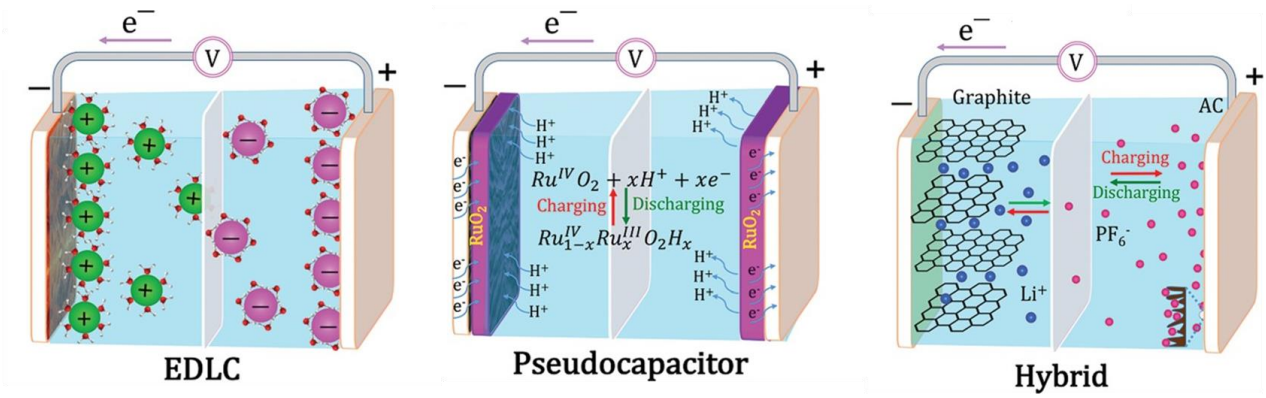

Figure 2.14: Supercapacitor types [92].

2.2.3. Difference between batteries and supercapacitors

Batteries and capacitors are two major EES devices. Batteries are composed of two separated electrodes by an electrolyte, which stores and transfers chemical energy into electrical energy via redox reactions in the bulk electrode material, causing a volume change that limits their cycle life[6]. Capacitors are the simplest form of EES devices; they are composed of two parallel plates, one has a positive charge, and the other has a negative charge, separated by a dielectric, a thin insulating material; thus, the charge is stored in an electric potential energy form between these two plates [93]. As we have seen in the previous section, supercapacitors are the upgraded version of capacitors, and they are classified in principle into 2 main types: EDLCs and pseudocapacitors, in addition to the hybrid devices between these two types or one of them and batteries, which is the hybrid capacitors. The critical point in the difference between batteries and supercapacitors is explaining the difference between batteries and pseudocapacitors, where both of these two types store energy via redox reactions; however, unlike batteries, pseudocapacitors store energy via surface fast reversible redox reactions at the electrode-electrolyte interface thus why it is so critical to use electrode materials with high SSA and due to the rapid redox reactions the charge-discharge rate is faster, the energy density is lower, and their cycle life is longer comparing to batteries. In Table 2.2, a comparison between the features of supercapacitors and batteries is presented.

Table 2.2: Comparison between batteries and supercapacitors [94].

	Battery	Supercapacitor
Recharge cycle lifetime	< 10^3 cycles	> 10^6 cycles
Self-discharge rate	5%	30%
Voltage	3,7 V-4,2 V	0 V-2,7 V
Energy density (Wh/kg)	high (20-150)	low (0,1-10)
Power density (W/kg)	low (50-300)	high (500-400)
Fastest charging time	hours	sec~min
Fastest discharging time	0,3~3 hours	< a few min
Charging circuit	complex	simple

2.2.4. Design and structures

A supercapacitor is based on four key elements: (i)**Electrodes** are two conducting materials with a high surface area and porosity [95] that can be the same type or different, separated by (ii) an **electrolyte** that enables the ion's movements between the electrodes. (iii) The **current collectors** collect and transfer the current from the electrode and distribute it to the external circuit, connecting the flow of electrons from the active electrode material to the external circuit. The effectiveness of a high-performance supercapacitor system depends on the current collector's ability to demonstrate excellent conductivity along electron routes, form adhesive contact with the electrode material, remain stable throughout the charging/discharging process, and showcase corrosion resistance. It usually consists of metallic foils, such as nickel, aluminium, and copper, with thicknesses ranging from 20 to 80 µm. Furthermore, metals like silver and gold are renowned for their high metallic conductivity [95][9]. (iiii) The **separator** is a membrane that allows ions to move between two electrodes in a supercapacitor. It plays a crucial role in determining the device's performance, including its energy density, power density, self-discharge, and cycle life. Choosing the right separator is essential to ensure

optimal performance. A suitable separator should have appropriate resistance, ionic flow permeability, optimal thickness and porosity, proper interfacial contact, affordability, chemical stability, and electrolyte retention capability. The thickness of the separator is the main difference between the two supercapacitor structures [95]. In sandwich supercapacitors, the two electrodes are stacked on top of each other and separated by a material that isolates them. Meanwhile, the in-plane structure design typically consists of interdigitated fingers separated by a gap to disconnect them from each other.

Figure 2.15 presents the essential elements in a supercapacitor device and the two different types of structure. There is a significant contrast between the two architectures in terms of size; a sandwich device is clearly thicker than an in-plane device, the time consumed for preparing a sandwich supercapacitor is longer than that we spend to design in-plane devices. In-plane supercapacitors imply a lower cost compared to the sandwich ones since in the case of the first structure, represented in Figure 2.15.a, the working area of the two electrodes stands for the same area. However, the electrodes in the sandwich design, represented in Figure 2.15.b, are prepared in two separated areas, plus the cost derived from the need for the separator material, unlike in the in-plane architecture, where the space provides separation. Moreover, a device with one layer is supposed to be more flexible than a device with double layers. The sandwich type has a low power density compared to the in-plane, considering that the ion path diffusion between two stacked electrodes is longer than the path between two neighboring fingers, hence increasing the internal resistivity and decreasing the power density. Finally, the sandwich device is thicker; thus, the current collector ought to be wide enough to support the two electrodes besides the separator, which could reduce the amount of the transferred current.

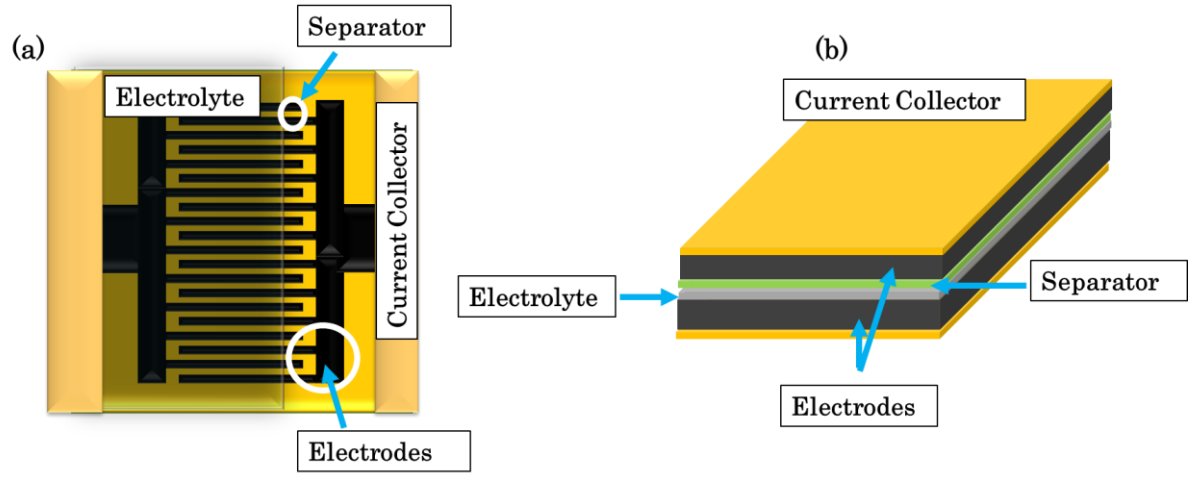

Figure 2.15: Supercapacitor structures and their composites. (a) In-plane interdigitated fingers, and (b) The sandwich structure.

2.2.5. Electrolytes

Electrolytes are substances that are usually in a solution form containing acids, bases, or salts [96]. These elements play a crucial role in improving the electrochemical performance of SCs by enhancing their energy and power densities. While electrode materials are important, the voltage stability and ionic conductivity of the electrolyte are equally critical parameters. By broadening the potential window of the electrolyte solution and increasing the cell voltage (V), we can effectively increase the energy density. As per the equation $E = \frac{1}{2}CV^2$, the cell voltage is more efficient than increasing the electrode capacitance in terms of improving energy density. This is because the best supercapacitor performance requires the energy density to be proportional to the square of the cell voltage [9]. Various types of electrolytes have been developed and reported in the literature up to now. These electrolytes are mainly classified as liquid electrolytes and solid/quasi-solid-state electrolytes. Liquid electrolytes can be grouped into aqueous, organic, and ionic liquids (Ils). Solid or quasi-solid-state electrolytes can be broadly divided into organic electrolytes and inorganic electrolytes [96]. Unfortunately, no perfect electrolyte has been developed to date, meeting all the

following requirements: (1) a wide potential window; (2) high ionic conductivity; (3) high chemical and electrochemical stability; (4) high chemical and electrochemical inertness to SCs components (e.g., electrodes, current collectors, and packaging); (5) a wide operating temperature range; (6) a good match with the electrode materials; (7) low volatility and flammability; (8) environmentally friendly; and (9) low cost. Each electrolyte has its advantages and disadvantages [96]. Aqueous electrolytes exhibit elevated ion conductivity, enhancing the power density of MSCs, yet they face limitations in terms of restricted operational voltage and diminished energy density. Organic electrolytes demonstrate an expanded operating potential range of 2,7-2,8 V [97], elevating the energy density of the devices. Nevertheless, they provide a higher resistance compared to those utilizing aqueous electrolytes. Ionic liquids have garnered considerable attention as electrolytes due to their favourable conductivity, elevated thermal stability, and non-volatile characteristics. One drawback of ionic-liquid electrolytes is their liquid state, necessitating stringent encapsulation to prevent leakage. Additionally, their liquid nature imposes constraints on their utilization in flexible MSCs. Therefore, solid-state electrolytes have been created by combining acids, salts, and ionic liquids into a polymer matrix, including materials like polyacrylonitrile (PAN), poly (vinylpyrrolidone) (PVP), poly (vinylidene fluoride) (PVDF), and poly (vinyl alcohol) (PVA). Notably, PVA is the most frequently employed; blends with H_2SO_4 and H_3PO_4 in PVA are extensively documented as the solid-state electrolyte for in-plane MSCs. However, the solid-state electrolytes should exhibit high chemical stability to prevent undesired chemical reactions occurring at the electrode/electrolyte interfaces. Additionally, they must possess good electrochemical stability to enable a broad operating potential range for the devices. Concurrently, solid-state electrolytes should demonstrate favorable mechanical flexibility, facilitating the production of flexible or stretchable MSCs [97]. Table 2.3 provides an overview of some of the widely applied liquid electrolytes in electrochemical capacitors, detailing their strengths and weaknesses.

Table 2.3:The frequently utilized liquid electrolytes in electrochemical capacitors, outlining both their advantages and disadvantages [97][96][97].

Liquid electrolytes type	Advantages	Disadvantages
Aqueous	• High level of conductivity. • High power density of the MSCs. Example: H_2SO_4, KOH, Na_2SO_4.	• Limited voltage window. • MCSs exhibit low energy density.
Organic	• Higher cell voltage. • Superior energy density. • Wide operational window range (2,5-2,7 V, dominated the commercial market). Example: tetraethylammonium tetrafluoroborate ($TEABF_4$) dissolved in the ACN or PC solvent.	• High cost. • Lower capacitance and conductivity. • Flammability, volatility, and toxicity.
Ionic liquids	• High thermal, chemical and electrochemical stability. • Negligible volatility, and non-flammability. Example: tetrafluoroborate (BF_4^-), hexafluorophosphate (PF_6^-), bis(trifluoromethanesulfonyl)imide ($TFSI^-$).	• High viscosity. • Low ionic conductivity. • High cost.

2.2.6. Electrochemical characterization

One of the most frequently employed electrochemical techniques is **cyclic voltammetry** (CV), which enables the study of electrochemical cell behavior or three-electrode setups. It can effectively determine the voltage range of electrode material in a particular electrolyte, identify the reversible or non-reversible reactions. Figure 2.16.a displays a pseudo rectangular CV curve for an EDLC device [93] [98] . The energy storage performance of the electrode active materials under practical operating conditions can be analyzed using the **galvanostatic charge-discharge** (GCD) technique. To conduct this test, a constant current is applied to the electrode, which is charged and discharged between two potential limits. During this process, the change in voltage vs. time is recorded. In the case of an ideal EDLC, a linear current response can be observed. Additionally, the CD curves are perfectly symmetric where the charging time (tc) is equal to the discharging time (td) [92][98], as shown in Figure 2.16.b. **Electrochemical impedance spectroscopy** (EIS) (Figure 2.16.c) measures the properties of the system in a quasi-equilibrium state; it measures the response of voltage or current by applying a small alternating current sinusoidal signal. Because it can sweep the frequencies, separate physical properties of the systems, such as mass transport, charge transfer, and chemical reactions, can be estimated at different reaction steps [98][92].

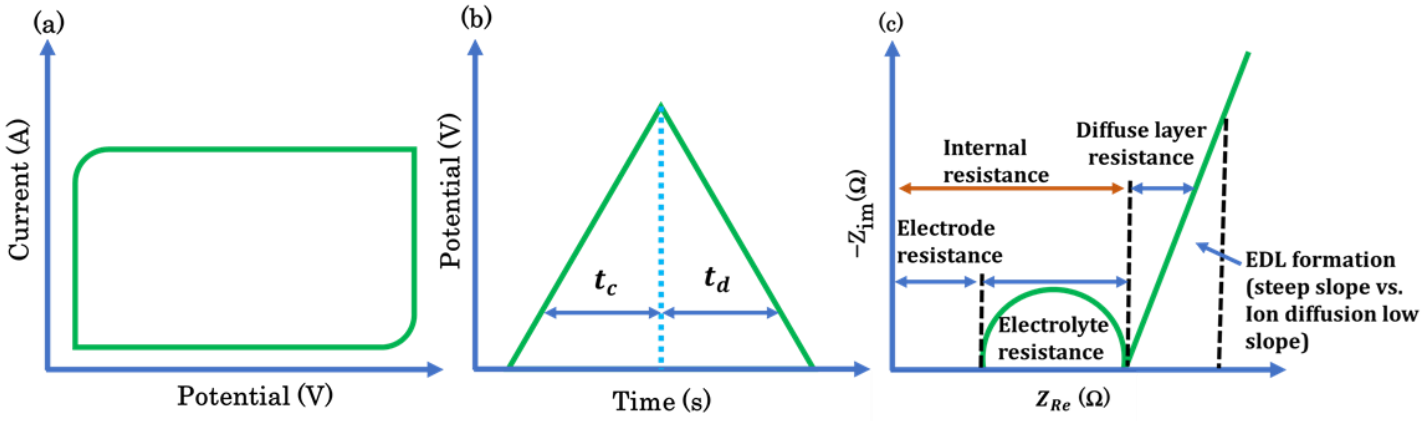

Figure 2.16: Electrochemical characterization curves for ideal EDLCs. (a) CV, (b) GCD, and (d) EIS updated from refs [93][99].

Depending on the CV data presented in Figure 2.16.a, we can calculate the capacitance, which is the ratio of the stored charges Q to the applied voltage, and the density can be calculated as a quantity of unit mass, unit volume, or unit surface [99].

- To calculate the areal capacitance C_{area} (mF/cm^2) of the, the following formula was used:

$$C_a\ (mF/cm^2) = \frac{1}{2 \times s \times v \times (V_f - V_i)} \int_{V_i}^{V_f} I(V)dV \qquad \text{Equation 2.1}$$

Where (s) is the total surface area of active electrodes (in cm^2), (v) is the voltage sweep rate (V/s), (V_f-V_i): V_f and V_i are the potential limits of CV curve, $\int_{V_i}^{V_f} I(V)dV$: the integrated area from CV curves.

From GCD results, we can calculate the energy and power values.

- The areal energy density E_{area} (µWh/cm^2) can be calculated using the following equation:

$$E_{area} = \frac{1}{2} \times C_{area} \times \frac{(\Delta V)^2}{3600} \qquad \text{Equation 2.2}$$

Where $\Delta V = V_{max} - V_{drop}$. Here, V_{max} is 1V for aqueous electrolytes, and V_{drop} is the voltage drop produced after reversing the current flow in the GCD curve.

- The areal power density P_{area} (mW/cm^2) can be determined using the following equation:

$$P_{area} = \frac{E_{area}}{\Delta t} \times 3600 \qquad \text{Equation 2.3}$$

where Δt is the discharge time in seconds.

Cycle life tests are an essential way to estimate the lifespan of supercapacitor devices. These tests usually involve a constant current profile where the devices are charged and discharged at a constant current between the rated voltage and a

defined end-of-discharge voltage. For this purpose, a percentage of the rated voltage is selected arbitrarily, usually one-half or one-third of the rated voltage. At regular intervals, the basic properties of the supercapacitors are assessed after a specific number of complete charge and discharge cycles. Any deviations are approximated, and the assessment is terminated based on how much the capacitance drops compared to the initial value [100].

3. Materials and methods

This chapter will explain the methods used for developing the research in this thesis by describing in detail the materials, techniques, and methodology used to fabricate MSC devices, collect, and analyze data after their characterization. The research questions and objectives raised during the thesis were addressed through the fabrication of low-cost and high-performance rigid and flexible MSCs based on pristine and 2D material-doped graphene-like materials of high-quality and quantity for energy storage applications.

Here, we adopt DLW as a versatile, low-cost, eco-friendly, and fast bottom-up graphene synthesis method. Since its inception, numerous studies have proven their efficacy for the fabrication of LIG and LrGO MSC electrodes [50][49]. Under laser irradiation, the photothermal and/or photochemical mechanisms induce the conversion of the carbon precursor from sp^3-hybridized carbon atoms to sp^2-hybridization, resulting in the production of a highly 3D porous graphene film patterned as MSC electrodes in one step. The high surface area and the smooth absorption of the electrolyte into the working area enhance the performance of the device [53], [101].

The main work of this thesis is divided into four parts, three of which are a progression of the previous stage. We started from rigid pristine LIG MSCs [53] then, upgraded to flexible pristine LIG MSCs, and finally, upgraded to flexible MSCs fabricated from LIG doped with InSe. The 4^{th} part consisted of producing large area rGO for energy storage applications [32]. This study was developed in the frame of a collaboration between ISOM and CIEMAT. Our lab took care of the reduction of GO using two types of lasers, UV, and IR, and the lab from CIEMAT applied other GO thermal reduction methods. Then, according to the quality of the produced LrGO tested through the performance of different characterization techniques, we compared these two groups of methods and classified each for the appropriate energy storage applications.

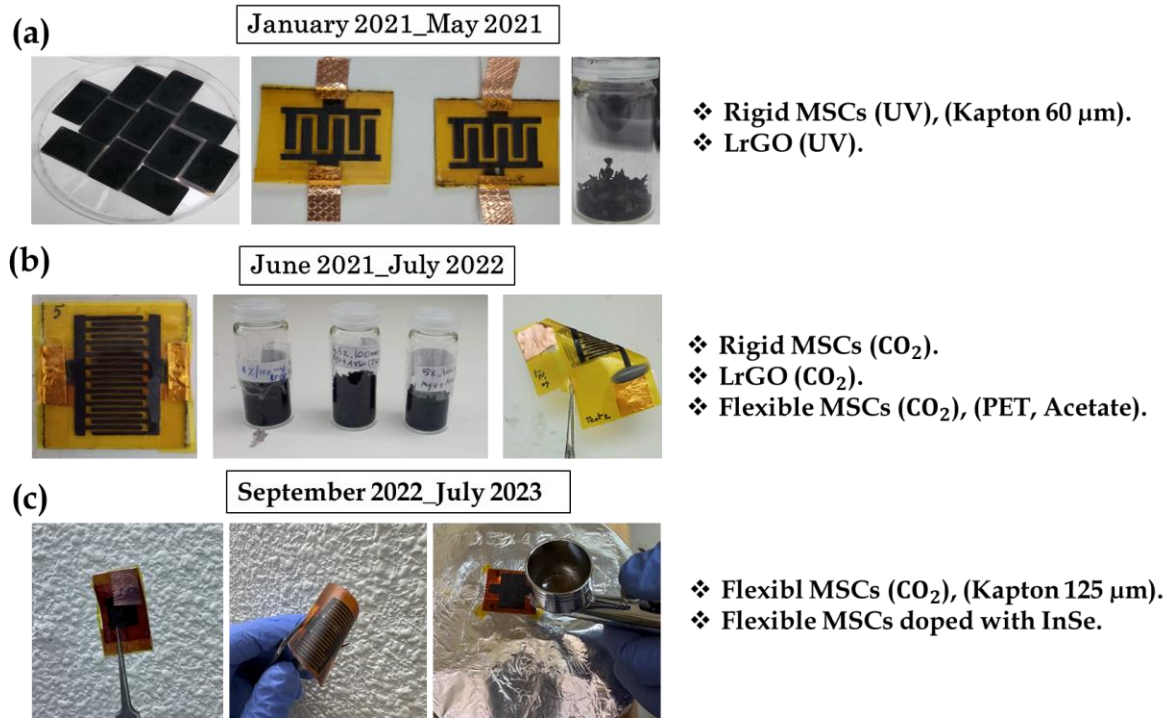

Figure 3.1: Timeline of the work developed in this thesis.

3.1. Laser-induced graphene rigid microsupercapacitors

The LIG method offers a wide range of possibilities regarding the choice of the precursor, the laser type, and the environmental conditions in which the process takes place. Therefore, after an extensive review of several research works in the LIG MSCs field, Kapton polymer, the CO_2 laser, and working in ambient conditions demonstrate significant effectiveness in producing high-performance and reproducible devices [49][60][102][103][88].

The 10,6 µm CO_2 continuous wave infrared laser was selected in this work for its unique ability to convert sp^3 C–C bonds to sp^2 C=C bonds in carbon, as sp^3 C–C has a strong absorption of infrared light in the wave numbers ranging from 700 to 1200 cm^{-1}. This process results in the formation of point-by-point porous graphene, generating a large area of 3D LIG [104]. About the precursors type choice, the study of Lin et al. [49] tested 15 polymers to investigate the appropriate choice for LIG preparation using CO_2 laser in ambient conditions. According to this study,

Kapton film, which consists in polyimide (PI)[105], is characterized by having the imide group in the monomer unit. It is highly used in the flexible electronics field. It is known for its outstanding thermal stability, chemical resistance, electrical insulation characteristics, and its mechanical strength. It has been used in numerous LIG-MSCs applications [49]. Vashisth et al. [106] also investigated a range of polymers as precursors and in this study, Kapton stood out regarding the production of LIG with high quality and interesting morphology. Consequently, we narrowed the circle of parameter choices after fixing three main factors in the work to be developed in this thesis: IR CO_2 laser, Kapton as precursor, fabrication at ambient conditions. On the other hand, the laser machine has a plethora of parameters to consider. After conducting multiple pattern tests performing MSC characterizations, and comparing their behavior in terms of electrochemical performance, we have fixed the laser scan line to d_y=75 μm and the writing at the focal distance (f= 8 mm), with the focused beam spot size being s=100 μm. Then, the optimization of the produced LIG will depend only on two main variables: i) the power measured in watts, W, and ii) the laser scan speed u_x measured in mm/s. Our laser machine has a power ranging from 1,8 W to 40 W and a maximum scan speed of 600 mm/s; as a preliminary study, we have created several LIG fingers with different powers ranging from 1,8 W to 2,4 W and scan speeds from 25 to 85 mm/s as presented in Figure 3.2.

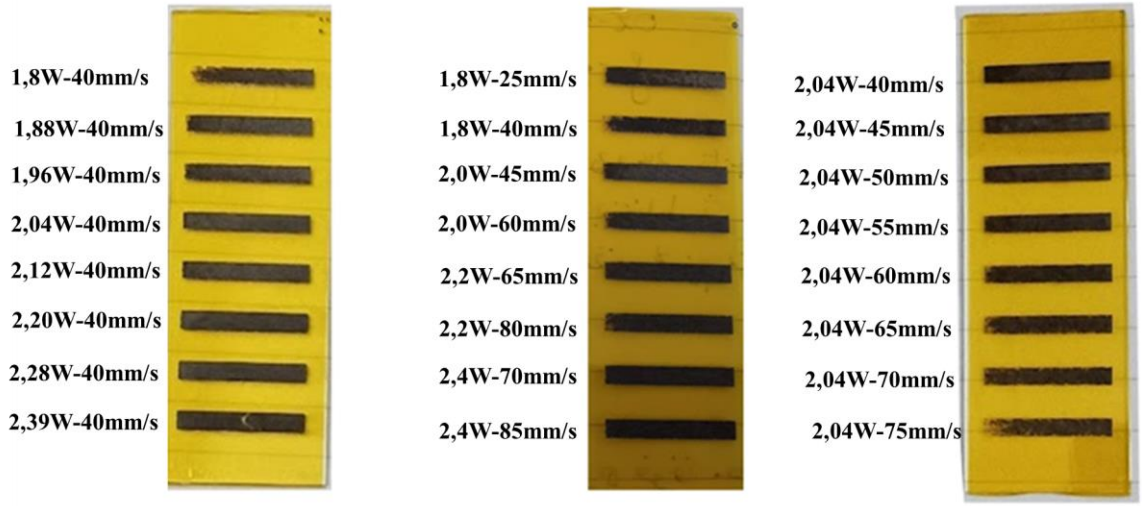

Figure 3.2: The initial calibration of the CO_2 laser parameters, power (W), and scan speed (mm/s) on the Kapton polymer.

We eliminated every resulting LIG containing non-effective transformations, cracks, and discontinuous areas, and we retained parameters that indicated higher degrees of graphitization with more transformation from yellow (Kapton color) to black color (LIG color), alongside the absence of cracks indicating a homogeneous and continuous LIG surface. However, we still had multiple LIG choices with different laser powers and scan speeds. To address this, we prepared MSCs dependent on these parameters, maintaining consistent preparation conditions such as contacts, electrolyte amount, and vacuum time. We compared each group of laser parameters with the same power but different scan speeds using electrochemical measurements. To ensure the stability of our results, we have prepared and characterized three samples for each condition. Subsequently, we selected the MSC with the best behavior for each branch. We undertook this step primarily because our goal is to enhance the performance of the MSC devices more than focusing solely on producing the best LIG quality. Additionally, electrochemical measurements provided a quicker way to examine and compare our devices than characterizing the LIG using SEM, Raman, XRD, …etc.

As a result, we chose eight laser parameters with pairs of power and scan speed values, under which promising MSCs were obtained. These pairs of power and scan speed values are represented in Figure 3.3.

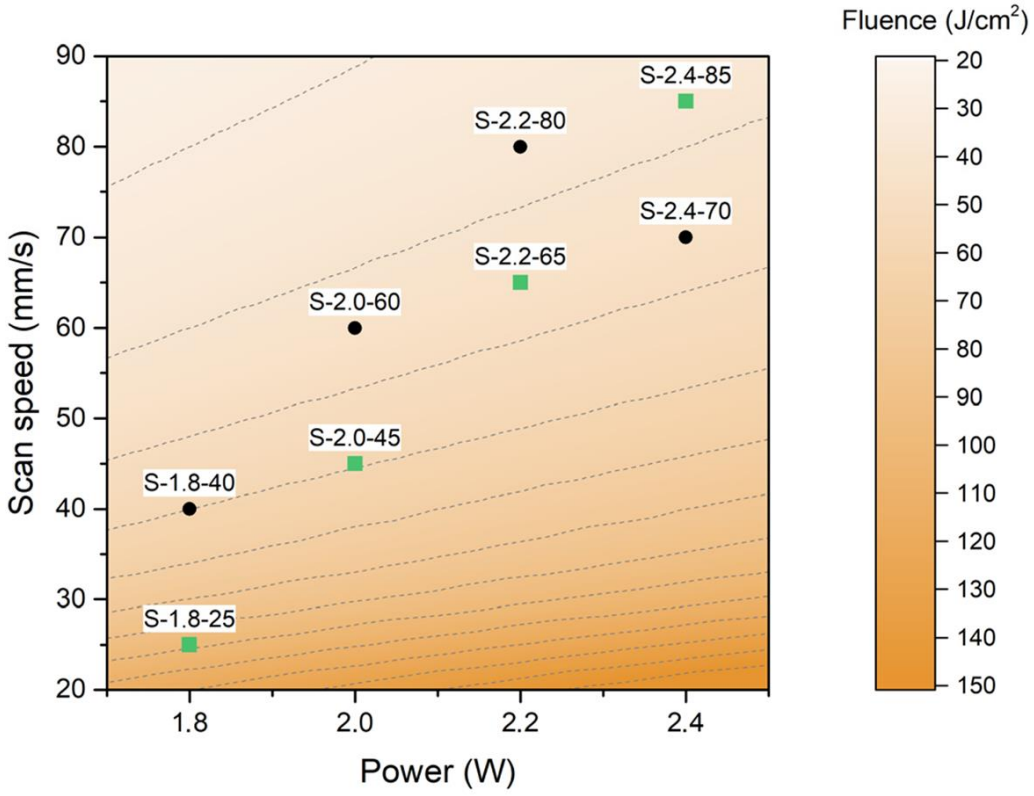

Figure 3.3: The eight chosen laser conditions after the preliminary testing of power and scan speed [4].

At this step, we introduce the laser fluence parameter (F), which refers to the quantity of energy transported per unit area within a specific time frame measured in J/cm², given by its following formula, and presented in the previous figure (Figure 3.3):

$$F = \frac{P}{u_x.s} \times \frac{s}{d_y} \qquad \text{Equation 3.1}$$

Where P is the laser power measured in watts, u_x is the scan speed, s is the laser pitch or diameter, and d_y is the step interval between lines. The product of $u_x.s$ represents a focal point moving along the x-axis, and the faster it moves, the lower

the fluence [53]. The $\frac{s}{d_y}$ ratio acts as a multiplier to account for the overlapping factor of the energy irradiated to a laser line when s is more remarkable than d_y.

It was crucial to select both power and scan speed carefully among the eight different laser conditions to maintain the material's structural integrity while achieving sufficient pyrolysis. The samples were fabricated within a specific "fluence region" using the power and speed values that produced the most adequate results. The laser conditions located toward the top left corner were found to have insufficient laser power and a too fast scan speed. This resulted in no noticeable change in the substrate and left significant gaps that broke the material's continuity. In contrast, the laser conditions toward the bottom right corner had excessive laser power and a too slow scan speed that caused internal cracks and poor material quality, thereby compromising the integrity of the pyrolyzed polymer.

To sum up, this work presents an optimization of four laser fluence conditions represented as green squares in Figure 3.3 by adjusting the power and scan speed, for the purpose of fabricating high quality LIG to use it as electrodes that are components of a MSC with a high-electrochemical performance.

3.1.1. Materials and preparation methods

3.1.1. a. Preparation of the LIG electrodes

The used laser consisted in a 40 W CO_2 upgraded cutting engraving machine laser cutter with a continuous infrared 10,6 µm wavelength, and a size of 300 x 200 mm (VEVOR® company, Germany), together with a X-Y computer control system. The used precursor was a commercial adhesive Kapton polymer sheet of 60 µm thick (Tesa®, 25 mm x 33 m, Norderstedt, Germany). The shape of an in-plane pair of interdigitated microelectrodes was designed using the Inkscape *vector graphics software.* The size of the microelectrodes finger was 0,6 mm x 10 mm. The gap between two nearby fingers was 0,45 mm. Both positive and negative electrodes

had ten fingers, being twenty fingers in total, and two pad electrodes with a size of 20,5 mm x 2 mm, resulting in a total active area of 2,02 cm^2. A scheme with the geometry of the electrodes is illustrated in Figure 3.4. Two layers of the Kapton film were fixed carefully on a clean microscope glass ensuring that no air pockets were trapped beneath to obtain a uniform LIG process. Then, the electrodes designed by Inkscape were printed on the Kapton by the laser beam under ambient conditions. In this process, in a single step, the patterning and the transformation of the Kapton to graphene by pyrolysis are achieved simultaneously.

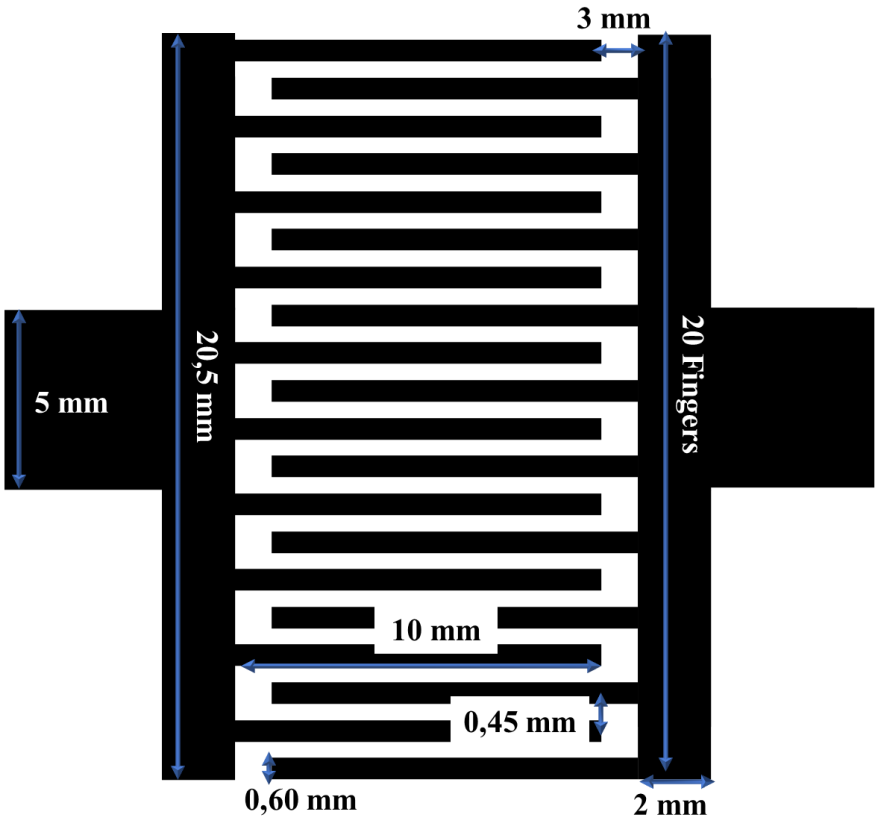

Figure 3.4: Scheme of the in-plane MSC electrodes design, where the sizes of the elements are represented.

3.1.1. b. MSCs fabrication

LIG acts as an active electrode, as well as current collector. However, for improving the electrical connectivity, silver plating (RS PRO, UK) was applied to the positive and negative electrode areas and then, pieces of conductive copper tapes (RS PRO,

10 mm x 33 m, UK) were placed on top in order to increase the length of the electrodes. Subsequently, Kapton tape was used to cover the top part of the metallic contacts, to isolate them from the electrolyte. To create the Polyvinyl alcohol : H_2SO_4 1 M gel electrolyte, a 1 M sulfuric acid solution was heated to 80°C on a hot plate. Then, 1 g of PVA (Sigma-Aldrich, 86-88% hydrolyzed medium molecular weight, US) beads were manually crushed in a mortar and added to 10 ml of the acid solution while mechanically stirring with a magnetic bead to avoid clumping. No air was introduced to the gel. After heating and stirring for 2 hours, the solution became transparent and viscous. It was then left to cool down at room temperature to allow bubbles to rise. Pictures of the described components are displayed in Figure 3.5.

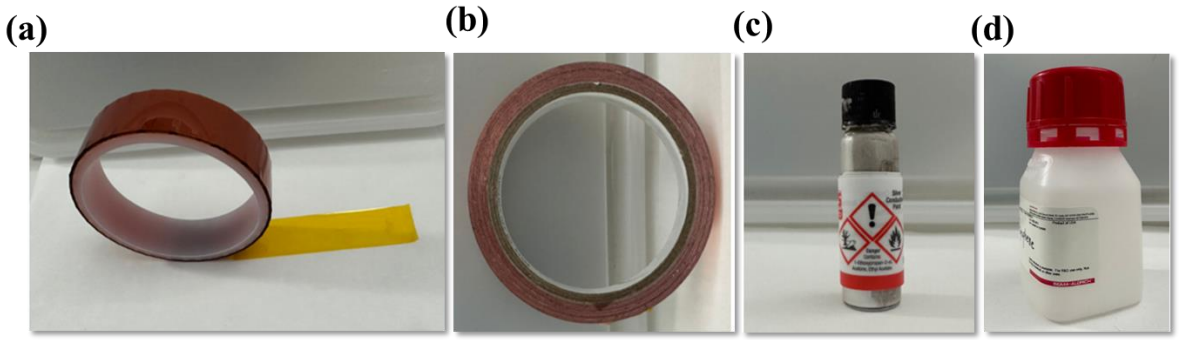

Figure 3.5: Materials used for MSC fabrication: (a) the Kapton tape used as a precursor and to protect the contacts, (b) copper tape and (c) silver paint as part of the current collectors and (d) PVA used to prepare the gel electrolyte.

The gel electrolyte was applied and spread evenly over the active area. Then, the device was placed under an active vacuum for 2 hours to remove any air from the internal pores and replace it with electrolyte. Finally, the device was left in a static vacuum overnight to ensure that the electrolyte infiltrates even the smallest pores effectively. After this step, the final device was achieved and ready to be measured. Figure 3.6 illustrates the different stages of the MSC fabrication, described in this section.

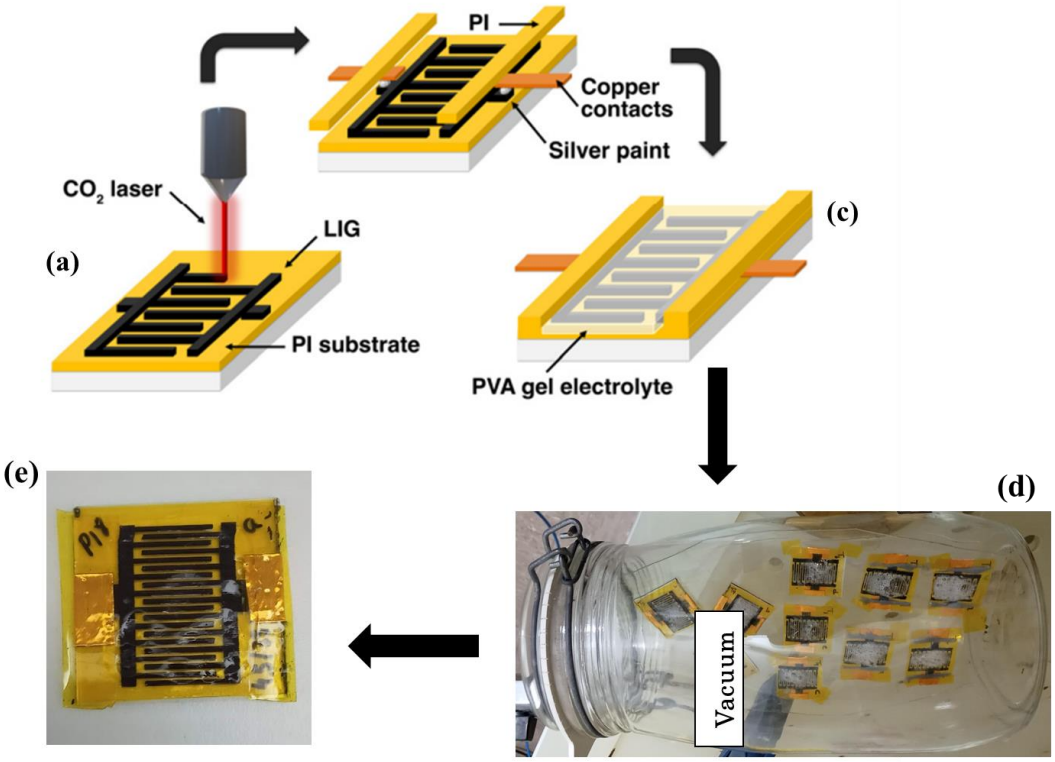

Figure 3.6: Schematic illustration of an MSC device fabricating step. (a) LIG-electrodes prepared using IR CO_2 laser on Kapton tape, (b) metallic contacts preparation and isolation, (c) gel electrolyte application, (d) samples under the vacuum process, (e) the final device after 2h active and overnight static vacuum.

3.1.2. Materials and characterization methods

3.1.2.a. LIG characterization methods

- A probe station (Karl Suss PSM 6) and a parameter analyzer (4145B, Hewlett-Packard) were used to test the electrical resistance of the samples by the two probe methods. For each laser condition, we have prepared and measured three 4 mm x 20 mm LIG fingers to provide an average value, along with its corresponding standard deviation. The purpose of this method was to take into account variations between samples.
- A scanning electron microscope (FEI inspect F50) was used to study the LIG morphology of the electrode material produced. 4 mm x 4 mm LIG squares

were fabricated eight times, two squares per condition. To prevent charging effects, an electrical path was added using silver paint and conductive copper tape. An accelerating voltage of 5 kV was applied at four different magnifications to acquire sample images for investigating the LIG structure and estimating the average pore size.

- For Micro-Raman experiments, an Ar^+ laser with a 488 nm line was used with an incident power of 7 mW. An Olympus microscope, equipped with a high optical aperture (N.A. = 0,95) and a ×20 objective, enabled a lateral resolution of less than 0,8 µm. The scattered light was filtered with a notch filter (Kaiser) and analyzed with a Horiba monochromator (1200 l/mm grating, iHR-320), which was connected to a Peltier cooled Synapse CCD. The Raman spectra were collected along two lines, each of 150 µm long, with 5 µm steps and 20 µm spacing.

3.1.2.b. MSCs characterization methods

- To evaluate MSCs electrochemical performance, cyclic voltammetry and galvanostatic charge-discharge voltage range (0-1V), were conducted using a potentiostat/galvanostat system (Metrohm, Autolab PGSTAT204, Switzerland) and Nova software. A FRA32M frequency response analyzer module of the PGSTAT204 system response analyzer has been used for the electrochemical impedance spectroscopy measurement. A sinusoidal signal applied with an amplitude of 10 mV at an open circuit over a frequency ranging from 100 kHz to 10 mHz.

All measurements were conducted in ambient conditions for PVA: 1M H_2SO_4 gel electrolytes. The following values have been determined numerically using Python code.

3.2. Laser-induced graphene flexible MSCs

Electronics technology is experiencing to shift from rigid devices to flexible and wearable devices that can be bent, rolled, or folded like clothes or accessories [107]. These flexible devices, such as flexible displays, curved mobile phones, electronic clothing, and energy storage devices, will have several advantages over their rigid counterparts, such as better durability, lighter weight, improved comfort, and higher space efficiency among emerging storage devices [108].

In this study, we have tried to upgrade and adapt our rigid MSCs to flexible devices, preserving their outstanding performance, keeping up the exact or comparable fabrication cost, and reducing the time consumption of the device preparation:

- Several flexible configurations have been used to fabricate bendable devices, including the adhesive Kapton film 60 μm thick on polyethylene terephthalate or acetate substrates, and the non-adhesive Kapton film with a thickness of 125 μm as the polymer precursor.
- We made some modifications in the electrolyte preparation protocol so that it becomes less viscous and more measurable, but still not so liquid to the point of straining and producing a leakage to the contacts.
- We reduced the vacuum time from 2 h actively and overnight statically to only 1 h actively.
- We tested two materials for the encapsulation of the devices: Fixomull and the adhesive Kapton 60 μm thick.
- We developed a setup for the mechanical test of the flexible devices.
- Finally, while adjusting the laser irradiation parameters for the fabrication of LIG flexible MSCs doped with InSe thin layers, we stumbled upon an interesting phenomenon. We found that increasing the frequency of passing the laser over the Kapton resulted in a darker color, which means a more effective conversion compared to the single-pass devices. After conducting electrochemical measurements and comparing the results between single

and double-pass devices, we observed that the double-pass devices exhibited a higher performance and more effective behavior.

We have successfully modified our protocol and obtained results by combining all the possible options and hypotheses mentioned in the above points. In this section, we will present these results in detail to demonstrate the reliability of our work. Finally, we will summarize the final protocol that was optimized for this study.

3.2.1. Refinement of the study protocol

To fabricate the flexible LIG-MSCs, first, we have used acetate (Crafter's companion, 16 cm × 25 cm, thickness =100 µm, Newton Aycliffe, UK) and PET (RS PRO, Mylar Film 75 µm, UK), coated with 60 µm thick adhesive Kapton tape, following the same protocol illustrated in (section 3.1.1.b). However, the results were neither reproducible nor stable. We encountered the issue of LIG cracks and electrolyte leakage. To solve this issue and protect the contacts, we created a small barrier using an adhesive epoxy (LOCTITE® EA 3423, IT) to isolate the area of the metal collectors from the active area of the device. We compared the results from the electrochemical characterization of these devices with the performance of flexible devices reported in the literature and the conclusion was that there was not an encouraging improvement to continue with this approach. Furthermore, the additional step of applying adhesive glue extended the fabrication time, as the glue required 3 h to dry completely, in addition to the 2 h of active vacuum exposure and overnight static vacuum maintenance after applying the electrolyte.

It is important to note that the flexibility tests were random and not accurate during this time, as we were concurrently working on developing a device to assist in adjusting the folding angle Figure 3.7 represents the work done with PET and acetate as a trial to achieve good performance flexible MSCs.

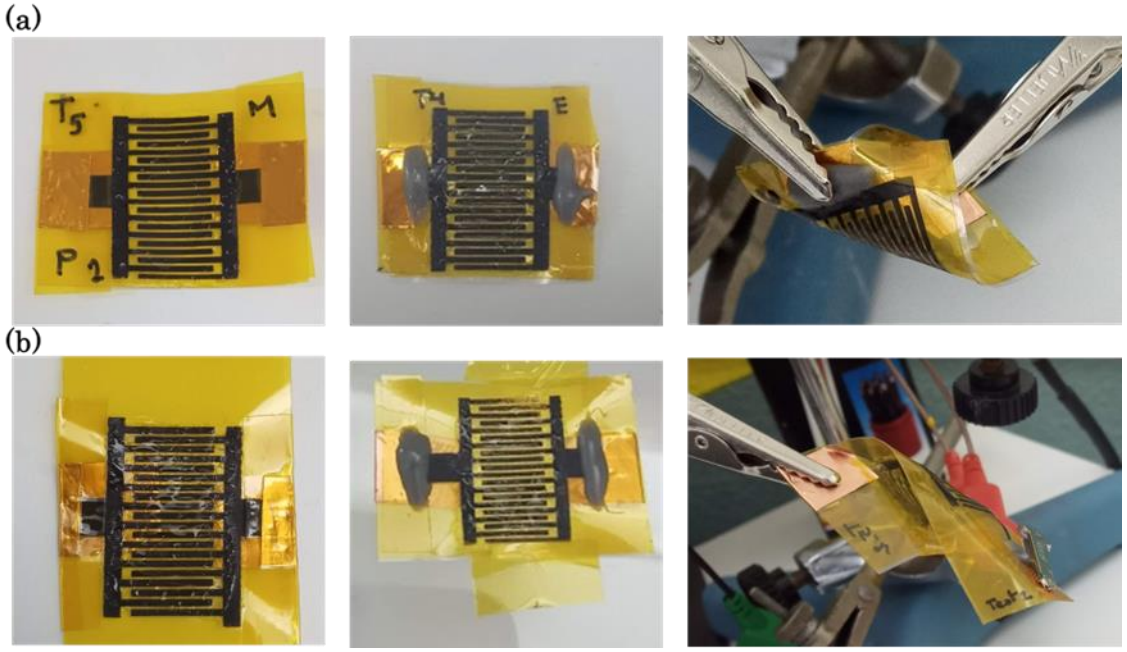

Figure 3.7: Pictures from the first trial of manufacturing flexible MSCs. (a) images presented PET samples and (b) acetate samples. (left) MSC devices are fabricated using the same protocol used in section (3.1.1.b). (center) MSC devices coated with adhesive epoxy to protect the contacts, (right) bent devices for the electrochemical characterization.

For all the above-described issues and after reviewing the literature, the non-adhesive Kapton film was the right choice for manufacturing flexible LIG-MSCs. Almost all the work that fabricates flexible MSCs based on the LIG technique, uses a Kapton film with a thickness in the range of 120 to 125 µm. For example, W. Song et al [60] used a Kapton with 120 µm thickness. Wang et al. [17] and J. Lee et al. [18] used a Kapton 125 µm thick to fabricate flexible LIG-MSCs.

Therefore, in this section, we opted for the use of non-adhesive Kapton 125 µm thick (DuPont™ Kapton® HN, 25 mm × 15 m, US) instead of adhesive Kapton 60 µm thick as a precursor (Figure 3.8.a). We employed the same continuous IR CO_2 laser, with a power of up to 40 W and an infrared wavelength of 10,6 µm, dy=75 µm (laser scan line), and s=100 µm (the focused beam size). So, our first study focused on adjusting only two variables: power and scan speed. We fabricated LIG

fingers under ambient conditions after cleaning the Kapton film with ethanol and drying it by using nitrogen (N_2).

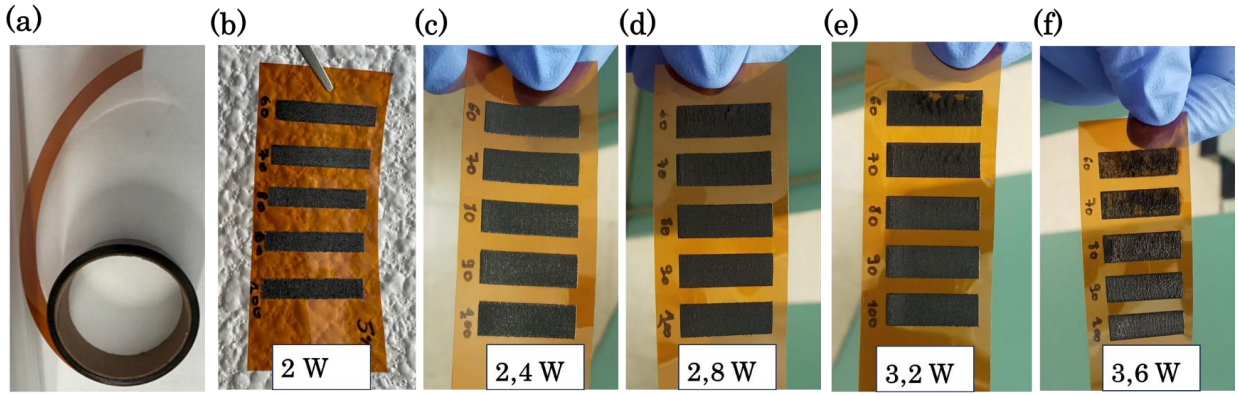

Figure 3.8: The non-adhesive Kapton 125 µm thick presented in picture (a) and an optimizing the laser power and scan rate to generate laser-induced graphene on the Kapton precursor. From left to right pictures, series of experiments increasing the power, (b) 2W, (c) 2,4W, (d) 2,8W, (e) 3,2 W, and (f) 3,6 W, from top to bottom, an increase of the scan speed is applied from 60 to 100 mm/s.

Then, as an initial estimation of the most promising conditions, we selected the darkest, most homogeneous, and continuous LIG area. We started from the lowest laser power and scan speed, which was 2 W-60 mm/s (Figure 3.8.a), where we began to observe the formation of black LIG areas and the effective transformation of the Kapton film from orange to black. Gradually increasing the power and scan speed, we noticed the volatilization of the material and the black color turning into a greyish shade. Our initial observation indicated that a power range of 2 to 2,8 W and a scan rate range of 60 to 100 mm/s (Figure 3.8.b-d) resulted in a good LIG surface area that appeared blacker, continuous, and homogeneous. At laser powers higher than 2,8 W, we began to observe defective material, as evident from Figure 3.8.e-f, where the black color is less prominent, the Kapton film's orange color is visible, and some defects are present due to the loss of LIG material. Hence, we focused on the remaining 15 pairs of laser parameter options.

To determine which of these 15 conditions generated the best performance devices, we prepared MSC device 5 samples per each laser condition to maintain the accuracy and integrity of our outcomes using the same contact preparation

methods, electrolyte amount, and vacuum time. The MSCs were divided into three groups based on laser power: the 1st group corresponding to 2 W, the 2nd group to 2,4 W, and the 3rd group to 2,8 W. For each group, we compared them electrochemically and selected the devices with good performance. The fabricated MSCs followed the same design illustrated in Figure 3.4 and the same fabrication protocol as explained previously. Among the samples fabricated, the one with 2,4 W-80 mm/s exhibited the best performance when comparing its cyclic voltammetry, galvanostatic charge-discharge, and electrochemical impedance spectroscopy, along with the areal capacitance, energy, and power, with the other fabricated devices. Consequently, we chose 2,4 W-80 mm/s to optimize the electrolyte preparation protocol, vacuum time, and appropriate encapsulated material for flexible devices.

Optimization of the electrolyte preparation process: The main goal of this step was to achieve a solution that was measurable, in order to apply a controlled and reproducible amount of volume on the electrodes. 1 g PVA 86-88% hydrolyzed medium molecular weight was added to a 20 ml mix of 1M H_2SO_4 and deionized H_2O inside a beaker. The material was then placed on a hot plate, and the solution was agitated at room temperature under 650 rpm by magnetic stirrer beads. After 30 min, the temperature was increased to 75ºC, and the stirring continued for 150 min to get a transparent and homogeneous solution. This resulted in a gel electrolyte less thick than the first one, presented in section 3.1.1.b. MSCs fabrication. With this new solution, we could measure its amount precisely when we applied it to the working area by using a typical syringe. For our MSCs, which had an electrode active area of 2,02 cm^2, 0,20 ml was the suitable volume, as can be observed from the cyclic voltammetry curves represented in Figure 3.9. According to several studies, an electrolyte amount ranging from 0,20 to 0,25 ml is sufficient for our devices depending on some literature that has a comparable working area [67][68].

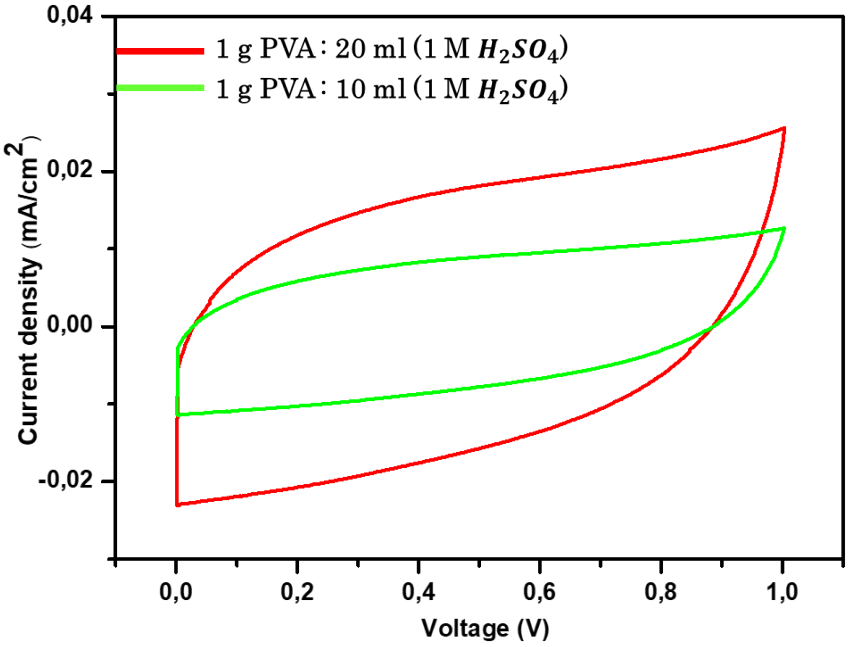

Figure 3.9: CV at 0,05 V/s comparison of two LIG-MSCs fabricated with 2,4 W of power and scan speed 80 mm/s. Coated with 0,20 ml two different electrolytes followed with 2 h of vacuum and overnight statistic vacuum. Red curve electrolyte: 1 g PVA:20 ml (1 M H_2SO_4). Green curve electrolyte: 1 g PVA: 10 ml (1 M H_2SO_4).

Vacuum time optimization: To shorten the vacuum time, we conducted a comparison between two MSCs that were produced under the same conditions of laser parameters (2,4 W-80 mm/s) and the same optimized electrolyte amount (0,20 ml). We then subjected both samples to vacuum treatment. The first sample was placed under active vacuum for only one hour (blue curve from the cyclic voltammetry graph represented in Figure 3.10.a), while the second was put under active vacuum for two hours and then left in static vacuum overnight (orange curve from the cyclic voltammetry graph represented in Figure 3.10.a). The result from Figure 3.10.a shows that using only 1 h of active vacuum is enough to achieve a better or comparable performance than using longer times. Therefore, the vacuum time optimization is achieved. Beyond this experiment, we attempted to utilize various gel drying techniques, such as air drying [109] and by using a hot plate [69], which have been used in certain studies. However, the air-drying method was too time-consuming, taking overnight to complete, and our aim is to reduce the

time taken. Using a hot plate was faster, but the temperature easily damages the wet LIG area as shown Figure 3.10.b.

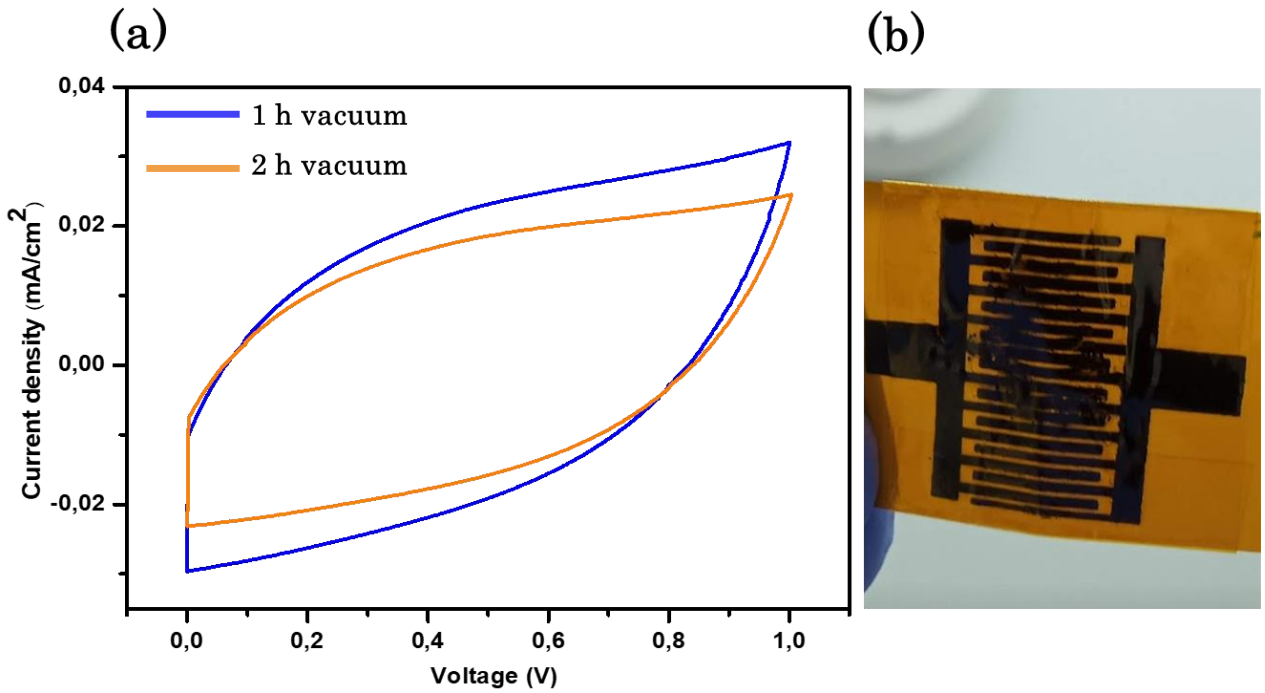

Figure 3.10: (a) CV at 0,05 V/s comparison of two LIG-MSCs fabricated with 2,4 W of power and scan speed 80 mm/s. Coated with 0,20 ml with the same electrolyte. Blue curve 1 h of vacuum. Orange curve 2 h active vacuum and overnight statistic vacuum. (b) Example of sample dried the electrolyte on a hot plate 70 ºC for around 5 min.

Encapsulation: To simultaneously ensure the user's safety during mechanical testing and extend the lifetime of the flexible MSC device, it must be encapsulated because this step helps to prevent the gel from drying out and from causing electrolyte leakage. In our study, we used two materials for encapsulation: the adhesive Kapton 60 µm thick, and Fixomull (Leukoplast, Fixomull® transparent, 10 cm × 2 m). Fixomull, shown in Figure 3.11, is a transparent medical tape that is waterproof and has adhesive properties. The tape is attached to a protective film [110][111].

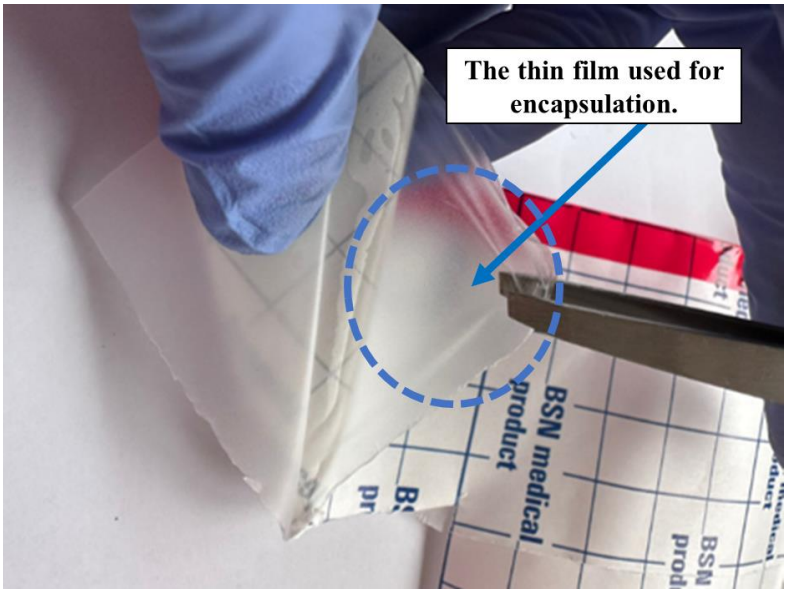

Figure 3.11: Fixomull the medical tape alongside a clarification of the adhesive thin layer used in encapsulation.

Figure 3.11 a. represents the cyclic voltammetry curves of a non-encapsulated device (blue curve), a device encapsulated with 60 µm thick Kapton (black curve) and a device encapsulated with Fixomull (green curve). We also have determined the best protocol to encapsulate the device. As it is shown in Figure 3.12.b, we have considered (a) encapsulating it directly after vacuuming (red curve), (b) allowing it to be exposed in air for a certain period in this case for 15 min (purple curve) or (c) after the first electrochemical measurement (orange curve), after this comparison we have found that running a fast CV measurement for non-encapsulated devices first is the best option. This step allows ions to create a path smoothly and efficiently inside the LIG without any force being applied from above by the encapsulation material that can make the movement difficult or not possible. Once we have completed the first CV measurement, we can encapsulate our device and proceed with the full electrochemical measurements.

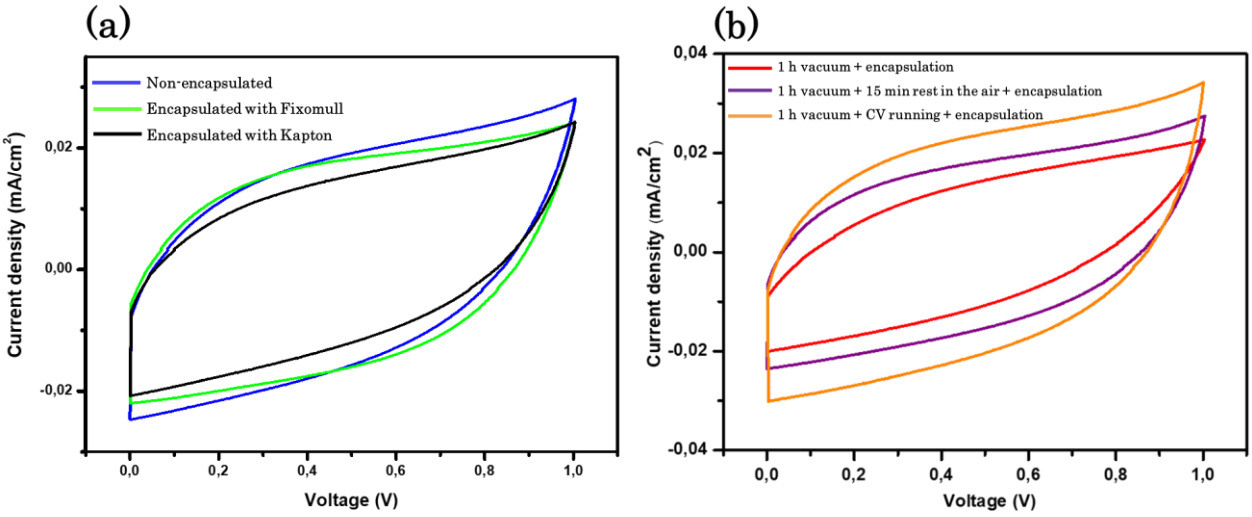

Figure 3.12: CV curves at 0,05 V/s comparison of two LIG-MSCs fabricated with 2,4 W power and scan speed 80 mm/s. Coated with 0,20 ml with the optimized electrolyte and dried for 1h vacuum. (a) Comparison to choose the best encapsulation material. The blue curve is from a non-encapsulated device, the green curve corresponds to a device encapsulated with Fixomull, and the black curve is from a device encapsulated with a Kapton film 60 µm thick. (b) Comparison to choose the best encapsulation technique after vacuum. The three curves correspond to devices encapsulated with Fixomull. The red curve corresponds to a device encapsulated directly after 1h of active vacuum, the purple curve is from a device encapsulated after 1h active vacuum and 15 min underexposure in air, and the orange curve is from a device encapsulated after 1h active vacuum and running a CV measurement.

Based on the graph in Figure 3.12.a, the three curves appear to be very similar, with the performance of the device encapsulated by Kapton slightly worse than the others. However, during the bending tests, it was observed that devices encapsulated with Fixomull were more flexible than those encapsulated with Kapton. This is because the medical tape used is much thinner than the Kapton, which has a thickness of 60 µm. Figure 3.13.a displays the homemade setup used to make the bending tests. Figure 3.13.b illustrates the stability of a CV graph for a LIG-MSC encapsulated with Fixomull tape under different bending angles.

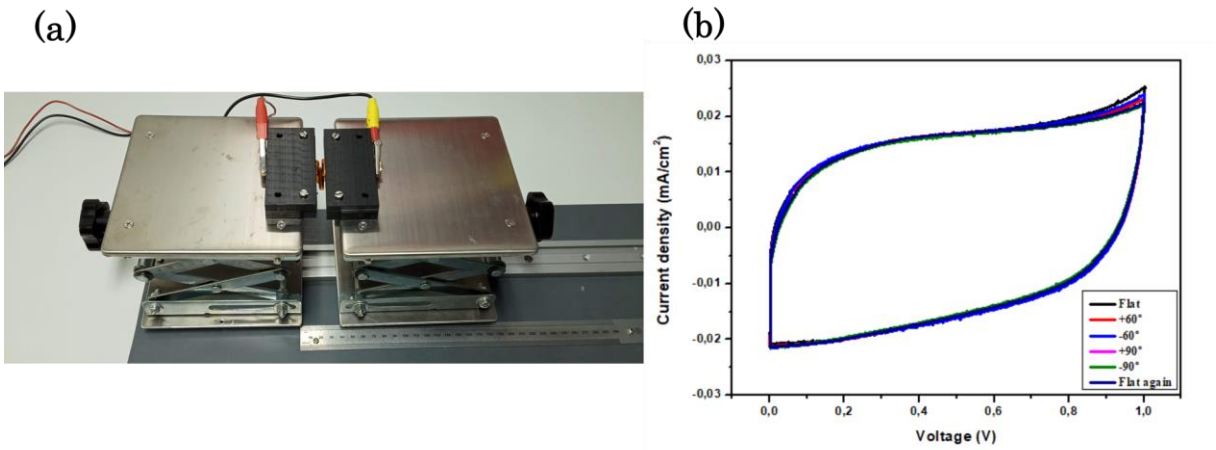

Figure 3.13: (a) Mechanical test of flexible LIG-MSCs (2,4 W-80 mm/s) encapsulated with Fixomull bent sample using a home-made setup, (b) CV graphs of different banding angles at 0,05 V/s scan rate demonstrating the stability of the device performance under the mechanical test.

From these results, Fixomull looked like a good candidate for our devices encapsulation. However, after a certain period, we noticed that the Fixomull layer become visibly wrinkled (Figure 3.14.a and c), while the Kapton layer had remained stable during this entire period (Figure 3.14.b and d). This effect caused a degradation in the performance of the device encapsulated with Fixomull over time (green curves in Figure 3.14.e), while the performance of the device encapsulated with the Kapton tape was stable over time (blue and red curves in Figure 3.14.e). We realized that Fixomull film is too thin and in addition, the material corrodes with time under contact with the electrolyte due to the H_2SO_4. For this reason, the Kapton film was chosen as the final material for the encapsulation of the supercapacitors in this study.

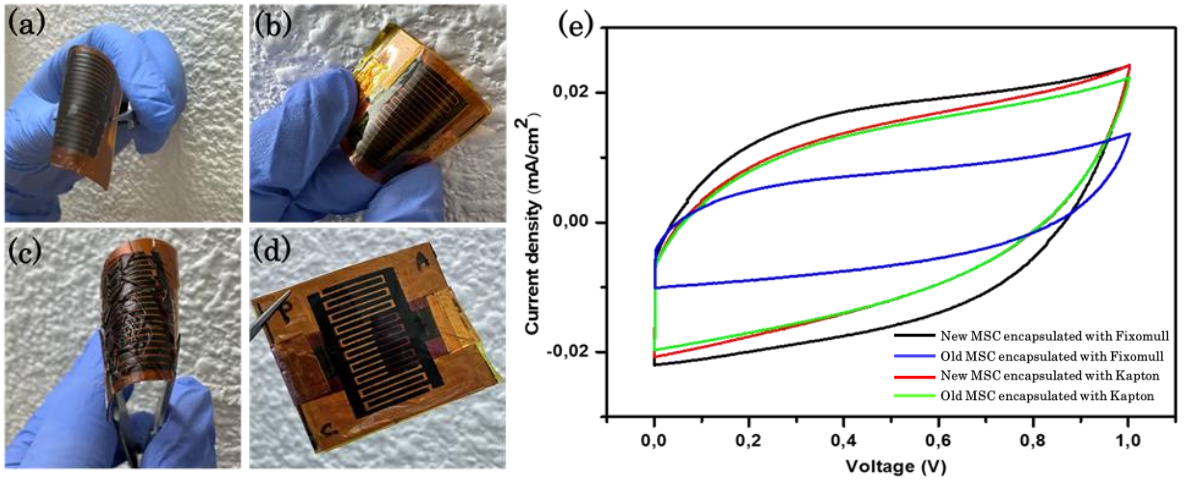

Figure 3.14: New samples encapsulated with Fixomull (a) and Kapton (b), On the other hand, (c) and (d) depict old devices that have undergone one month of fabrication and have also been encapsulated with Fixomull (c) and Kapton (d), (e) CV comparison at 0,05 V/s of the same devices when they were new and after one month of encapsulation. The black and blue curves correspond to new and old MSCs encapsulated with Fixomull, and the red and green curves refer to new and old MSCs encapsulated with Kapton, respectively.

As the final optimization step in the fabrication protocol of the LIG flexible MSCs, during our trial to adjust the laser writing conditions for the study of doping the LIG with InSe 2D nanomaterials to enhance its performance, we discovered that doubling the laser passes significantly improved the quality of the LIG material. The Kapton substrate changed from orange to a much darker black color compared to the sample made with a single laser pass. These initial results were very encouraging, and we decided to study how the number of laser passes affects the quality of the produced LIG and, consequently, the performance of the MSC device. This step can be applied quickly using the laser controller software. There is an option in the program that the user can select to increase the laser pass number. Thus, the laser will write the design of the electrode on the Kapton in the first pass, generating the LIG and then, automatically will start the second pass, overwriting the design on the same place for the second time and so on. This is equivalent to a multiple pyrolysis cycling, this results in an identical LIG geometry better then to do it manually because once the laser is turned off, it is impossible to restart it from the same initial point; this will make a short cut especially in the MSCs interdigitated designs.

3.2.2. Materials and preparation methods

3.2.2.a. Preparation of the LIG electrodes

A piece of the commercial non-adhesive Kapton film of 125 μm thickness is cleaned with ethanol and dried with N_2. Then, the CO_2 laser converts the material from polyimide to graphene by pyrolysis and draws the geometry of the electrodes simultaneously in a single step, under ambient conditions. We fabricated in-plane LIG-MSC electrodes with the following conditions: two laser passes applied with a laser scan line d_y = 75 μm, and the focused beam size of 100 μm. The design of the electrodes is the same as the one used previously for the rigid devices, shown in Figure 3.4. Three different powers: 2,0 W, 2,4 W, and 2,8 W and a fixed scan speed of 80 mm/s.

3.2.2.b. MSCs fabrication

The new protocol for fabricating flexible LIG-MSCs used in this part can be summarized in the following points and in the scheme illustrated in Figure 3.15

- Cleaning the 125 μm Kapton film with ethanol and drying it with N_2.
- Fixing a piece of the cleaned Kapton flat and straight on top of an 8 mm thick metal plate.
- Preparing the LIG MSC electrodes as explained in section 3.1.1.b. However here we applied the laser treatment two times.
- Reinforcing the contacts using silver paint, copper tape, and covering them with Kapton tape to isolate them from the contact with the electrolyte.
- Applying 0,20 ml of the gel electrolyte, which composition is 1 g PVA: 20 ml 1 M H_2SO_4+H_2O, on the LIG electrodes.
- 1 h of active Vacuum.
- Running a CV conditioning measurement.
- Encapsulating the device with the adhesive 60 μm Kapton.

- Applying full series of electrochemical measurements.

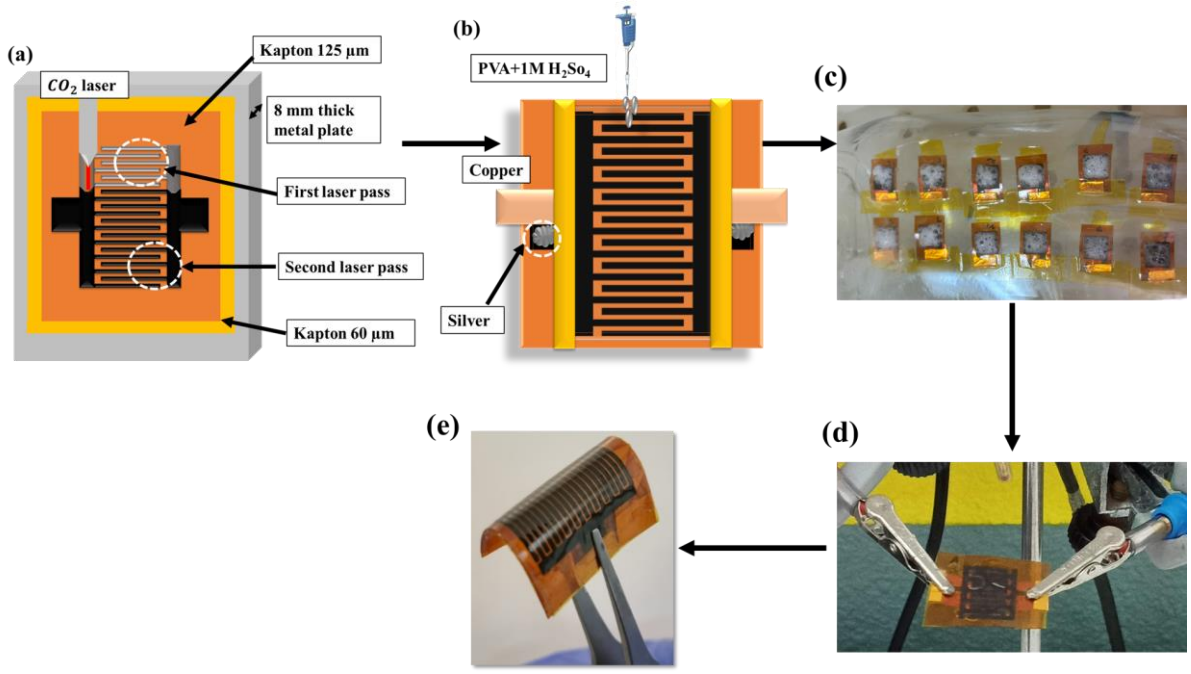

Figure 3.15: A schematic drawing illustrates the steps in preparing flexible LIG-MSCs. (a) application of double laser pass, (b) preparation of contacts, (c) flexible LIG-MSCs under active vacuum, (d) LIG-MSC device during CV measurement, following with (e) encapsulation using Kapton 60 µm.

3.2.3. Materials and characterization methods

3.2.3.a.LIG characterization

- The morphology of the LIG electrode material was studied using a scanning electron microscope (FEI inspect F50). Six 4 mm x 5 mm LIG squares were fabricated, one square per condition. The used parameters are shown in Figure 3.16. Using silver paint and conductive copper tape, an electrical path was added to block charging effects during the measurement. Secondary electron images were taken at five different magnifications with an accelerating voltage of 5 kV to investigate the LIG structure and compare

the pore size between the samples fabricated applying different powers and the single and double laser pass.

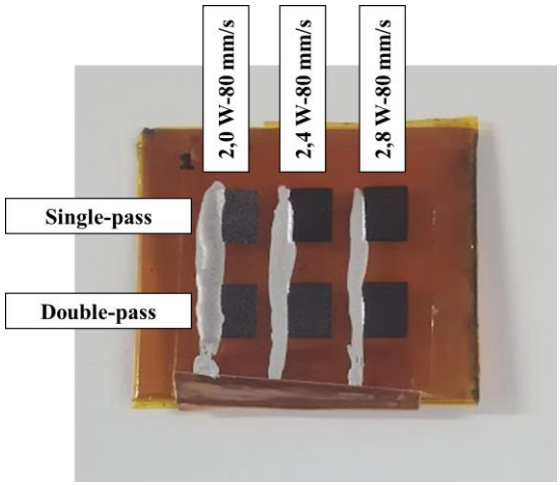

Figure 3.16: Sample used for SEM characterization.

- The quality of the produced LIG under the different conditions was studied by Raman spectroscopy (Horiba LabRam HR, Japan), with a magnification lens of ×10, an ND filter of 50%, and a laser wavelength of λ = 532 nm. To obtain reliable and consistent results for single and double-pass LIGs, three fingers of 5 mm x 15 mm were fabricated and measured for each laser condition. Some of these samples are shown in Figure 3.17. To ensure accuracy, each spectrum was obtained using 5 accumulations and 20 s of acquisition time. The LIG fingers were coated with silver paint and copper tape to dissipate the heat concentration under laser beam exposure.

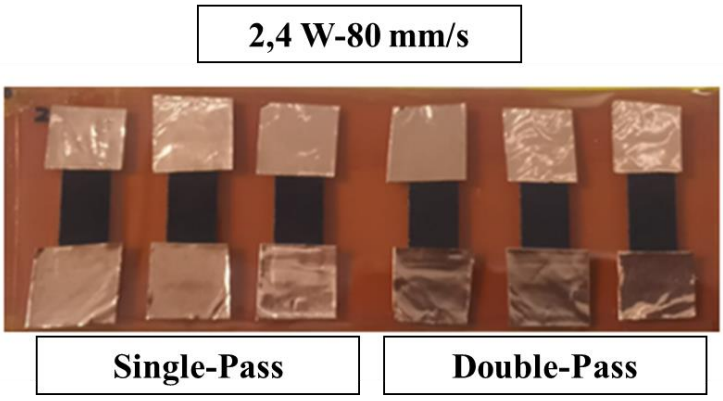

Figure 3.17: Example of one of the samples used for Raman characterization.

- X-ray diffraction (XRD) experiments were conducted using Cu Kα radiation (λ = 1,54 Å) on an X'Pert Pro diffractometer (Malvern-PANalytical). The diffractometer was operated at 45 kV and 40 mA. XRD data were collected in θ-θ configuration over an angular range of 5° to 80° with a step size of 0,017.
- The Brunauer–Emmett–Teller (BET) method with an ASAP 2020 (Micromeritics, Norcross, GA, USA) was used to determine the specific surface area and the pore volume of the LIG samples.

The LIG samples for the XRD and BET characterization were prepared for each condition by fabricating a large LIG area of multiple 5 mm × 5 mm squares, square by square, and then we peeled the produced material gently from the unmodified Kapton substrate to get the LIG powder.

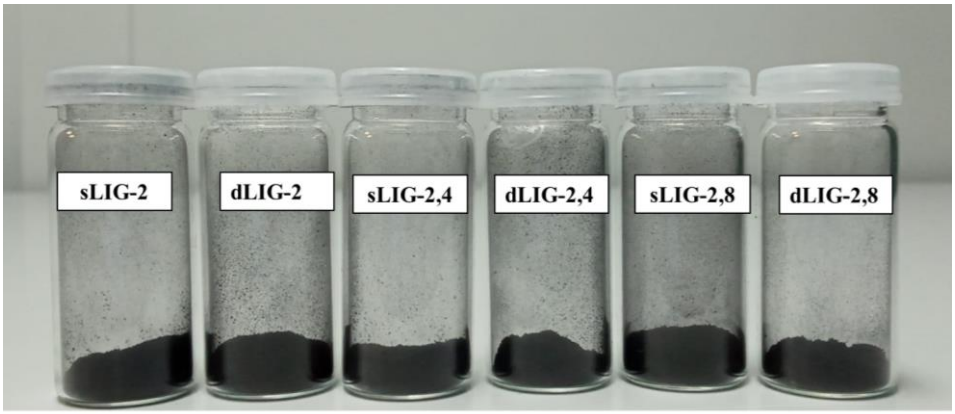

Figure 3.18: Example of LIG powder used for XRD and BET characterization.

3.2.3.b. MSCs characterization

This part is identical to the characterization method presented in (section 3.1.2.b); the only difference is the running of a CV measurement to conditioning the device before encapsulating it and the measurements under different bending angles to check that the sample behaves the same when it is relaxed and under bending. Also, another important part of the characterization of the MSC devices was the

performance of cyclability tests to study the stability over time and estimate the potential lifetime of the fabricated supercapacitors.

3.3. InSe doped laser-induced graphene MSCs

The zero-band gap of graphene limits its use in most electronic device applications. However, this can be rectified by doping it with heteroatoms, which open and tune the bandgap structure. In our case, LIG heteroatom doping is a highly efficient technique for modifying the electronic band structure of graphene. As a result, doped LIG has become a very attractive material for energy storage applications due to the formation of electrochemically active sites [57], [112].

In Table 2.1(section 2.1.6), a summary of previous studies about doped-LIG MSCs fabricated using a CO_2 laser was presented. For example, Cho et al. [59] prepared an in-plane MSC based on LIG doped with PEDOT and achieved a capacitance density of 115,2 F/g at 0,5 V/s scan rate. In another work, a gelatine-mediated ink containing Ni and Co ions was coated onto a Kapton film, and a CO_2 laser was used to get a LIG-NiO-Co_2O_4 in-plane MSC with 2,4 mF/cm^2 of areal capacitance at 10 mV/cm^2 [61]. The LIG heteroatom doping can be done symmetrically or asymmetrically, L. Li et al. [64] demonstrated this by preparing high areal capacitance symmetric in-plane devices using LIG doped with PANI and MnO_2. The areal capacitance achieved was 361 mF/cm^2 and 934 mF/cm^2, respectively at 0,5 mA/cm^2 scan rate. They also made asymmetric sandwich devices from LIG-FeOOH and LIG-MnO_2, which exhibited 21,9 mF/cm^2 at 0,25 mA/cm^2 scan rate. These devices showed significant performance improvements compared to devices made with pristine LIG. Accordingly, these results motivated us to explore LIG-heteroatom doping in our work and enhance further the performance of our flexible MSCs.

The study of Mu et al. [113] was fascinating. They used InSe nanosheets as dopant material to enhance the performance of an MSC based on graphene prepared using the mask-assisted-vacuum filtration technique, and the MSCs achieved high areal and volumetric capacitances of up to 0,72 F/cm^2 and 1,79 F/cm^3, respectively. These MSCs exhibited exceptional long-term cycling stability, retaining 93,6% of specific

capacitances after 10000 cycles. They also possessed excellent mechanical flexibility, maintaining capacitance at 98,2% after 2000 cycles under a bending angle of 90 degrees, and they had an outstanding power density of 7,31 W/cm^3 and a high energy density of 0,48 mWh/cm^3.

Besides, InSe is a well-known 2D semiconductor material boasting exceptional charge carrier mobility values, ON/OFF ratio, and efficiency in optoelectronic devices. It finds wide applications in photodetection, flexible electronics, solar cells, photovoltaics, and strain energy. InSe-based fabricated devices on flexible substrates exhibit remarkable flexibility without reducing their performance, making InSe a strong candidate for flexible electronics [114][115][116][117], [118]. In this thesis, we explored how to enhance the flexible LIG-MSCs by doping the 125 μm thick Kapton film with InSe nanosheets before and after laser passing. Figure 3.19 is an illustration of the LIG heteroatom doping methods used previously in the MSCs application.

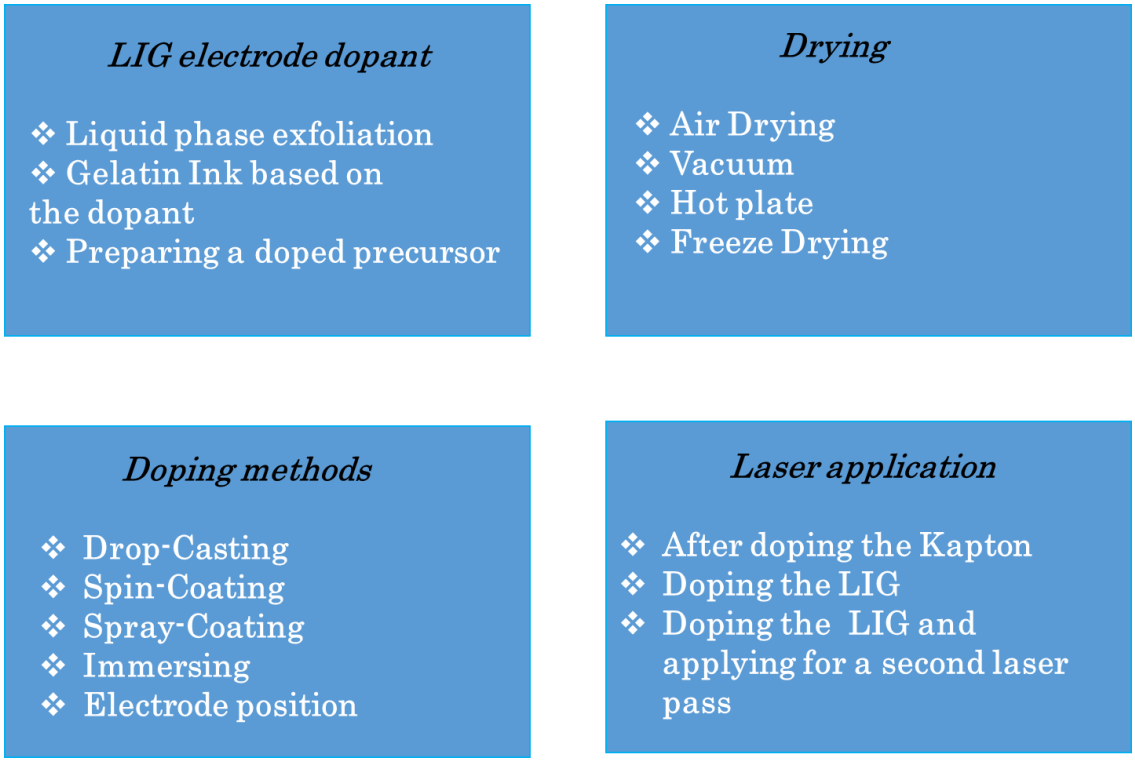

Figure 3.19: Schematic drawing of the LIG heteroatom doping methods in MSCs application presented in Table 2.1. Section 2.1.6.

As we have seen previously, our protocol was to characterize the electrodes and then choose the best electrode structure in terms of LIG quality to use them and prepare high-performance MSC devices. In the first InSe LPE experiment, we characterized the resulting InSe using atomic force microscopy, but the resulting InSe-LIG MSCs were not so promising compared to the pristine LIG MSCs. Therefore, we had several questions: which solvent is suitable to use? What are the sonication and centrifugation parameters? What are the suitable doping and drying methods? To answer these questions, we had to try all the hypotheses, but the time was very tight. For that reason, we preferred to advance the MSCs characterization step because it goes faster, and we planned that once we achieve high-efficiency MSC devices, we characterize the electrodes prepared with the same steps, parameters, and conditions that resulted in these enhanced flexible InSe-LIG MSCs.

3.3.1. Materials and preparation methods

3.3.1.a. Liquid-phase exfoliation of the bulk InSe

LPE is a top-down 2D nanomaterials synthesis method starting from their bulk counterparts. It is an effective and low-cost technique [119]. Creating nanosheets through this method may appear to be a straightforward process. It involves basically the placement of the bulk materials in solvents and the application of ultrasound treatments, followed by centrifugation [38]. However, with a plethora of solvents to choose from, it is essential to select the most suitable one. On the other hand, the sonication and centrifugation parameters such as time, power, temperature, and speed are the key factors of LPE process and the most challenging part in this study. Figure 3.20 presents a scheme of the LPE steps we have used in the preparation of the dopant InSe.

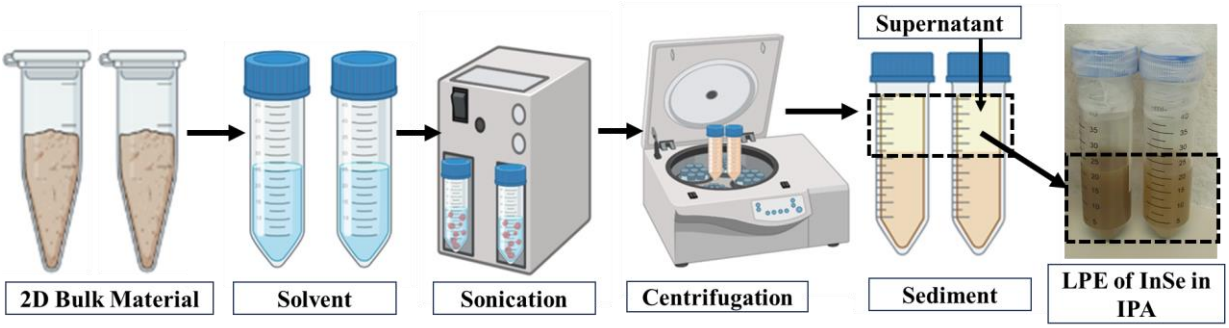

Figure 3.20: Scheme representing the general concept of the LPE method used in this work.

After reviewing in depth, the work on the LPE of 2D materials in general and of InSe specifically, Li et al. [120] achieved an optimum InSe exfoliation using NMP as a solvent. However, the use of NMP is not recommended since it is a toxic solvent, and one of our principal goals is to keep our work safe and environmentally friendly. Thus, we tried all the possible hypotheses depending on the previous studies to achieve a productive exfoliating outcome by using another solvent.

Commercial InSe powder (99,995% mw 193,78; 500 mg, Ossila, UK) can be observed from the picture shown in Figure 3.21 was used in different LPE

experiments, we tried different solvents, sonication, and centrifugation conditions in order to achieve a good exfoliation and getting InSe nanomaterial that can be used as a dopant material for our flexible MSCs and improving their performance.

Figure 3.21: InSe powder that has been used in this work.

In the following sections, we will describe all the experiments that have been done to achieve a successful exfoliation process:

1. InSe solution with 1 g/l density was prepared by solving 21,42 mg and 22,37 mg InSe powder in 21,42 ml and 22,37 ml IPA, respectively. After ultrasonication for 9 h (Figure 3.22.a), the exfoliated solution was centrifugated at 2000 rpm for 1 h [112], and the supernatants were separated from the sediments and filtrated during the weekend to remove the non-exfoliated InSe particles (Figure 3.22.b). 2 new densities resulted after the centrifugation: 0,071 mg/ml and 0,58 mg/ml.

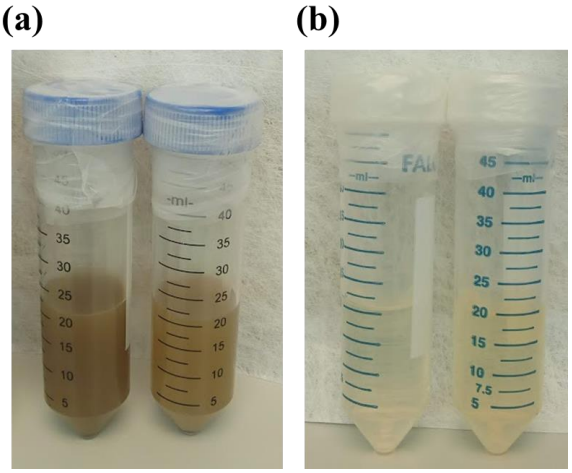

Figure 3.22: InSe flakes (a) after 9 h sonication and (b) after centrifugation under 2000 rpm for 1 h.

2. 30 mg InSe bulk and 30 ml solvent with a ratio of 60% ethanol was and 40% DI water (18 ml ethanol, 12 ml DI H_2O) which were placed first under vacuum overnight to extract the dissolved oxygen [121]. The 30 mg InSe bulk powder material with a bit of this solvent were manually ground using a mortar to have InSe powder and facilitate the sonication step, followed by ultrasonication for 12 h; after that, the plan was that the exfoliated solution will be centrifuged at 5000 rpm for 60 min to take out the large flakes. Then supernatants will carefully separate from the sediments and re-centrifugated at 1200 rpm for 40 min [122]. Figure 3.23.a presents the picture of the solution after 12 h of sonication. Figure 3.23.b shows the falcons after the first centrifugation where we faced a failed centrifugation; all the InSe flakes stuck to the wall of the falcons and the supernatant was a transparent solution as demonstrating Figure 3.23.c, We tried to re-use the same material where we returned each transparent solution to its original falcon and sonicated them again till we observed that all the material was removed from the wall (Figure 3.23.d). Then, we used this produced solution to dope the LIG.

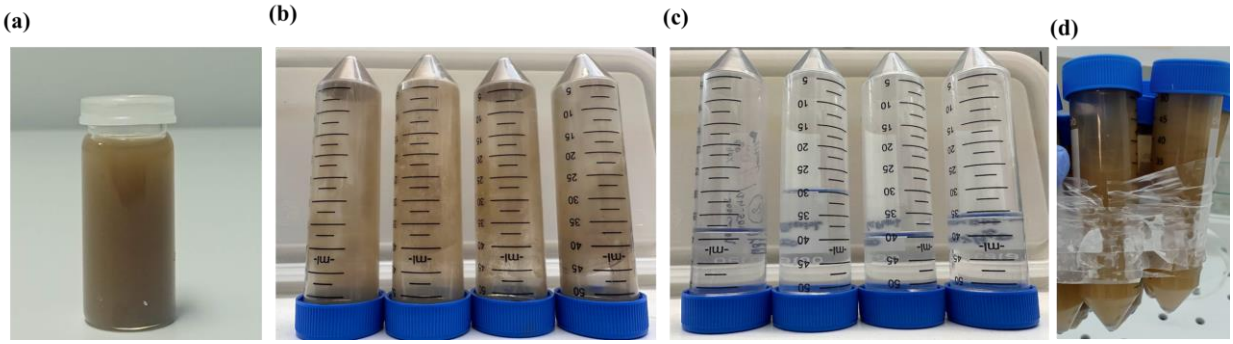

Figure 3.23: LPE of InSe in ethanol and DI,(a) the solution after 12 h of sonication, (b) Post-failure centrifugation, (c) the resulting transparent solution after sacking InSe on the Wall of the falcons, (d) the re-used solution after 3 h of sonication.

3. The centrifugation machine that we have been used for this work was at Centro de Tecnología Biomédica (CTB). The tool became inoperative. Consequently, we propose using the filter presented in Figure 3.24.a to separate the large and the small flakes after sonication to replace the centrifugation step. For this experiment, we sonicated 20 mg of InSe powder in 20 ml IPA for 5 h; the resulting solution is shown in Figure 3.24.b. After filtration, we get a transparent solution (Figure 3.24.c) suggesting the absence of InSe material. We believe that 5 h of sonication was insufficient to exfoliate the bulk InSe into thin layers. Therefore, since probably the size of almost all the material was larger than the filter size of 0,2 µm, the solution bottle after filtration would contain an insignificant number of flakes, if any.

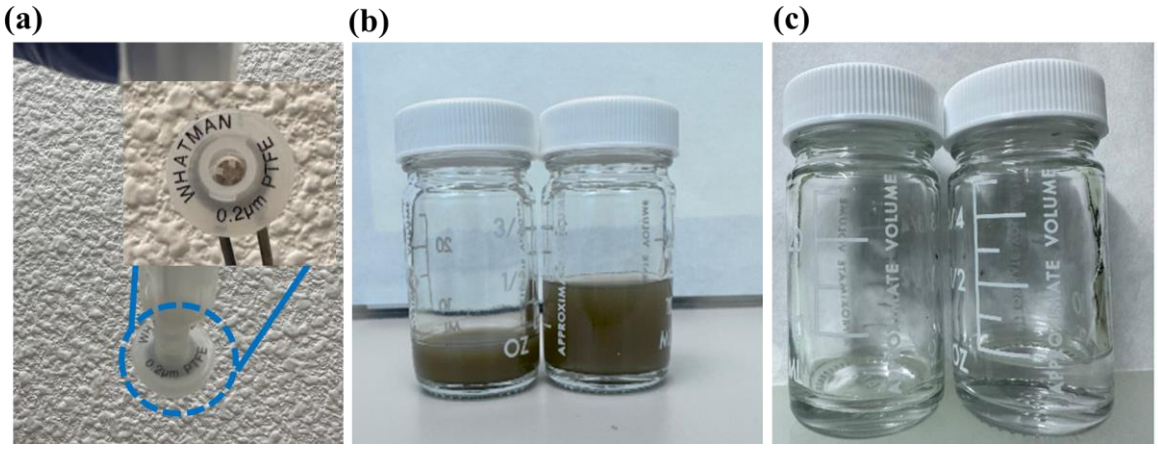

Figure 3.24: (a) The filter was used to separate the macro-flakes from the micro-flakes, (b) InSe-IPA solution after 5 h of sonication, and (c) the same solution after filtration.

4. The DI H_2O is typically regarded as the perfect solvent medium for graphene and 2D in LPE studies [39]; Hence, another LPE trial was made and this time by sonicating 40 mg of InSe in 40 ml DI H_2O for 15 h to compensate for the lack of the centrifugation step. Figure 2.25 depicts the outcome of the process of sonicating the InSe in DI H_2O for 15 hours. As a result, the solution has acquired a greenish hue, similar to the color obtained from the previous solvent.

Figure 3.25: InSe-solvent solution sonicated in DI H_2O for 15 h.

5. As a last trial, we mixed 1 g PVA with 20 ml of InSe-H_2O solution (the solution resulted from the previous experiment N°4) for 1h under a temperature of 75 °C and continuously stirring at 650 rpm the resulted solution presented in Figure 3.26 as we have seen earlier that some studies demonstrate the efficiency of the use of Water/polymer mixture in LPE [79][39], our motivation in the use of the PVA was to make the doping process more efficient and easy that we can coat the LIG electrodes with this mixture as we are doing with the electrolyte.

Figure 3.26: PVA: InSe-H_2O, prepared after 1h at 75°C, under stirring at 650 rpm.

3.3.1.b. Doping and drying process

Our concept was to dope either the Kapton 125 µm thick film before laser irradiation or to dope the LIG after laser application to improve the efficiency of the MSCs. Three doping strategies were proposed in this study, summarized in the scheme represented in Figure 3.27:

- Doping the Kapton with InSe and applying a laser pass to both precursors (Figure 3.27.a).

- Doing pyrolysis of the Kapton with the laser and then doping the LIG with InSe (Figure 3.27.b).

- Doing pyrolysis of the Kapton with the laser; then doping the LIG with InSe and finally applying another laser pass [65][73][76].(Figure 3.27.c).

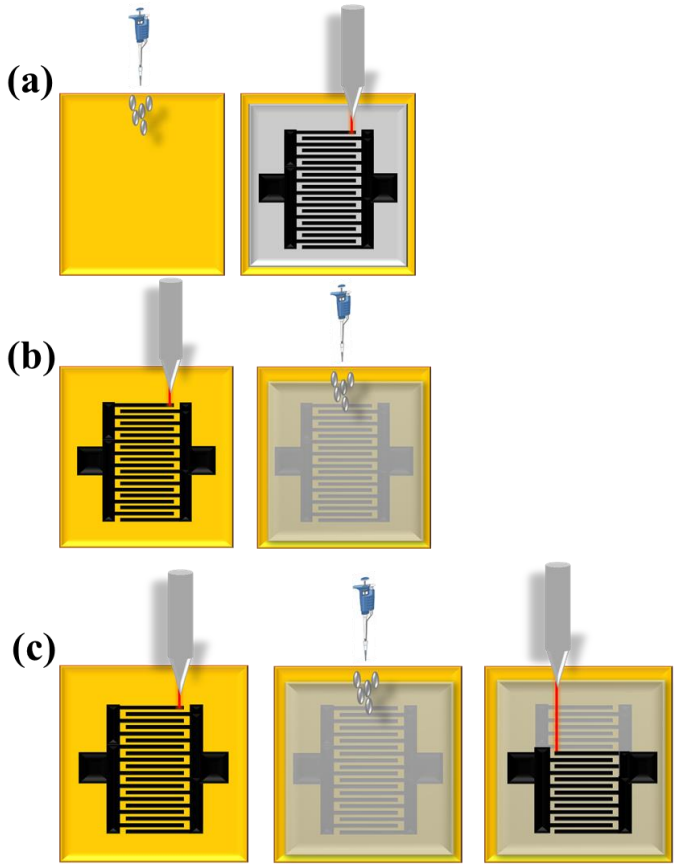

Figure 3.27: The Three depositing methods proposed for this study.

The process of doping the Kapton (1st method, Figure 3.27.a) failed because the Kapton surface is hydrophobic, causing a leak of the dopant away from the substrate when we tried to apply it. Consequently, this approach was not promising to achieve our goal. Moreover, the 3rd method presented in Figure 3.27.c was impossible to achieve with the precision of our laser, especially in the case of an interdigitated design. When we removed the sample after the first pyrolysis step to dope it, dry it, and then we returned it to the laser sample stage for the second pass, we found that the laser shifted a little bit each time as a result, the impossibility to achieve a precise overlapping on the first pass fabricated electrodes

led to shortcut issues. For these reasons, we conducted all the subsequent doping experiments on top of the LIG, following the 2nd method depicted in Figure 3.27.b.

For all the doping and drying trials, we chose one laser parameter to prepare the LIG MSC flexible samples, 2,4 W of power, and 80 mm/s scan speed. Several doping processes were examined: **Drop-casting**: the first depositing test was the drop-casting [65][68][72] (as shown in Figure 3.28.a) of 0,20 ml of the InSe solution using a syringe; the drop cast must be drop by drop to not to lose the dopant material because the size of the pores was small and the adsorption will not be too fast this process made under a hot plate 75°C to dry the LIG surface however this step should be done fast and carefully to protect the LIG from the overheating and damaging its structure. **Spray-coating**: 0,20 ml of dopant [77], using an airbrush as presented in Figure 3.28.b, the process has to be slowly and under low pressure to give the dopant enough time to penetrate effectively inside the electrodes, and the drying method was similar to the drying after drop casting. **Spin-coating**: several spin-coating conditions, 500 rpm/20 s, 1000 rpm/30 s, 1500 rpm/20 s, and 2000 rpm/20 s, we changed the parameters from slow speed and time to fast speed and slow time to get successful doping [73]. However, the process was unsuccessful because we noticed that all the dopant solutions flowed out of the surface sample, and there was no need for the drying step. **Immersing** is an effective way of doping the LIG, as demonstrated by Song et al. [60]. In a well-cleaned glass petri dish, we immersed the flexible LIG MSC in 0,20 ml of InSe solution (check Figure 3.28.c) till we noticed the adsorption of all the solution, then we dried it at room temperature. **Coating**: 0,20 ml of PVA: InSe-H_2O was spread on the interdigitated area of the sample, and then we put it in an active vacuum for 1 h to extract the air and the H_2O from the porous, Figure 3.28.d depicts LIG-MSC sample coated with PVA: InSe-H_2O under an active vacuum.

After these trials, we chose to dope our samples with the drop-casting method because it is easy to control by doping the LIG drop by drop without losing any material; unlike spray and spin coating, the immersing process is good, but it takes a long time in the drying step, for the coating with PVA: InSe-H_2O was the easiest

doping method however, after drying it in the vacuum and applying the electrolyte which contained more PVA we noticed that the electrolyte did not penetrate well after the vacuum compared with our other devices. We suggest that maybe we have used too much polymer which led to a blocking of the pores and resulted in an obstruction of the electrolyte from penetrating the LIG electrodes.

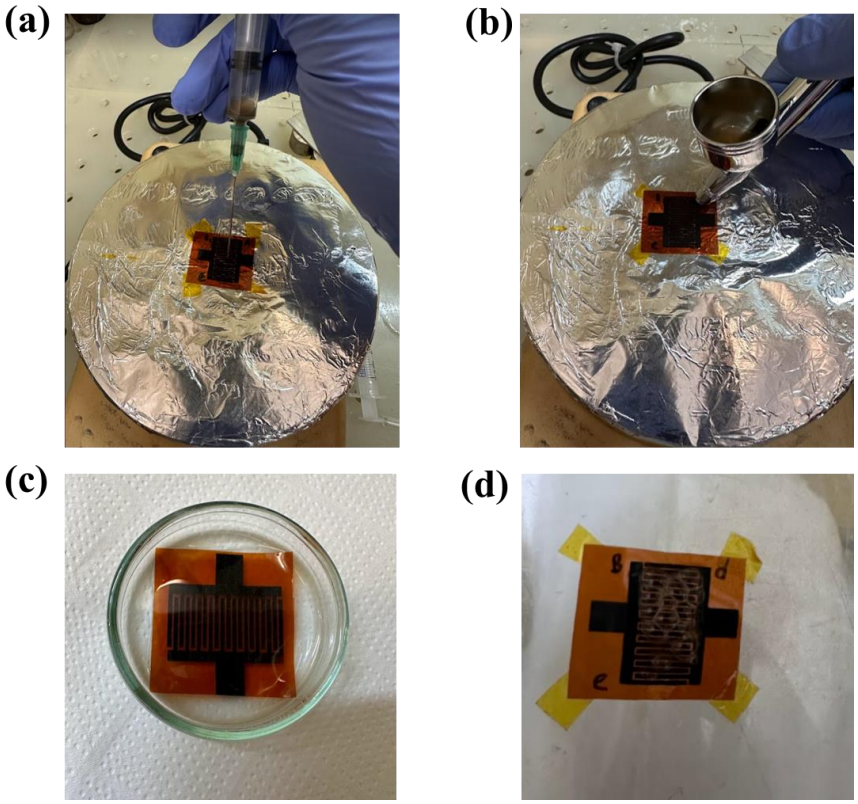

Figure 3.28: The doping process trials of 0,20 ml of InSe-DI H_2O on a 2,4 W-80 mm/s samples (a) drop casting using a syringe and drying on top of a hot plate, (b) spray coating process using an airbrush, (c) an MSC immersed in a glass petri dish, (d) MSC coated with PVA: InSe-H_2O under an active vacuum.

3.3.1.c. Preparation of InSe-LIG electrodes

To select the appropriate laser parameters in this part, 2 ml InSe-H_2O was dropping cast on Kapton 125 μm (15 mm, length) and dried at a 75°C hot plate. Then, we created squares (1 × 1 mm^2) to test the laser conditions and selected the effective parameters that create a continuous and homogeneous LIG structure without losing material or damaging the surface. Several laser powers, one scan

speed, and single and double laser passes were tested, as presented in Figure 3.29. The generation of LIG material started from 2 W power, and for high power up to 3 W, the material started to crack and create gaps and discontinuity on the surface. This was beneficial in our case because 2,0- 2,4- 2,8 W power and 80 mm/s scan speed for single and double laser pass, pristine LIG-MSC performance have been studied; thus, we can compare these materials before and after doping.

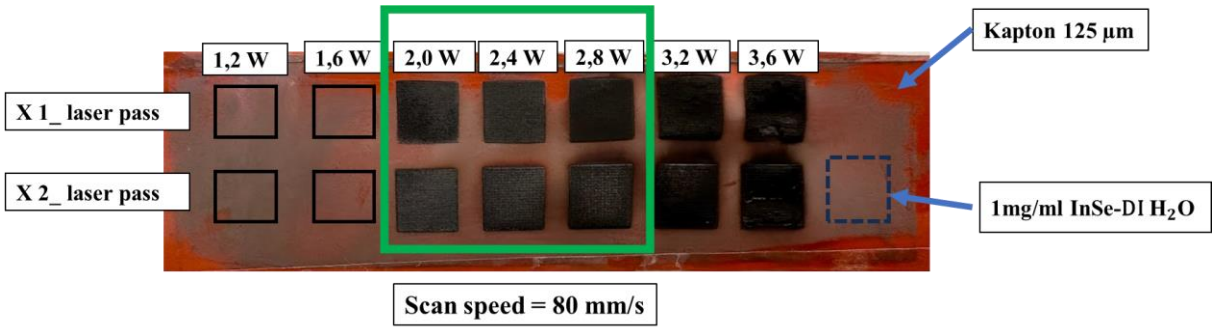

Figure 3.29: The first examination to test the laser parameters on Kapton (125 µm thickness, 15 mm length) doped with 2 ml InSe-H_2O (1 mg/ml) dried at 75 °C hot plate and creating LIG squares (1×1 mm^2) with different laser parameters.

3.3.1.d. MSCs fabrication

For the doped LIG-MSCs preparation, a piece of Kapton 125 µm of thickness film was cleaned well and dried using N_2; we applied single and double laser passes using the six laser parameters marked with a green frame as shown in Figure 3.29 to create the in-plane MSC design (presented in Figure 3.4), then we doped the LIG surface with InSe-DI H_2O (1 mg/ml) solution with an amount of 0,20 ml, and we dried the sample on a hot plate at 75°C, after the drying we continue our protocol in preparation the contacts, applying the electrolyte, vacuum, and encapsulation as we have explained previously in (section 3.2.2.b).

To achieve an additional LIG doping type, as shown in Figure 3.27.c, we created sandwich MSCs. Firstly, we applied the first laser pass to obtain LIG squares of size 1 × 1 cm^2, which resulted in a surface area (~2 cm^2) comparable to the in-plane MSC devices. Next, we doped the LIG with InSe using the drop cast process of 0,1 ml per electrode, and we dried the LIG on a hot plate at 75°C. Then we applied a second laser pass; following with the application of the electrolyte and 1 h of active

vacuum. We have used an ion porous paper as a separator (VWR Qualitative 413 filter paper), finally we made the contacts using silver paint and copper tape, and we encapsulated the device with Kapton tape 60 µm of thickness. The following Figure 3.30 summarizes the preparation of LIG-doped sandwich MSC devices.

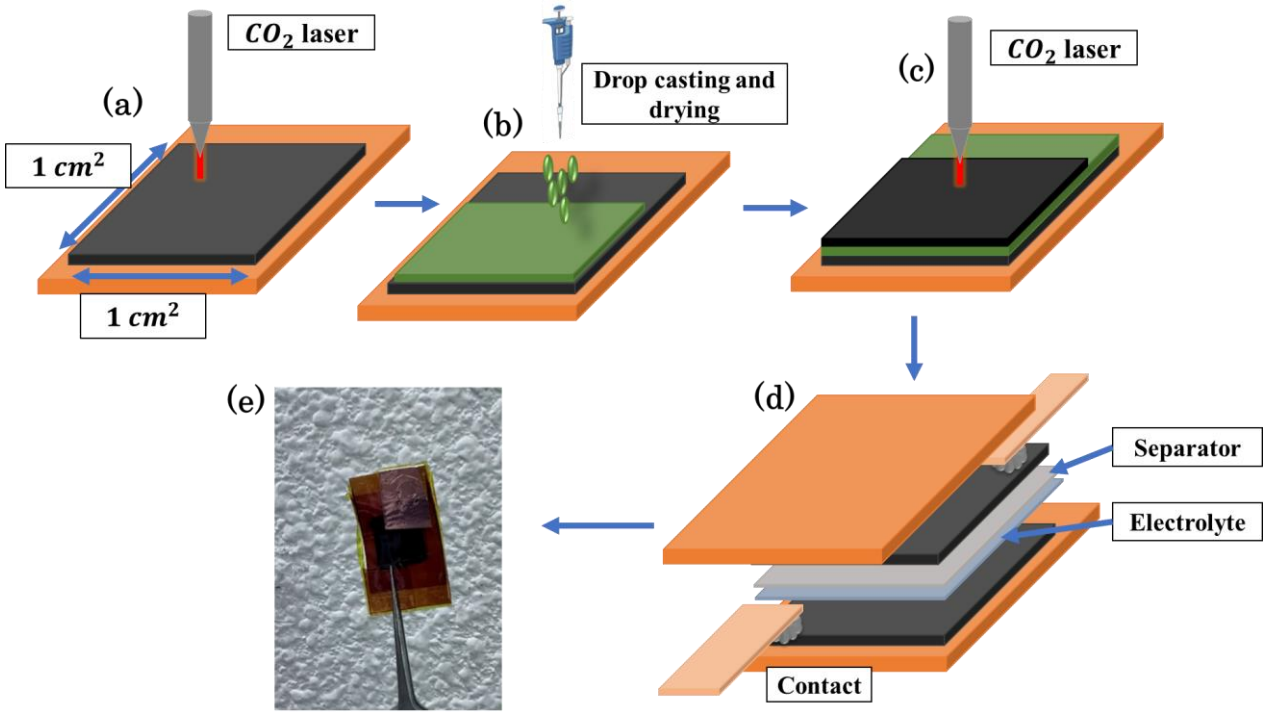

Figure 3.30: Schematic drawing of the doped sandwich LIG-MSC preparation, (a) creating the LIG electrodes by applying the first laser pass, (b) drop casting an amount of 0,1 ml per electrode of the exfoliated InSe solution, and drying them at a hot plate 75ºC, (c) application of the second laser pass over the doped LIG surface, (d) electrolyte coating and vacuum following with preparation of separation and contacts and encapsulating the hall device using Kapton 60 µm.

3.3.2. Materials and Characterization Method

3.3.2.a. LIG-InSe electrodes characterization

Due to time constraints, we could not characterize all our exfoliated material trials. As a result, we only performed one characterization of LPE InSe in IPA using an AFM (Dimension Icon, Bruker, US). We deposited a small amount of the InSe-IPA solution on a silicon dioxide (SiO_2) substrate to measure the size of the InSe particles. The AFM topography imaging measurements were performed using tapping mode, scan rate ranges from 0,5 to 0,7 Hz, 502 of samples line, 5 of proportional gain and an integral from 0,6 to 1. The amplitude setpoint ranged from 210 to 245 mV. Cantilevers with 302 kHz of resonance frequency were used (Si-N-type, AppNano, ACATA-200, US). The data visualization and analysis were done using Gwydion and ImageJ software to measure the particle size distribution.

3.4. Laser-reduced graphene oxide

rGO has gained immense popularity for optical, electronic, sensor, and energy storage applications [123]. Reduction techniques like chemical, photocatalyst, solvothermal/hydrothermal, thermal, and laser reduction have been reported to obtain this material [124]; among these techniques, thermal and laser reduction processes are preferred due to their low cost and fast characteristics. These processes are an effective way to obtain graphene-based materials on a large-scale level. Our study compares laser and thermal reduction of GO. Various thermal reduction methods were applied; these techniques were carried out by researchers at CIEMAT, in the frame of REGRAP-2D project. At the ISOM lab, we employed two different types of lasers to reduce the GO. One of them was an ultraviolet diode laser, with a wavelength of 405 nm, which operates at a peak power of 1000 mW and has a maximum resolution of 327 pixels per inch (ppi). The only controllable

parameter with this laser is the laser exposure time at each point, which could be adjusted from 1 to 100 ms in 1 ms increments. This aspect of the work had been initiated before my involvement in the lab, thus the LPE parameters with the UV laser were predetermined. However, as detailed in the subsequent sections, the second laser type used was the CO_2 laser, consistent with those employed in LIG applications described earlier. I commenced this aspect of the work anew, conducting a thorough review of previous studies on rGO. Based on this review, we conducted several tests to determine the optimal substrate for drop-casting the rGO and the appropriate laser parameters to produce a high yield of LIG. Subsequently, we characterized the resulting LIG and determined the optimal laser parameters to ensure high-quality material. Table 3.1 outlines the general and specific characteristics of the two laser types. The primary motivation for this endeavor was to assess these techniques' efficacy in producing various rGO materials and to evaluate their suitability for use in energy storage applications.

Table 3.1: Characteristics of the two laser types, CO_2, and UV, used to reduce GO in this work [53].

Laser type	Advantages	Disadvantages	Specific features	Common features
CO_2	Low-cost Commercial Simple setup High power	Lower resolution	Continuous wave without the addition of optical choppers. Photothermal mechanism.	The large variety of transformable precursors, including biobased/ Biodegradable. Simultaneous material transformation and device patterning in a single step. Fast processing. High tunability through the modulable parameters and available precursors enables graphene with a wide range of structures and applications.
UV	More dense structures are achievable. Access to the pulse duration and repetition parameters	Higher resolution	Continuous and pulsed mode. Photothermal and photochemical mechanisms	

3.4.1. Materials and preparation methods

3.4.1.a. Liquid-phase exfoliation of GO

For UV LrGO, GO powder was sonicated for 1 h in DI H_2O (5 mg/ml of density) to achieve a uniform dispersion that breaks down the bulk GO into smaller flakes, making it more prepared for the laser reduction step. For CO_2 LrGO, GO powder was sonicated in DI H_2O for 2 h to ensure proper dispersion, followed by centrifugation at 3000 rpm for 20 minutes to remove any large aggregates and to obtain a clear and homogeneous solution that resulted in a GO solution with a

concentration of 2,23 mg/ml, the two LPE resulted in a homogeneous black solution, which is an indication of the effective dispersion of GO. Figure 3.31 presents the two LPE steps we have done to prepare GO for the laser reduction.

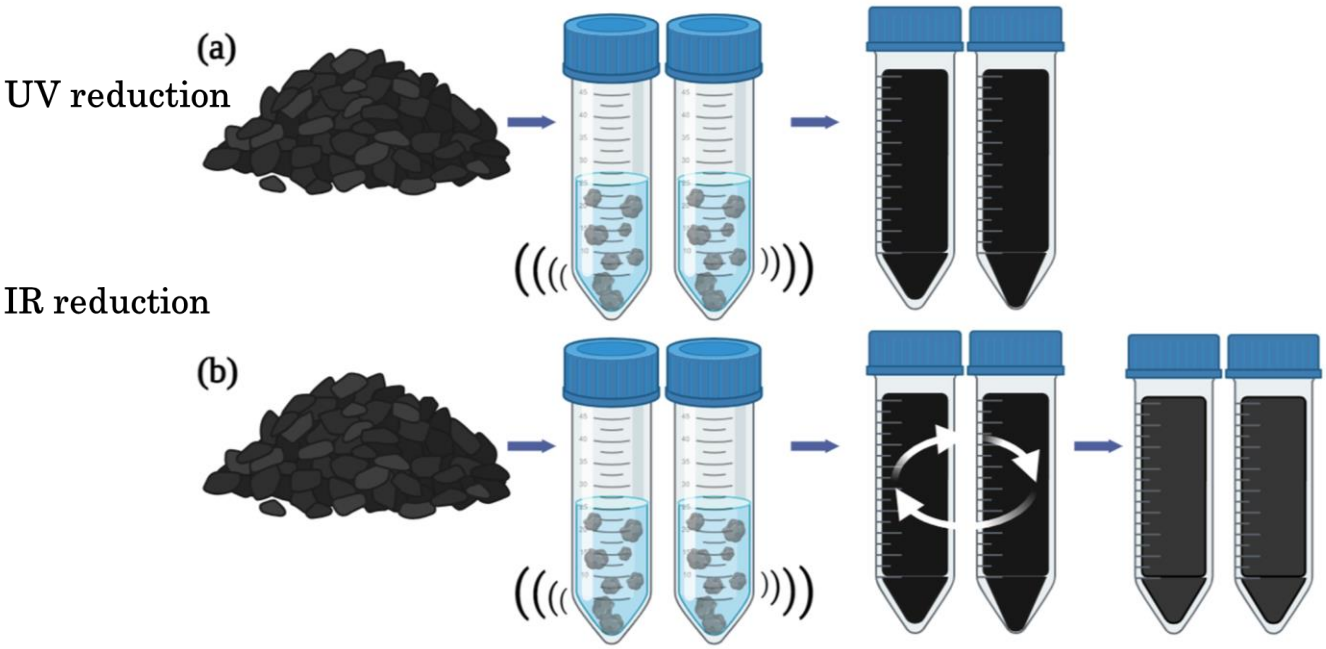

Figure 3.31: The steps used to prepare GO-LPE for the two laser reduction methods: (a) for UV-LrGO, sonicate GO powder in DI-H_2O for 1h, and (b) for CO_2-LrGO, sonicate GO powder in DI-H_2O for 2 h, followed by centrifugation for 20 minutes at 3000 rpm.

3.4.1.b. Laser reduction of GO

Figure 3.32 presents the GO-UV laser reduction steps: 5 mg/ml of GO aqueous solution was deposited on a 25 × 37 mm^2 glass slide in three consecutive drop castings of 2 ml each (Figure 3.32.a); the samples were left to dry on a hot plate at 75°C resulting a black layer demonstrating the evaporation of water and remaining the GO material (Figure 3.32.b). The samples were then subjected to laser irradiation through two consecutive and complementary raster presets for complete areal irradiation (Figure 3.32.c). The first irradiation transformed a circular region in the center of each pixel, while the second irradiation directed the beam to the edges of the pixel. To fabricate the rGO samples, irradiation times of 2 ms, 10 ms, and 50 ms per pixel were used. Figure 3.32.d presents an example of

irradiated samples at 2 ms irradiation time, where we observed a smooth and homogeneous area, indicating the effective reduction of GO. Then, the rGO was peeled off carefully from the substrate to get it as powder, ready for characterization as depicted in Figure 3.32.e, where we noticed a decrease in the amount of LrGO despite we used the same quantity of GO, and this occurred because of the increase of irradiation time which generates in a higher power and leads to the loose of the material during the laser process.

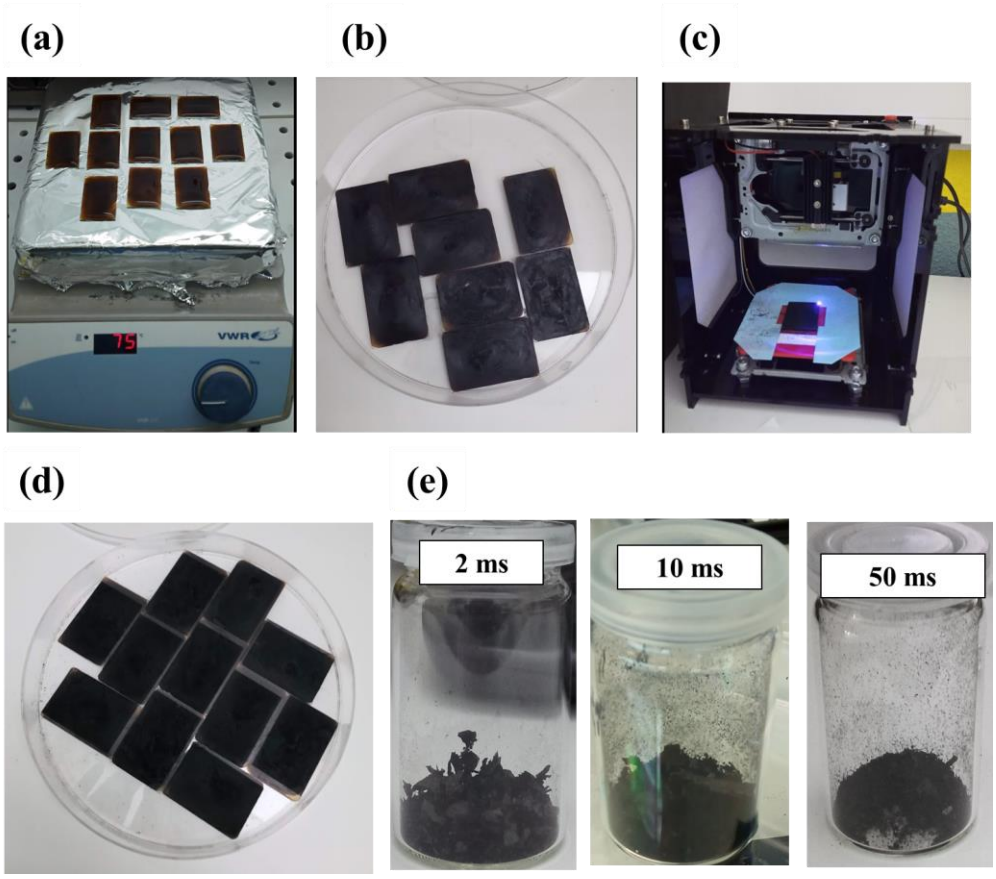

Figure 3.32: GO-UV laser reduction steps. (a) deposition and drying, (b) samples after drying, (c) UV laser during the reduction treatment, (d) 2 ms/pi irradiation time samples after reduction, and (e) LrGO powder of the three laser parameters.

In the case of the IR laser reduction, we first tested which material would be suitable as a substrate for the deposition of the GO and its reduction under different laser parameters. Therefore, we drop cast 1 ml of GO on three substrates squares: 4 cm×4 cm glass, Kapton, and acetate, as shown in Figure 3.33.a and b. After drying them at room temperature (Figure 3.33.c), causing the evaporation of

water and the remaining brownish color of GO, then squares of 1 cm×1 cm were irradiated using the CO_2 laser with different laser parameters power and scan rate presented in Figure 3.33.e (the white squares present the laser powers, and the orange squares present the scan speed), the selection of the substrate depends on its resistance to the laser power. The laser parameters are chosen based on the structural homogeneity and the color transformation, from brownish to black, of LrGO. It is crucial to ensure that no volatile material is produced during the process to avoid losing material, as observed with the glass substrates (Figure 3.33.d. left). Also, the laser power should not be too high to prevent the burning of the substrate, such as in the case of acetate and Kapton at 2,0 W (Figure 3.33.d. center and right, the bottom LIG squares) at faster scan rates. Therefore, we chose acetate as a depositing substance for the GO and lower power and slower scan speed (parameters framed with green square) since it is resistant to all the laser parameters we tested without any damage, and we did not notice any material loos.

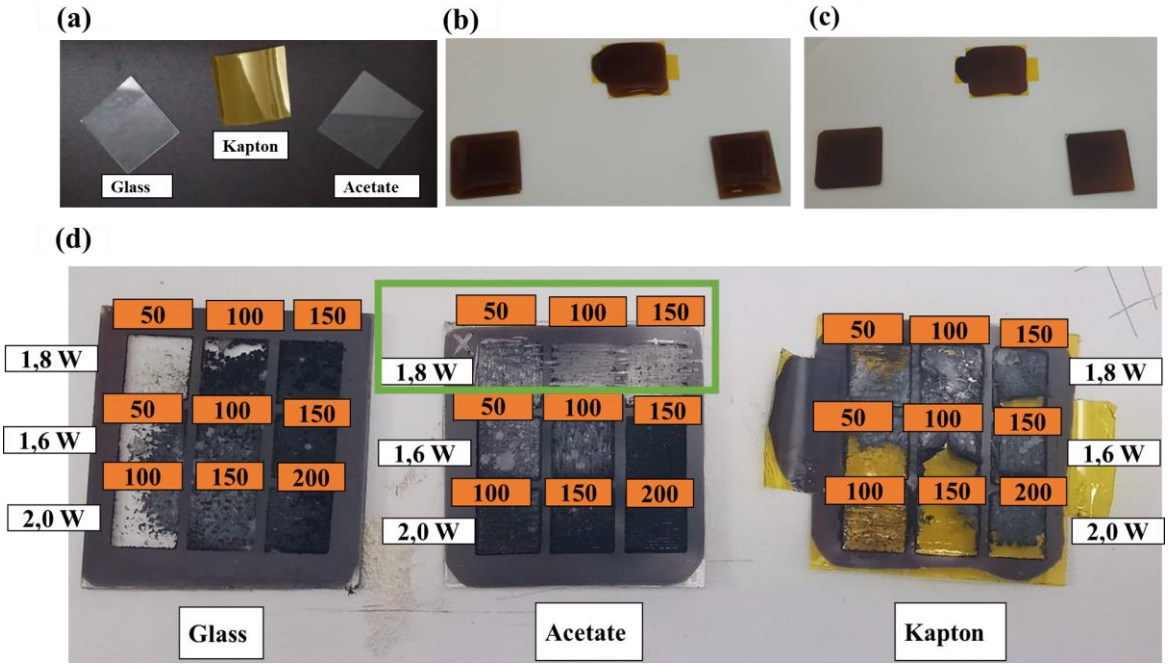

Figure 3.33: (a) The three substrates used for testing the best substrate for rGO, (b) drop casting of 1 ml GO solution, (c) drying the deposited solution at room temperature overnight, (d) testing the different laser parameters the white squares present the laser powers, the orange squares present the scan speed, and the green frame refer to the chosen laser parameters.

After these tests, a layer of 100 ml of GO aqueous solution of concentration 2,23 mg/ml was drop-casted on commercial acetate as presented in Figure 3.34.a, and b, then air-dried for 48 hours. Another 100 ml of the GO solution was drop-cast on the same films to create a second layer of GO, followed by 48 hours of air-drying, resulting in a brownish color of GO with the coffee effect that we can observe less brown color at the top left of the Figure 3.34.b after the water evaporation. Finally, GO samples were reduced using a CO_2 laser at a fixed scan speed of 100 mm/s and three different laser powers of 1,6 W, 1,8 W, and 2,0 W, square by square as shown in Figure 3.34.c, followed by a gentle peeling of the resulting material; a picture of the acetate after peeling the LrGO is depicted in Figure 3.34.d, which shows that the acetate was a resistive substrate to the applied laser even after reducing all the GO large area, the resulting powder illustrated in Figure 3.34.e, thus we can remark the same effect of the material loos while increasing the laser power.

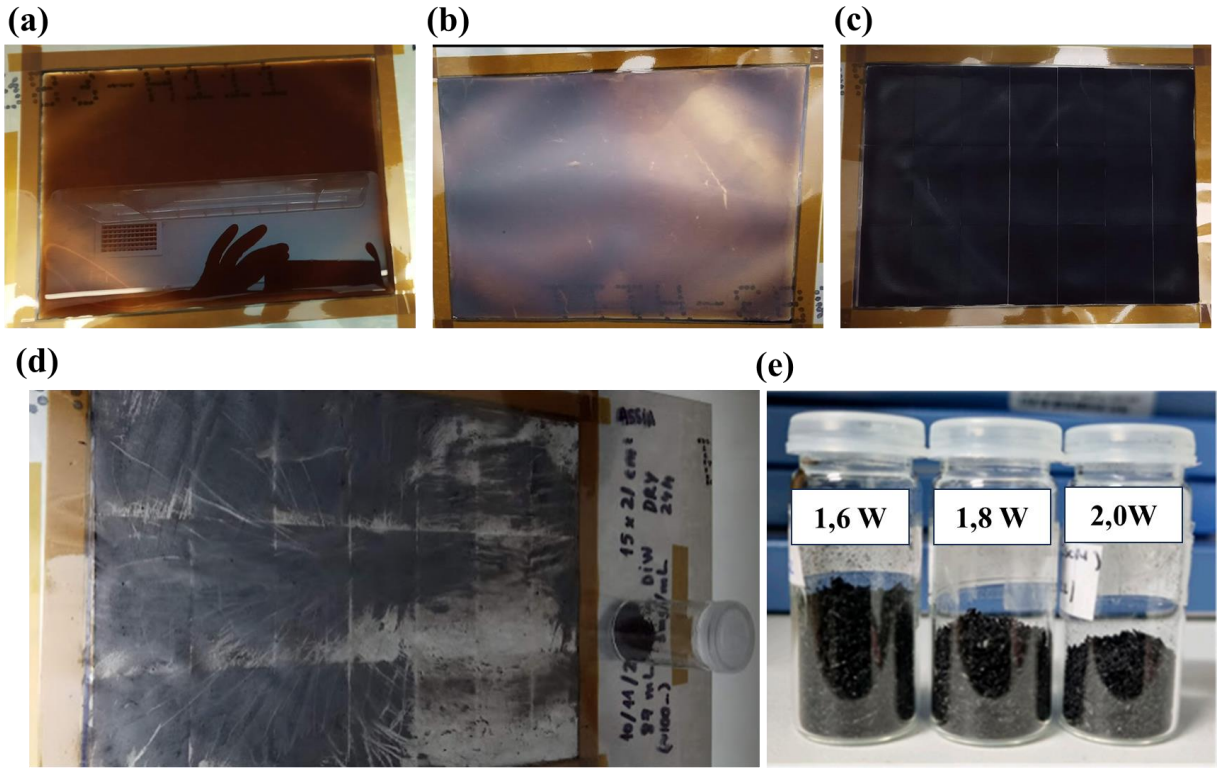

Figure 3.34: IR-LrGO preparation steps. (a) GO solution drop cast on acetate sheet, (b) sample after drying 48 h at room temperature, (c) GO after IR laser reduction of all the area, (d) Acetate sheet after peeling the LrGO demonstrating its resistivity to the high laser power (e) LrGO powder of the three laser powers and 100 mm/s scan speed.

3.4.2. Materials and characterization methods of rGO

- XRD experiments were conducted using Cu Kα radiation (λ = 1,54 Å) and an X'Pert Pro diffractometer (Malvern-PANalytical). The instrument was operated at 45 kV and 40 mA. XRD data was collected in θ-θ configuration within the angular range of $5 < 2\theta < 80$, with a 0,017-step size.

The interlayer spacing between the graphene layers was determined using Bragg equation:

$$n\lambda = 2d \sin\theta \qquad \text{Equation 3.2}$$

Where n is an integer, λ the wavelength of the incident X-rays, d is the lattice spacing and θ the diffraction angle [32].

To estimate the average size of the rGO, the following Scherrer equation is used [32]

$$D = \frac{K\lambda}{\beta cos\theta} \qquad \text{Equation 3.3}$$

Where D is the crystallite size (nm), k is the shape factor, λ is the wavelength of the incident X-rays; θ is the Bragg diffraction angle; and ß is the full width at half maximum.

- The TruSpec CHN elemental analyzer (LECO, Benton Harbor, MI, USA) determined the total carbon and hydrogen content. The sample was heated to a temperature of at least 900 °C in the presence of oxygen gas, which oxidized and/or volatilized mineral and organic compounds to CO_2. The amount of carbon dioxide produced was then measured using an infrared detection method to determine the carbon content.
- The BET method was used with an ASAP 2020 device (Micromeritics, Norcross, GA, US) to determine the specific surface area of graphene samples. Additionally, the pore volume of each sample was evaluated.
- Raman spectra were collected using a Horiba LabRam HR evolution spectrometer (Jobin Yvon Technology, Edison, NJ, US). The sample was placed under a 50× objective of an Olympus BX41 microscope, and a 532 nm

laser beam was focused onto it. The scattered radiation was collected in backscattering geometry, dispersed using 600 grooves/mm holographic grating, and recorded using a CCD detector (256 × 1024 pixels). The acquisition time for a typical spectrum was within 60 seconds, with five accumulations, and a resolution better than 0,48 cm^{-1}/pixel was obtained.

- The morphology of the samples was observed using scanning electron microscopy, using an FEI InspectTM F50 (FEI Company, Columbia, MD, US) SEM with 5 kV accelerating voltage.

4. Results and discussion

4.1. Laser-induced graphene microsupercapacitor

4.1.1. Correlation between the LIG morphology and MSCs functionality

Laser-induced graphene is a material like graphene that can be synthesized quickly, inexpensively, and effectively through laser pyrolysis applied to carbon-based materials. This technique has become a promising application for flexible and wearable electronics, as well as energy storage devices like supercapacitors. As this strategy was developed recently in 2014, its prospects in microelectronics applications are still under investigation. Our study aims to optimize the CO_2 laser parameters on a 60 µm thick Kapton polymer under ambient conditions to create a highly structured LIG morphology and improve the performance of MSCs based on this resulting material. The LIG electrodes produced were characterized via an electronic probe station, SEM, and Raman mapping, demonstrating enhanced LIG quality, complete porosity, homogeneity, and ideal continuity that affect the performance of the MSC devices. Through electrochemical measurements, we demonstrate that MSCs exhibit a high areal capacitance of 22,2 mF/cm^2, with an estimated energy and power density of 3,07 µWh/cm^2 and 0,0462 mW/cm^2, respectively, at a scan rate of 0,05 mA/cm^2 scan rate.

4.1.1.a. Outcomes and Interpretation

After extensive evaluation and characterization of various laser parameters, we took great care in selecting the appropriate conditions to irradiate the Kapton substrate. We aimed to maintain the material's structural integrity while achieving sufficient pyrolysis and good MSC behaviour, we identified optimal power and speed values to transform the Kapton film substrate into a conductive 3D carbon network. In the end, we stopped at four conditions that showed

promising LIG morphology, were homogenous, free from cracks, and showed less resistivity, besides that based on our initial electrochemical measurements these laser conditions showed huge impacts in achieving good electrochemical results when applied in the field of MSCs. The study samples of this section are presented in detail in Table 4.1, along with their laser parameters, (the samples were named as follows S-X-Y where S: samples, X: refers to the laser power in W, and Y: refers to the laser scan speed in mm/s). The fluence was determined through Equation 3.1, and the resistivity was calculated from the electronic resistance measurements.

Table 4.1: Presentation of the four study samples in detail along with their constant laser parameters scan line, laser beam, focal distance, and the variable parameters power, scan speed, and, as a result, the fluence.

Laser Parameters / Samples	Variables				Constants		
	Power (W)	Scan Speed (mm/s)	Fluence (J/cm^2)	Resistivity (Ω.m)	Focal distance (mm)	Line spacing (µm)	Laser beam size (µm)
S-1,8-25	1,8	25	96	1,40	8	75	100
S-2,0-45	2,0	45	59,3	0,46			
S-2,2-65	2,2	65	45,1	0,62			
S-2,4-85	2,4	85	37,6	0,59			

As an initial step, the electrical resistance was measured for the four LIG samples, as described in Figure 4.1. Among these samples, the S-1,8-25 demonstrated a resistance of 351,80 Ω (1,4 Ω.m). Despite this graphitization level was sufficient to ensure the connectivity of the material as we have seen in Figure 3.2; however, it was not enough to produce the highest graphene quality and conductivity. In contrast, the S-2,0-45 set had the lowest resistance and resistivity, around 116,45 Ω and 0,46 Ω.m, respectively. Samples made under other conditions showed resistances in the range of 147-156 Ω, with higher resistivity, suggesting that in

the case of Kapton 60 µm, a power of 2 W is sufficient enough to create a highly conductive graphene-like material, less laser power exhibit the highest resistance meaning that the transformation of the polymer to LIG was not effective and with higher power then 2 W maybe its start to create defect and damage the LIG which reduce the material conductivity.

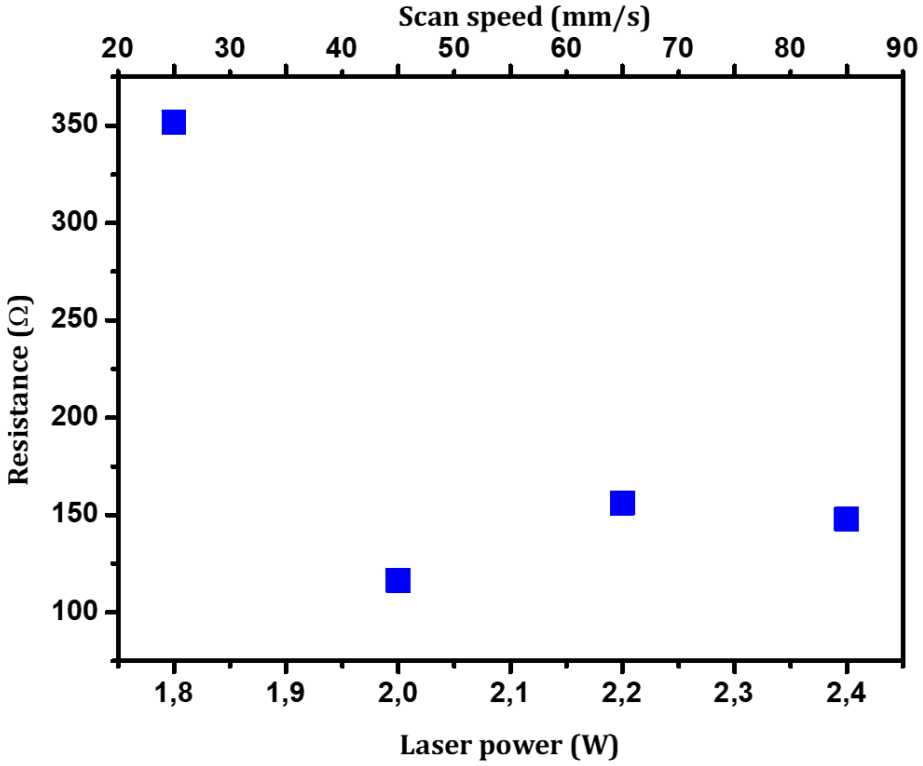

Figure 4.1: The electrical resistance of the four studied samples versus laser power and scan speed, updated from ref [53].

To check the correlation between the conductivity and the material structure, the SEM images of the four LIG samples are presented in Figure 4.2 at four different magnifications (×200, ×1000, ×5000, and ×20.000). The sample S-1,8-25 (Figure 4.2. the 1st raw from the left, images a, e, i, and m), produced with the lowest laser power and the slowest scan speed, the liberation of atoms was both limited and gradual, resulting in a cracked material (check Figure 4.2.a), exhibiting very few and tiny open pores becoming straightforward to observe at higher magnification (Figure 4.2.m). In Figure 4.2. e and i, the direction of laser movement can be observed as the polymer substrate expands and bends when the laser passes,

creating characteristic C-shaped lines when the laser moves from left to right and the reverse for the opposite direction meaning that the laser power was incomplete to rich the level of transforming the Kapton polymer to high LIG quality structure. For higher laser power of 2 W and a faster scan speed of 45 mm/s, the porosity was significantly increased and more uniform in distribution, with a measured pore size of around 2,5 µm, as seen in Figures 4.2.b, f, j, and n (2nd raw images from left). This sample demonstrates the highest pores density, achieving a good compromise between the generated porosity and non-excessive material loss. LIGs fabricated with laser powers higher than 2 W, as shown in Figure 4.2. The 3rd and 4th raw images from the left have bigger pores and gaps due to the largest spot size created from higher laser power, which makes breaking the chemical bands and removing the material during the laser induction process more significant. At the highest magnification (Figure 4.2.c, g, k, and o, the 2nd SEM raw images from the right), S-2,2-65, fabricated with higher laser power and a faster laser scan rate, shows a more heterogeneous porous network with bigger pores in the range of 4 µm. Sample S-2,4-85 has similar structure, but at the lowest magnification (Figure 4.2.d), the heterogeneity is even higher, as the degradation induced by the laser collapsed the pores, thus transitioning its morphology into strings and reducing its effective surface area.

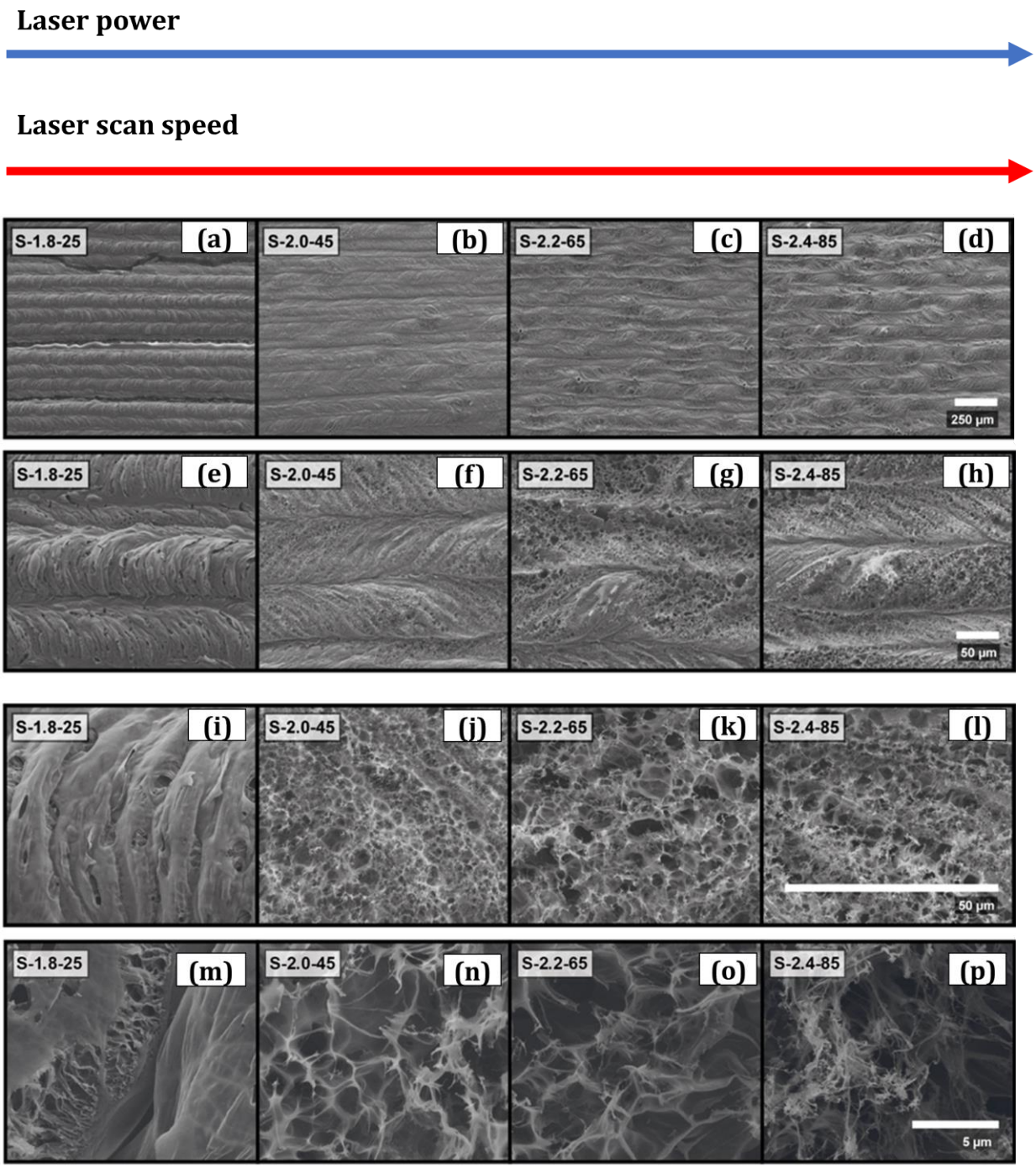

Figure 4.2: SEM images of the four LIG samples in order from the lowest laser power and scan speed to the highest (from left to right) were captured at magnifications of (a-d) ×200-250 µm scale, (e-h) ×1000-50 µm scale, (i-l) ×5000-50 µm scale, and (m-p) ×20.000, scale of 5 µm,[53].

Figure 4.3.a and b display the Raman maps and spectra of the LIG materials fabricated under the four laser conditions. Two sets of maps were generated, each taken along lines perpendicular to the laser scan direction. The purpose was to demonstrate how the quality of the material changes concerning the periodicity of the material transformation. To evaluate the quality of the manufactured LIG, Raman spectra, along with the full width at half maximum (FWHM) of D and G peaks are presented in Figure 4.3.c, and d, respectively. Increasing the material defect concentration results in an increase in the D peak intensity and peak widths and a decrease in the 2D peak intensity. Thus, I_D/I_G increases while I_{2D}/I_G decreases with defects [125], [126].

Figure 4.3.a presents the I_D/I_G ratio for each sample, with darker colors representing more graphitic materials and lighter colors representing more defective areas. In Figure 4.3.b, the I_{2D}/I_G ratio is illustrated, with lighter areas indicating higher graphenic quality and darker areas representing lower-quality regions. These spectra ratios for highly defective sample S-1,8-25 correlating with SEM image which exhibited wrinkle structure and few open sites (Figure 4.2.a), unlike a highly graphitized sample like S-2,0-45 the highly dense porous surface and more homogeneous morphology (Figure 4.2.n), is correlated with I_D/I_G ratios which exhibit less defect presented with darker color while the I_{2D}/I_G is lighter proving a higher graphenic quality. Figure 4.3.c show Raman spectra which are quite similar in all cases, the D and G peaks are narrowed, and the 2D peak is well-defined, except for sample S-1,8-25, which has the lowest laser power. The I_D/I_G and I_{2D}/I_G images for this sample are quite uniform, revealing the homogeneity of the sample transformation but also its poor quality due to the small degree of graphitization. From the images of I_D/I_G and I_{2D}/I_G in Figure 4.3.a and b, regarding the fractions of high-quality S-2,0-45 sample demonstrating the best graphene quality, D and G peak widths of this sample, around 70 cm^{-1}, and the I_{2D}/I_G ratio close to 0,5 corresponds to very high-quality graphene multilayer[127], [128].

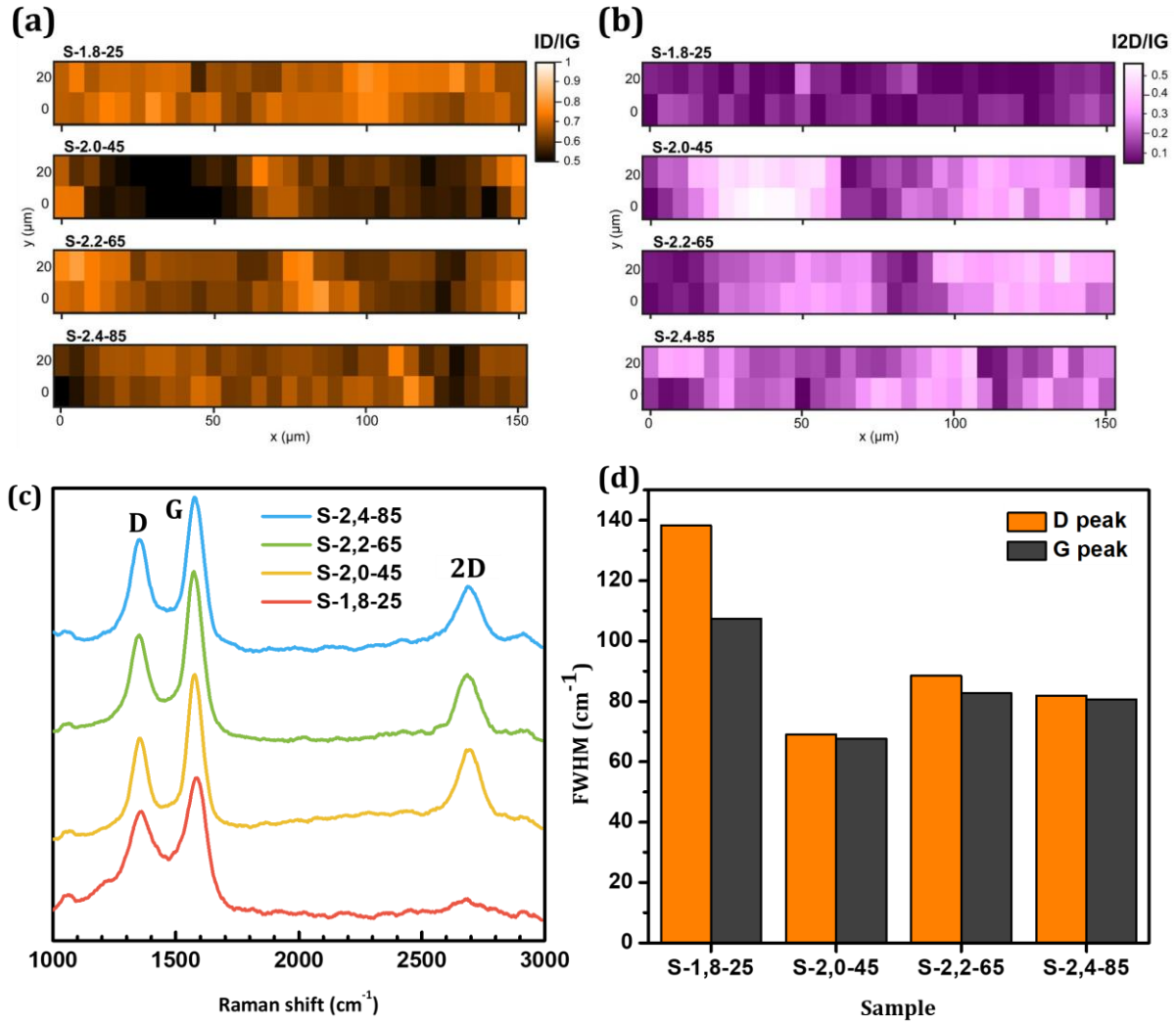

Figure 4.3: Raman mapping and spectroscopy of each LIG sample. The intensity ratios of the Raman peaks I_D/I_G and I_{2D}/I_G were determined (a and b, respectively). (c) the corresponding Raman spectra exhibiting the three graphene main peaks (D, G, and 2D). (d) the FWHM of the D and G peaks for every sample [53].

In the case of the S-2,2-65 and S-2,4-85 samples, the I_D/I_G ratio is lower than in the case of the S-1,8-25 sample, which is due to the higher level of graphitization for the higher power values, despite their higher level of graphitization, there is an excessive removal of material and the collapse of pores that is occurring, as observed before (SEM images, Figure 4.2) The structural degradation of the material translates into the introduction of defects that increase the value of the I_D/I_G ratio and the peaks FWHM.

Microsupercapacitor devices were fabricated based on the different laser parameters listed in Table 4.1 to understand their effect on the electrochemical performance and correlate the results with the outcomes concluded from the microscopy and spectroscopy characterization. We measured CV and GCD at various voltage and current densities, respectively, along with EIS, and presented the results together to compare and find the best device performance. In Fiure 4.4.a and b, CV and GCD graphs at scan rate of 0,02 V/s and a current density of 0,1 mA/cm^2 are presented, respectively, the real capacitance values, were extracted from charge/discharge measurements and calculated for each current density are presented in Figure 4.4.c. A comparison of the EIS measurements is provided in Figure 4.4.d. The best-performing sample overall was S-2,0-45, plotted in red in Figure 4.4.a–d. where its CV curve exhibited more pseudo-rectangular shape and reaching the highest current, the GCD curve as well were the most symmetric curve besides this device has shown the lowest EIS , Although S-1,8-25 outperforms in terms of areal capacitance at very low current densities of 0,05 mA/cm^2 (black curve Figure 4.4.c), the metric drops quickly for faster currents. The CV, GCD, and capacitive current of sample S-2,0-45 under all measured conditions show that the current densities obtained follow an exponential decrease as the CV scan rates increase. This illustrates the power limitation present in LIG MSC devices [129]. The decrease in current can also be attributed to the ion transport in the electrodes. At slower scan speeds, the ions have more time to diffuse through the electrolyte and enter the deeper pores of the electrode. Conversely, at faster scan rates, only the more superficial pores are reached, and this reduces the effective surface area of the supercapacitor [130].

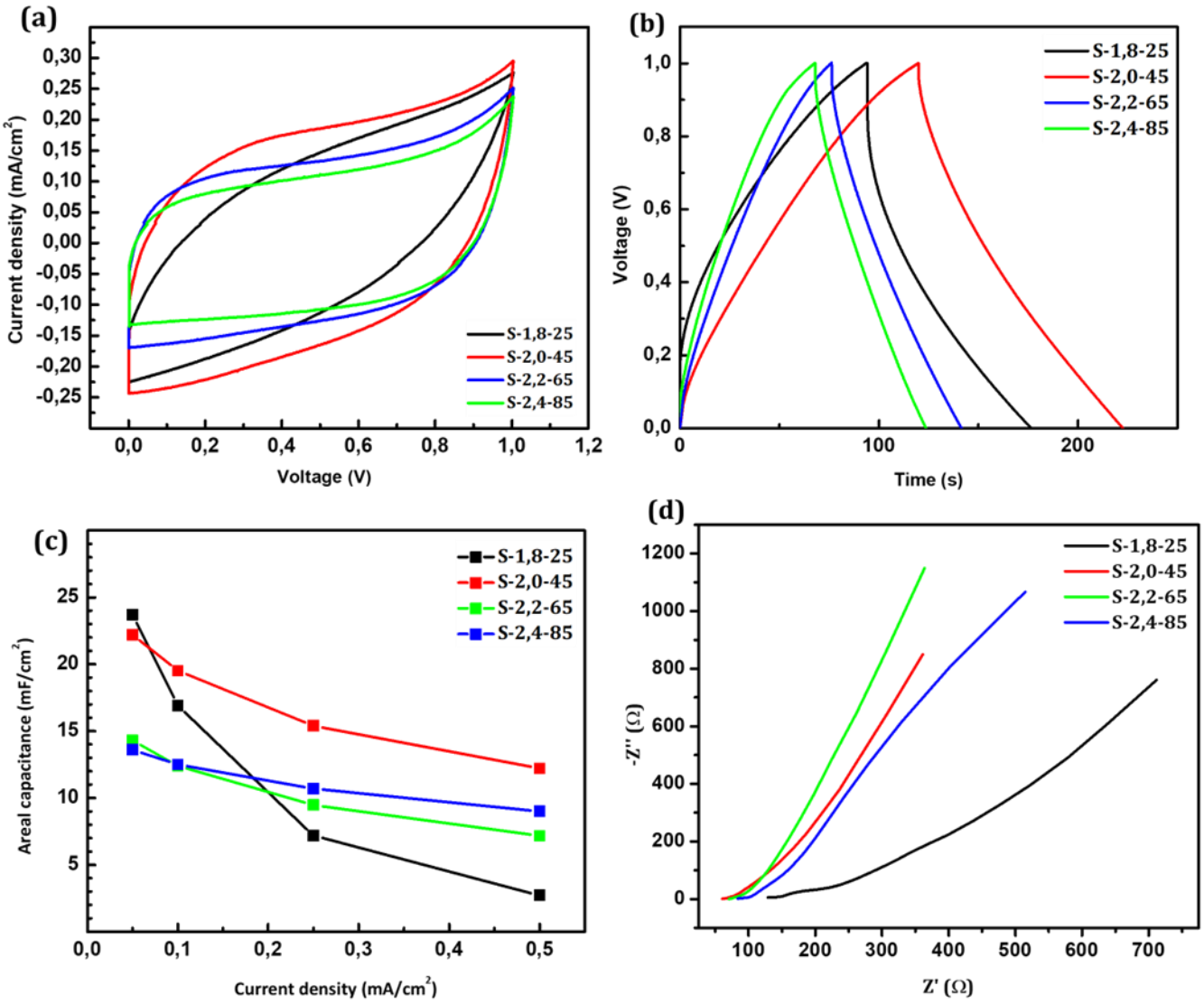

Figure 4.4: The electrochemical measurements of the LIG MSCs were fabricated using the studied laser parameters. (a) and (b) CV and GCD of the four MSCs at 0,02 V/s and 0,1 mA/cm² scan rates respectively, (c) the areal capacitances comparison of the devices versus the current density, and (d) Comparison of the EIS performance [53].

In order to identify the optimal laser settings for producing high-performance LIG MSC, we have analyzed and plotted the areal capacitances of the four laser conditions, as shown in Figure 4.5.a-c. The graph in Figure 4.5.a indicates that laser power is the most critical factor in transforming the material and achieving the highest capacitance. It compares the areal capacitance measured at 0,1 mA/cm² with laser power in watts. Similarly, Figure 4.5.b shows that laser scan speed also

plays a significant role in determining the areal capacitance. This is because laser power influences both the scan speed and the material transformation. While laser fluence is a commonly used parameter in pyrolysis methods, its impact on the interdigitated MSCs' areal capacitance is illustrated in Figure 4.5.c. The lowest capacitance range was found in conditions with the lowest fluence (S-2,4-85 and S-2,2-65), which have a fluence lower than 50 J/cm^2. On the other hand, samples fabricated at 1,8 and 2 W show the highest capacitances with a fluence range from 96 to 59 J/cm^2. The achieved results align with the SEM characterization of each LIG condition. Sample S-2,0-45 is the most uniform and has the best distribution of pores. It has smaller pores (about 2,5 μm) compared to the larger pores of the higher-power samples. S-2,0-45 also has the highest graphenic quality at the center of each raster line, low I_D/I_G ratio, and the highest I_{2D}/I_G ratio among all four samples without too much loss of material. The material of S-2,0-45 is composed of low defective multilayer graphene nanoflakes, forming a continuous porous network. This sample has achieved a maximum capacitance of 22,2 mF/cm^2 at 0,05 mA/cm^2, which is one of the highest values reported in the literature for a LIG MSC. Figure 4.5.d shows the Ragone plot, which compares the areal energy density and areal power density of bare LIG devices fabricated on polyimide substrates without the addition of heteroatoms or pseudocapacitive nanoparticles with similar devices presented in the literature [49][131][73][71][64][72][132]. These metrics are commonly used to benchmark and compare different energy storage devices. The best device achieved in this work exhibited 3,07 μWh/cm^2 and 0,0462 mW/cm^2 at 0,05 mA/cm^2, which is higher than similar devices, even those doped with N or B atoms [131][73]. However, the energy density decreased to 1,18 μWh/cm^2 at 0,5 mA/cm^2, which is 40% less than that obtained at the lowest current density. While this decrease is steeper than those observed in other cited devices, it keeps the device as one of the best. It is worth noting that the LIG MSC used in this study was not doped with any pseudocapacitive element; therefore, these results are even more impressive.

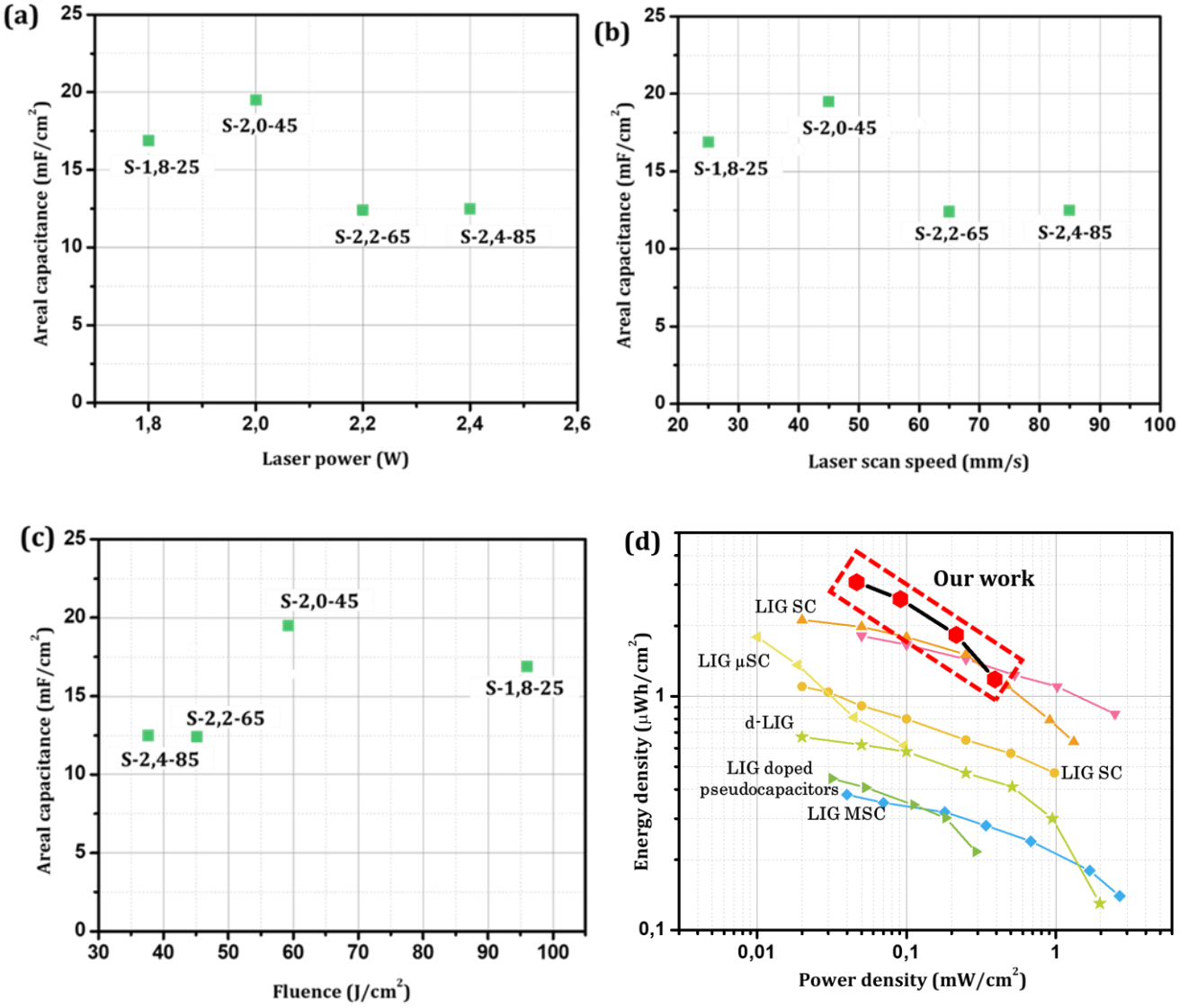

Figure 4.5: The areal capacitance of the measured MSCs at 0,1 mA/cm² was presented as a function of the leading laser parameters of this work: (a) laser power, (b) scan speed, and (c) fluence. (d) Ragone plot of S-2,0-45 sample compared with similar devices have been studied [49](LIG-SC),[64] (LIG-SC),[71](NP-LIG), [72](LIG-µSC), [73](d-LIG), [131](doped LIG), updated from ref [53].

4.1.1.b. Conclusion

We have investigated the relationship between the structural morphology of LIG quality and the electrochemical performance of the MSCs based on these electrodes. For this purpose, we used laser-induced graphene technique in order to fabricate microsupercapacitors from Kapton tape 60 µm thick precursor. The laser

conditions we have used covered the entire possible range of power and scan speed that transformed the material while maintaining its structural continuity for the polymer used. Our findings suggest that laser power is the most significant parameter in LIG formation on thin layers, as it has a more substantial impact than laser fluence or scan speed. We observed that the devices fabricated at a laser power of 2 W (S-2,0-45) had smaller and more uniform pores of around 2,5 μm, as well as the highest material quality, as verified through Raman spectroscopy mapping with an I_{2D}/I_G ratio close to 0,5 and a low I_D/I_G ratio. Both indicators suggest that the LIG material transformed at 2 W was composed of multilayer graphene nanoflakes with high quality and low defects without too much loss of material and reducing the specific surface area compared to other laser conditions that produced less conductive and lower-quality materials even if it is higher but with some reduction in the SSA through the material loss effect as we have seen from SEM analysis. As a result, the electrochemical performance of sample S-2,0-45 was excellent, with an average areal capacitance of 22,2 mF/cm^2 at 0,05 mA/cm^2, which is one of the highest reported in the literature for a LIG MSC without any pseudocapacitive material added. Moreover, this device achieved an energy density of 3,07 μWh/cm^2 and a power density of 0,0462 mW/cm^2 at 0,05 mA/cm^2, which is comparable to other LIG MSCs, even those doped with heteroatoms. In conclusion, this study demonstrates that it is possible to obtain high-quality and high-performing laser-induced graphene by passing the laser on thin layers of polyimide, which is suitable for flexible applications the following Table 4.2 summarizes the characteristic values of the best device in this study.

Table 4.2: The characteristic values of the best device in this study (Areal capacitance, energy, and power density values were calculated at 0,05 mA/cm^2 current density).

Sample	Areal capacitance (mF/cm^2)	Energy density (μWh/cm^2)	Power density (mW/cm^2)
S-1,8-25	16,9	2,75	0,0433
S-2,0-45	22	3,07	0,0462
S-2,2-65	12,4	1,66	0,0463
S-2,4-85	12,5	1,91	0,0463

4.1.2. Optimizing flexible LIG-MSC functionality through laser densification

Flexible MSCs have recently emerged as a primary choice within the electronics landscape. They possess the ability to make electronic devices lighter, more wearable, and easier to carry. Additionally, they can provide instant charging to meet the intermittent or frequent usage demands of delicate electronics. Moreover, they offer many advantages, including exceptional mechanical flexibility, high energy density, rapid charging-discharging rates, long cycle life, economic efficiency, and environmental friendliness. In this study, we introduce a simple, user-friendly, and cost-effective method to improve the production of high-performance flexible microsupercapacitors based on laser-induced graphene. Our approach involves using a single step double-pass treatment of IR continuous CO_2 laser, significantly enhancing the quality of the LIG electrodes. The validity of this approach was confirmed by the porous size expanded by up to 20 %, as demonstrated by the SEM analysis and the wettability test of the LIG surface, which supported these results, as the water contact angle percentage decreased to ~11 % after doubling the laser pass; Raman spectroscopy also showed an increase in LIG quality after the second laser pass. These improvements have positively impacted the performance of MSC devices, particularly in the enhancement of the areal capacitance from 2,99 to 7 mF/cm^2 at 0,1 mA/cm^2. Furthermore, the EIS was reduced to 155,07 % and the device continued to demonstrate high efficiency even after 10.000 cycles, with a capacitance retention rate of 79 %. Additionally, it maintained its high performance under various mechanical and folding tests at different angles.

4.1.2.a. Outcomes and Interpretation

Before presenting the results, we will showcase the study samples selected for the enhancement of flexible LIG-MSCs through the dual laser pass. This section aims to provide a comprehensive overview of the samples and their characteristics. It is imperative to note that the dual CO_2 laser pass technique has shown promise in enhancing the productivity of LIG-MSCs. Therefore, our focus is on presenting the study samples to shed light on the potential of this technique. Furthermore, it is essential to highlight that these samples have been selected on the basis of rigorous electrochemical testing and evaluation to ensure their suitability for the intended purpose. Table 4.3 below defines the samples with their corresponding laser parameters. The samples were named as follows s-X or d-X where s: single laser pass and d: double laser pass, X presents the laser power (2 or 2,8 W), and the four samples were fabricated at the same laser scan speed of 80 mm/s.

Table 4.3: Presentation of the laser parameters used in this study.

Sample	Power (W)	Number of passes	Scan speed (mm/s)	Environment Conditions
s-2	2	1	80	Ambient Conditions
s-2,8	2,8			
d-2	2	2		
d-2,8	2,8			

The laser application generates a high localized temperature that breaks C—O, C=O, or C—N bonds from the initial Kapton polymer resulting in liberation of oxygen and nitrogen atoms as gases, these liberations create porous structures and open sites on LIG surface; its density, distribution and size depend to the laser parameters and in this case to the power, scan speed, and laser number pass. Figure 4.6. depicts the LIG micromorphology of the two different laser powers for single and double laser passes; for lower laser power of 2 W and higher 2,8 W, include four SEM images. In Figure 4.6.a the laser power of 2 W was relatively weak and insufficient to effectively convert Kapton 125 µm to 3D porous graphene,

microscopic pores with an average size of 0,81 μm, ripples, and wrinkles were observed, and the material exhibited a heterogeneous morphology.

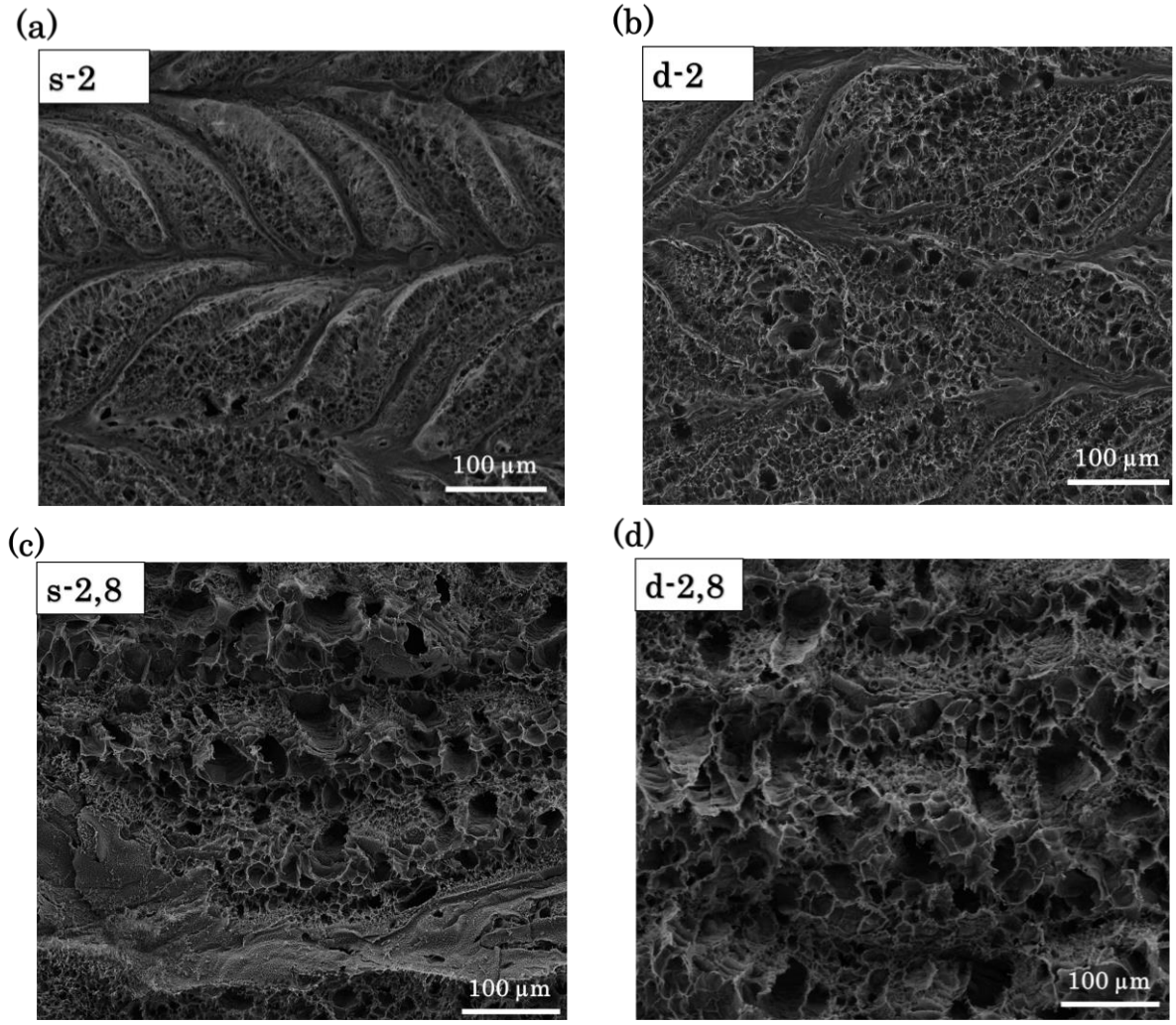

Figure 4.6: Characterization of single and double laser pass LIG samples, using SEM at ×1.000 magnification.

However, in Figure 4.6.b, the number of pores increased with passing a second laser treatment creating new open sites in the waves and wrinkles region, hence the percentage of the wave morphology decreased, and the size of the pores increased by 26,67 % compared to the first laser treatment which resulted from the expansion of the initial pores size. In Figure 4.6 c, a higher laser power of 2,8 W was used, resulting in more gas release through wider open pores [133]. The pores observed were 4,63 μm in average size, and a smooth area free from pores observed in some regions; however, when the second pass was made, a considerably

fully porous surface was created and the LIG structure looks denser with an average diameter of up to 7,22 μm (check Figure 4.6.d), this image shows a more homogeneous and consistent form of 3D foam graphene.

Upon subjecting the material to a second laser pass, the LIG's porosity increases, resulting in an elevated level of permeability. Table 4.4 presents the water contact angles of the LIG after single and double laser treatment, where the hydrophobicity percentage of the LIG decreases by 7% and 11% when double-pass laser powers of 2 W and 2,8 W are employed, respectively. These outcomes align with the prior SEM analysis findings of larger open sites in the LIG structure that led to effective adsorption of water.

Table 4.4: Water contact angle measurements after the wettability test of the LIG surfaces.

Samples	Water contact angle (°)
s-2	81,92
d-2	75,9
s-2,8	60,60
d-2,8	53,91

The second laser pass, mainly when using higher powers, causes the exfoliation of LIG as we have seen previously by opening and expanding the LIG pores after its conversion for Kapton through the initial laser pass. This process results in material loss [134] and then decreased SSA [133]. For 2 W samples, the SSA was reduced to 3,17 % but for higher power 2,8 W, the decrease was up to 23,64 % from the single to the double pass; therefore, for this effect we recommend using low laser power so that there is a balance between improving the LIG quality and not losing material, and thus preserving the SSA. However, this process had another significant impact on the width of the LIG surface material and then on the width of the finger electrodes in the MSC working area [133] The second laser passes resulted in broader and thicker finger electrodes, which in turn reduced the gap distance in the MSC devices. This reduction in gap distance and surface

permeability improvement have proved to be a massive advantage for our application in in-plane MSCs, as it promotes the seamless transfer of electrolyte ions between the negative and positive electrode fingers and offers an effective adsorption and penetration of the applied electrolyte. This, in turn, will significantly enhance the overall efficiency of the MSC system. Figure 4.7 presents the SSA measurements along with the miniaturization of the gap distance in the MSC device after the first and second laser processes.

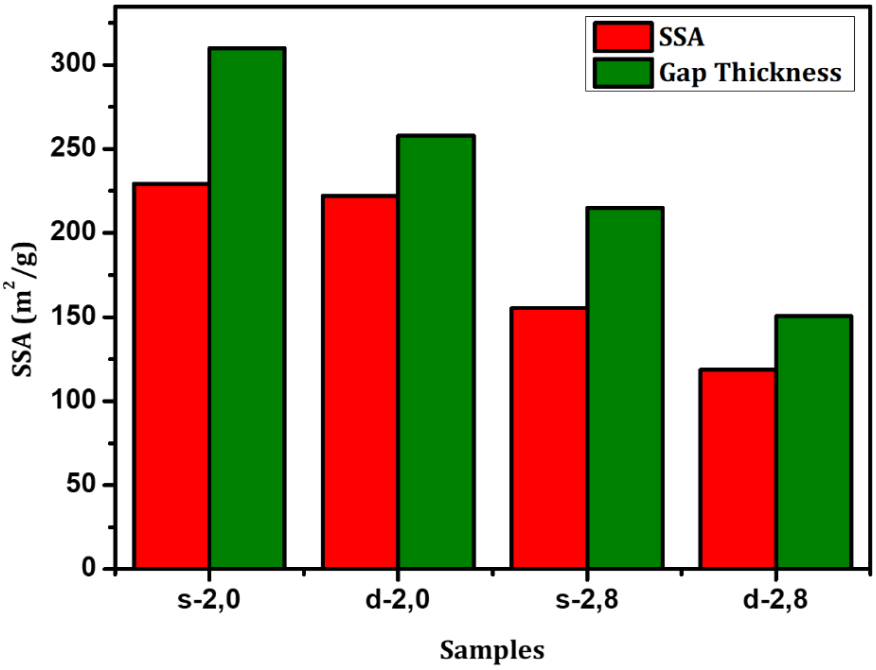

Figure 4.7: Specific surface area calculated from the BET method of the LIG powder and the gap distance decreasing between two MSC LIG fingers when the laser pass number doubled.

Raman spectroscopy was used to understand the correlation between the number of laser passes and the LIG chemical structure. The three dominant graphene peaks D, G, and 2D appear in all spectra [125][135]. The intense and narrow peaks demonstrate the conversion level of Kapton to LIG by CO_2 laser irradiation.

The D peaks are centered at ~1340 cm^{-1} signifies the presence of structural defects resulting from the disruption of positional symmetry within the carbon sp^2 network. G peaks~ 1570 cm^{-1} corresponding to the vibrations in the plane of sp^2-

bonded carbon atoms bonded to sp^2 and the degree of graphitization and 2D peaks~2670 cm^{-1} depict the generation of multilayer 3D graphene configurations [136]; These results are comparable to the Raman shifts of the graphene peaks reported in the literature [49] However, it differs in its intensity and sharpness from laser power to another and from primary to secondary laser pass, as illustrated in Figure 4.8.a. The intensity of the D peaks after the second laser pass decreased; this confirms that this approach improves the LIG quality by reducing the material defects and increasing the intensities of the G and 2D peak intensities. To confirm this, we have calculated the I_D/I_G ratios which decreased from ~0,80 to ~0,68 for samples of s-2 and d-2, as for s-2,8 and d-2,8 from ~0,42 to ~0,29 expresses a lower degree of disorder in the produced LIG, another vital factor to indicate the number of graphene layers is the I_{2D}/I_G ratio, is ranged from ~0,40 to ~0,35 for samples d-2 and d-2,8, respectively, signals that the formed LIG is a multilayer of single layer graphene sheets having around 4 to 5 layers for the electrically conductive layer formed on the Kapton surface [136].

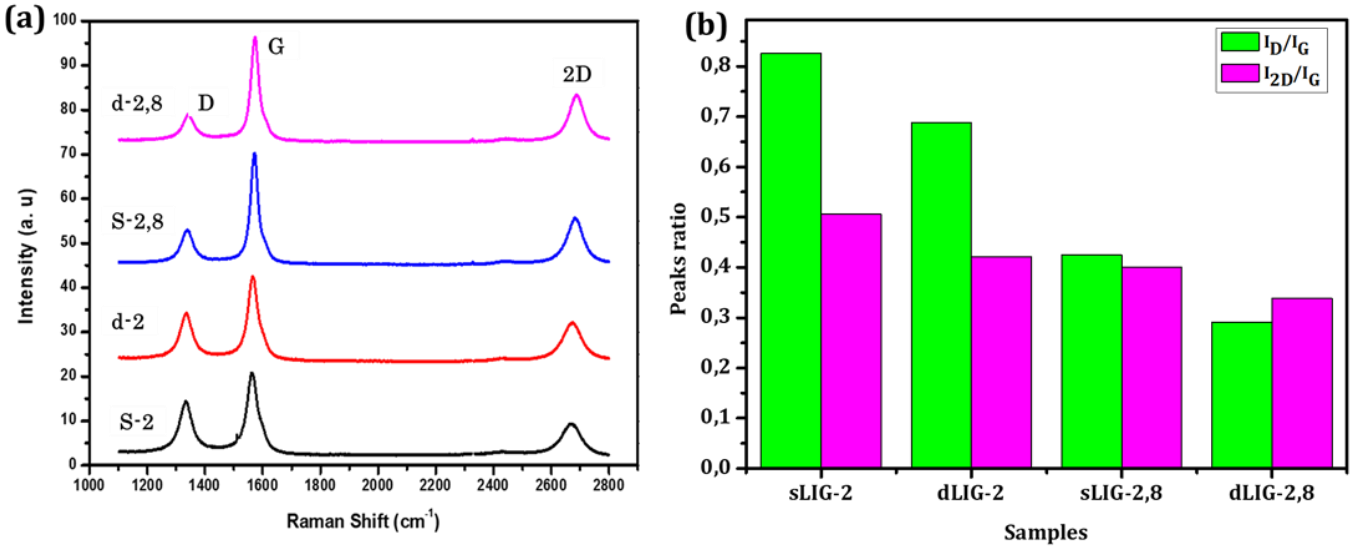

Figure 4.8: Raman analysis. (a) Raman spectroscopy of the study samples, indicating the three dominant graphene peaks D, G, and 2D, (b) I_D/I_G and I_{2D}/I_G peaks ratio

Flexible LIG-MSCs based on the parameters listed in Table 4.1, under ambient conditions using 1M H_2SO_4: PVA were characterized electrochemically in order to

investigate the impact of this technique on their performance. In Figure 4.9 black curves corresponding to the single laser pass and the red curves for the second laser pass. The CV curves depicted in Figure 4.9.a and c exhibit symmetric quasi-rectangular shapes across both MSC samples at 0,01 V/s for single and double lasers, a characteristic feature of EDLCs and a typical behavior of supercapacitor devices.

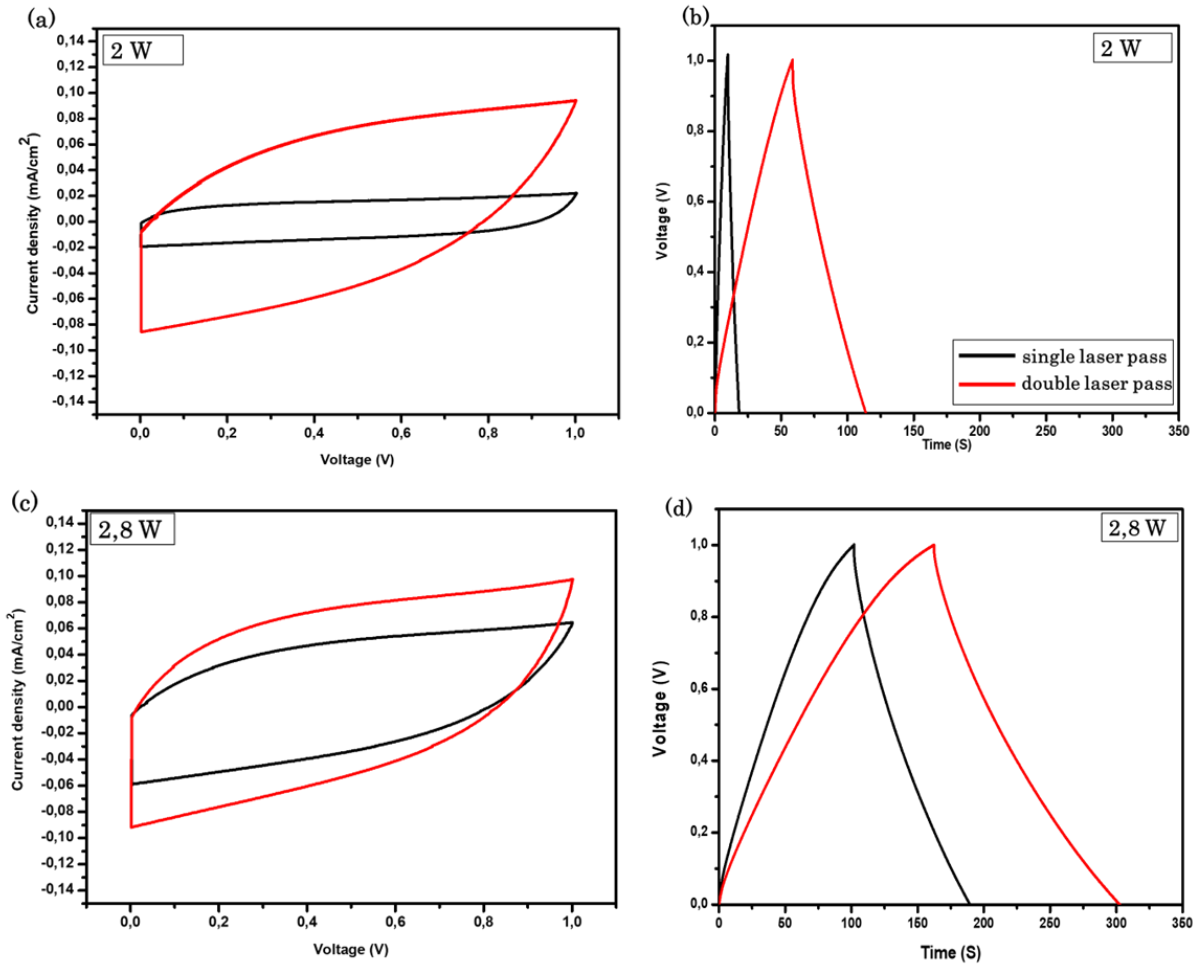

Figure 4.9: CV and GCD comparison between the single and double laser treatments at 0,01 V/s scan rate and 0,1 mA/cm² current density.

This consistency signifies excellent electrochemical stability where the double pass in each case improves the device functionality, the areal capacitance increases up to 130,20 % from sample s-2 to sample d-2 and in the same way for samples s-2,8, d-2,8 increases to up 134,11 %. A parallel observation can be drawn from the GCD

curves at 0,1 mA/cm² shown in Figure 4.9.b and d, where the nearly ideal symmetric triangular shapes, coupled with a very low voltage drop, further indicate a commendable capacitive behavior. Notable enhancements in electrochemical performance become evident after the second laser pass, as illustrated with the red curves; both CV and GCD results show a successful increase which has an important impact on the EIS, which decreases almost 58,77% and 155,07% for samples of 2 W and 2,8 W, respectively after the second laser pass, as presented in the following Figure 4.10.

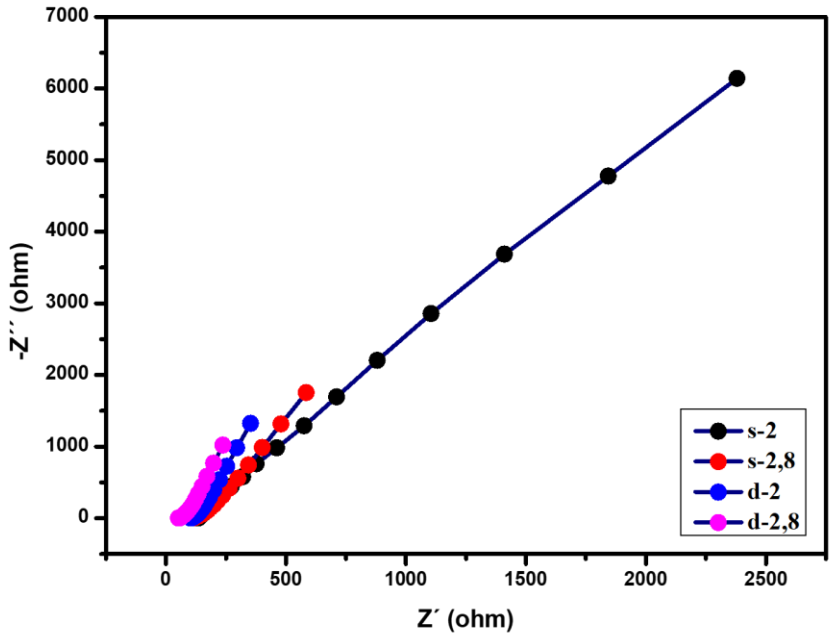

Figure 4.10: Comparative EIS analysis of four samples overlapping to assess its reduction following the second laser pass.

This emphasizes the substantial impact of improving the LIG quality on the enhancement of the performance of the MSCs device. Here, the second laser pass, as revealed by SEM, and Raman analyses, significantly alters the LIG morphology, whereas another laser pass improves structure, minimizing defects, opening more pores, and expanding the older pores resulting from the first laser pass, resulting in an effective penetration of the electrolyte ions. Furthermore, the second pass widens the fingers of the in-plane MSC, reducing the gap between them, and

facilitating rapid and smooth ion movement across the working area, and as a result, the interplay ultimately contributes to the reduction of device resistance.

The d-2,8 sample shows a high increase in areal capacitance of 7 mF/cm² after the second laser pass while the d-2 sample increases its areal capacitance ~5,87 mF/cm² at 0,1 mA/cm² current density of 0,1 mA/cm² and highly optimizes the energy and power densities presented with the continuous lines in Figure 4.11.b. These flexible LIG MSCs demonstrate the powerful impact of this simple and single step of doubling the laser pass in improving the resulting LIG quality and then upgrading the electrochemical productivity as illustrated in Figure 4.11.

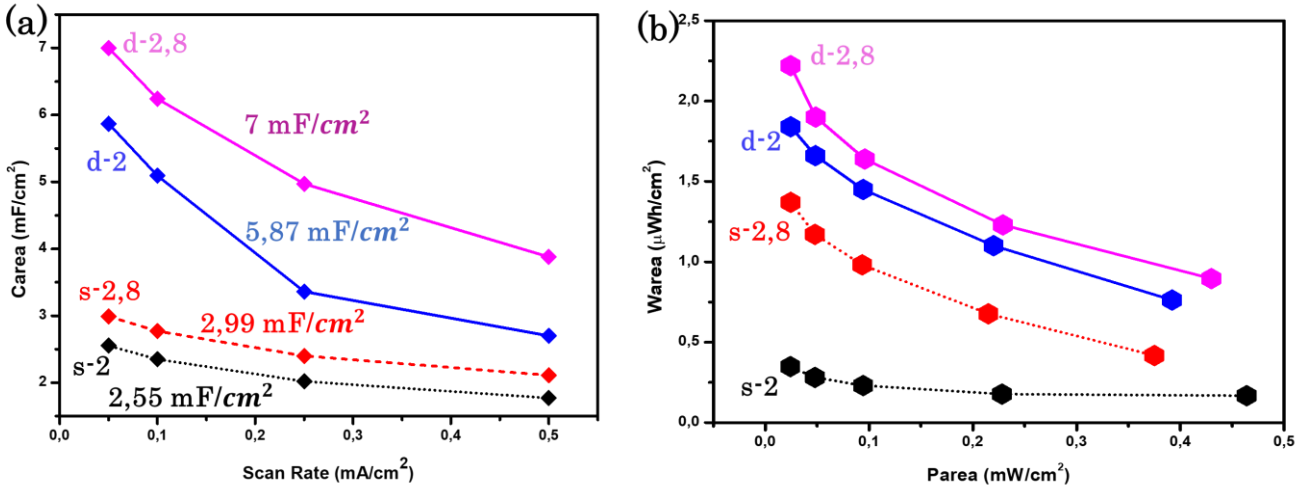

Figure 4.11: Comparative analysis of single and double laser pass devices' performance: (a) areal capacitance vs. scan rates, (b) areal energy-power density (Ragone Plot) at 0,1 mA/cm².

To address the requirement for increased voltage and current in practical applications, three d-2,8 devices were set up in both series and in parallel configuration to register the triple capacitance (highlighted in the green voltammogram in parallel) and the tripling of the potential window (illustrated by the violet voltammogram for series arrangement), presented in Figure 4.12. LIG-MSCs connected in series, resulting in a linear increase in operating voltage from 0 V to 3 V, and the CV curve results in a standard rectangular shape at a scan rate of 0,05 V/s. Parallel devices could evidently obtain a higher current density and thus three times higher capacitance. These outcomes apparently demonstrated

that the MSC prepared by this approach of densifying the laser pass had great potential in MSCs and the microelectronics sector.

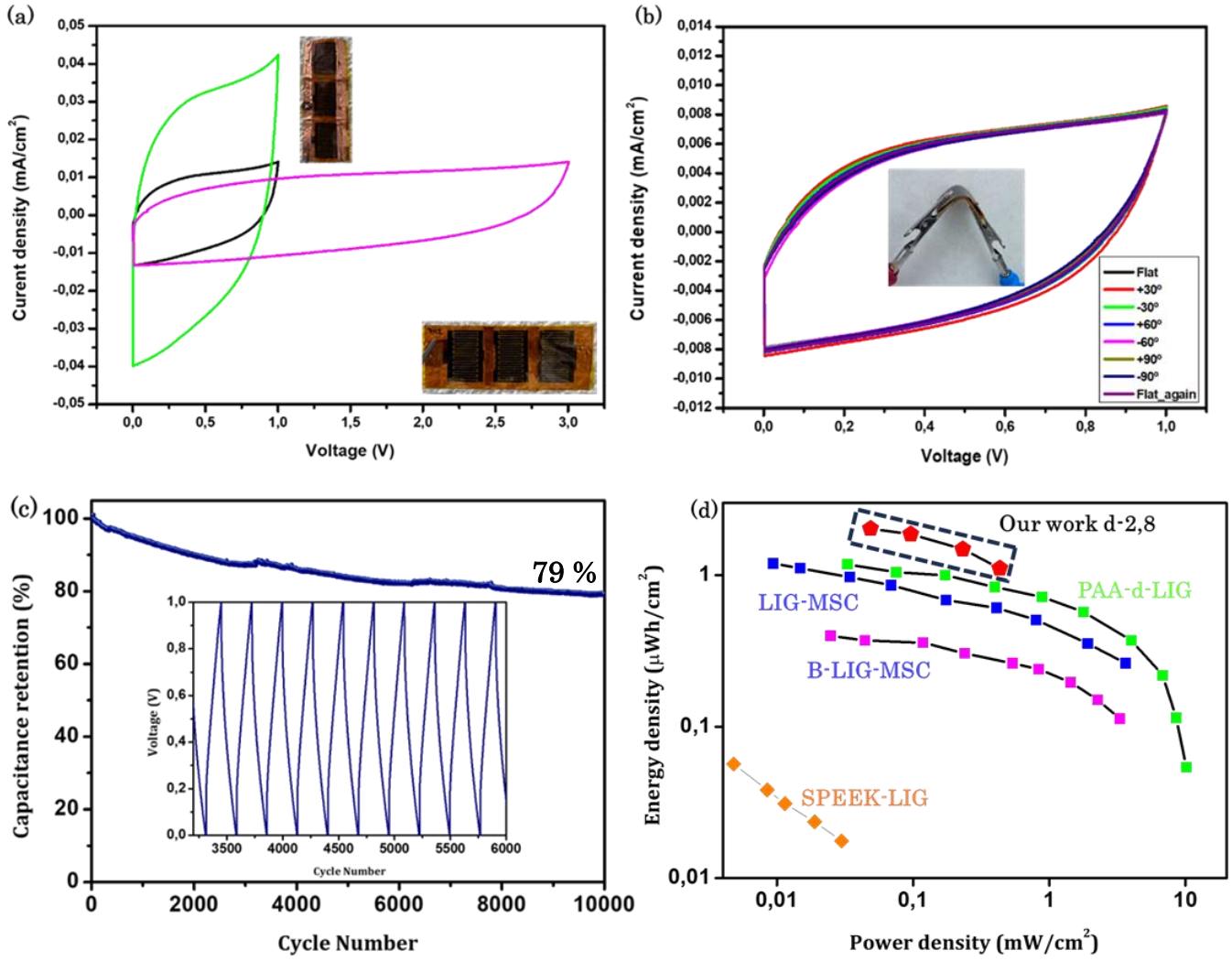

Figure 4.12: (a) CV of d-2,8 device placed in series (Blue) and parallel (Green) comparing with a single device (Red) at 0,05 V/s, (b) CV of d-2,8 under different bending angles at 0,05 V/s, (c) cyclability measurements of 10.000 GCD cycle at 0,5 mA/cm², (d) Ragone plot comparison with previous literature LIG-MSC [49], PAA-d-LIG [137], B-LIG-MSC [67], SPEEK-LIG [138].

Given that flexible devices will undergo rigorous mechanical stress in practical applications such as wearable health technology, foldable smartphones, and smart robots, Figure 4.12.b presents the examination of the mechanical stability of the flexible MSC, the d-2,8 device was tested at different bending angles and the results showed that the device maintained its performance even when bent under

various angles, without any significant decrease. Finally, even after 10.000 cycles, the device was able to retain approximately 79% of its initial capacitance (Figure 4. 12. c) confirming ideal stability throughout the life cycle. Additionally, sample d-2,8 that has a pristine LIG electrode demonstrates high efficiency compared to MSC-based LIG doped with nitrogen and conductive coating [60] that achieves 790 $\mu F/cm^2$ at 75 $\mu A/cm^2$ and NiO and Co_3O_4 with 2,4 mF/cm^2 [61], comparing our results in terms of energy and power density Ragone plot presented in Figure 4.12.d demonstrate that the d-2,8 sample with 2,03 $\mu Wh/cm^2$ of energy density and 0,00487 mW/cm^2 at 0,5 mA/cm^2 which is higher than LIG-MSC coated with polyamic acid (PAA) [137], LIG based MSC [49], boron-doped LIG MSC [67], and SPEEK LIG MSC [138].

4.1.2.b. Conclusion

In summary, through this study we present a cost-effective and efficient technique to enhance LIG quality, which can, in turn, improve the performance of MSC devices. The proposed technique involves doubling the laser treatment, leading to significant improvements in LIG morphology and quality, expanding pore sizes, and opening the electrode width. These improvements result in a decrease in the spacing distance between the positive and negative electrodes, ultimately reducing the EIS from 214 to 83,90 Ω. Furthermore, the technique increases the capacitance, energy, and power densities from 2,99 to 7 mF/cm^2, 0,69 to 2,03 $\mu Wh/cm^2$, and 0,00477 to 0,00487 mW/cm^2, respectively, at 0,1 mA/cm^2. The bending test and the cyclability measurements revealed a high retention of capacitance of 79% from the initial capacitance after 10.000 cycles, indicating that the productivity of the device remains high. The results of this study demonstrate the potential of the proposed technique as a cost-effective and efficient method for improving the performance of LIG-based MSCs. The following Table 4.5 presents a summary of the enhanced results of sample corresponding to 2,8 W laser power when single and double laser pass was applied.

Table 4.5: Results enhancement of the flexible LIG MSC between single and double laser pass of 2,8 W laser power and 80 mm/s laser scan speed sample..

	Single Pass	Double Pass
Average pore size (µm)	4,63	7,22
SSA (m^2/g)	155,36	118,64
Wettability (°)	60,60	53,91
EIS (Ω)	214	83,90
Power density (mW/cm^2)	4,77E-05	4.87E-05
Energy density ($\mu Wh/cm^2$)	6,98E-07	2.03E-06
Areal Capacitance (mF/cm^2)	2,99	7

4.1.3. Integration of InSe 2D nanomaterials into flexible LIG MSCs

In this study, our objective was to optimize the production of flexible LIG-MSCs by doping LIG with InSe flakes obtained through the liquid phase exfoliation of InSe bulk powder. As seen previously, the zero-band gap of graphene limits its applications in the electronics field, and the challenge with LIG material lies in achieving good material quality, rich in porosity, without sacrificing the material loss and SSA decrease. Thus, our goal in this work is to improve the produced LIG while conserving the high SSA of graphene through the heteroatom doping approach. Although my Ph.D. studies concluded before completing the experiments and achieving comprehensive work, the main challenge was the LPE technique, which required numerous experiments to determine the appropriate parameters of sonication and centrifugation power, speed, time, and temperature, and while I was trying to adjust the laser for this experiment, I have optimized the double-pass laser technique thus during the final year I did a parallel work between studying the double-laser-pass effect and the InSe doping process. In this section, some of the results of the attempts described in the methodology chapter are presented. Although the results obtained are still far from our initial theoretical target of fabricating high-functionality InSe-LIG MSCs compared to those in our previous work, it is noteworthy that our pristine LIG MSCs previously outperformed the doped device. However, these results have significant potential for our future research plan and applications.

4.1.3.a. Outcomes and Interpretation

Based on our initial research path, we focused on the liquid phase exfoliation technique of InSe powder in IPA, in a mixture of ethanol and DI H_2O, and only in DI H_2O. For the doping process, we employed drop-casting, spin-coating, spray-coating, coating, and immersing techniques. We utilized two different structures of MSCs: an in-plane design, where we doped the Kapton film and the LIG after a

single or double laser pass, and a sandwich design, where we doped the LIG and passed the laser for the second time after doping and drying the LIG surface.

Due to time constraints, we performed only one AFM characterization of the first InSe LPE in IPA to measure the resulting particle size. Subsequently, we focused more on the electrochemical characterization part because it is faster compared to other characterization techniques and provides an initial overview of whether our LPE and doping were successful. Figure 4.13 presents an AFM topography characterization of InSe particles resulting from the first exfoliation of InSe in IPA of two different solutions with densities of 0,071 mg/ml (Figure 4.13.a and b) and 0,58 mg/ml (Figure 4.13.c and d) to analyze and measure the particle size of InSe and verify if they are compatible with the porous size of LIG. The IPA-InSe solution with a density of 0,071 mg/ml exhibits large InSe flakes as shown in its AFM topography in Figure 4.13.a, more than 50% of these flakes have a size of 500 µm and between 20 and ~35 % have a size ranging from 200 to 800 µm as shown in Figure 4.13.b.

In Figure 4.13.c the topography of the IPA-InSe solution of 0,58 mg/ml is presented which shows smaller flakes compared to the previous solution and almost 80 % of the flakes have sizes ranging from ~250 to ~750 µm. Apparently, these flakes are larger than the porous size of LIG, hence the maximum open sites obtained after 2 laser passes of high laser power of 2,8 W was with an average of 7,22 µm, means that the LPE parameters used in this experiment were not enough, we need to increase the sonication time or the centrifugation speed or even change the solvent, because with this achieved exfoliated InSe size the flakes will stack only on the top surface of the LIG without any penetrating in the 3D foam graphene-like material structure and this may create an InSe layer above the LIG could block the pores and obstacle the electrolyte ions from the penetration and fat movement between the positive and negative electrodes.

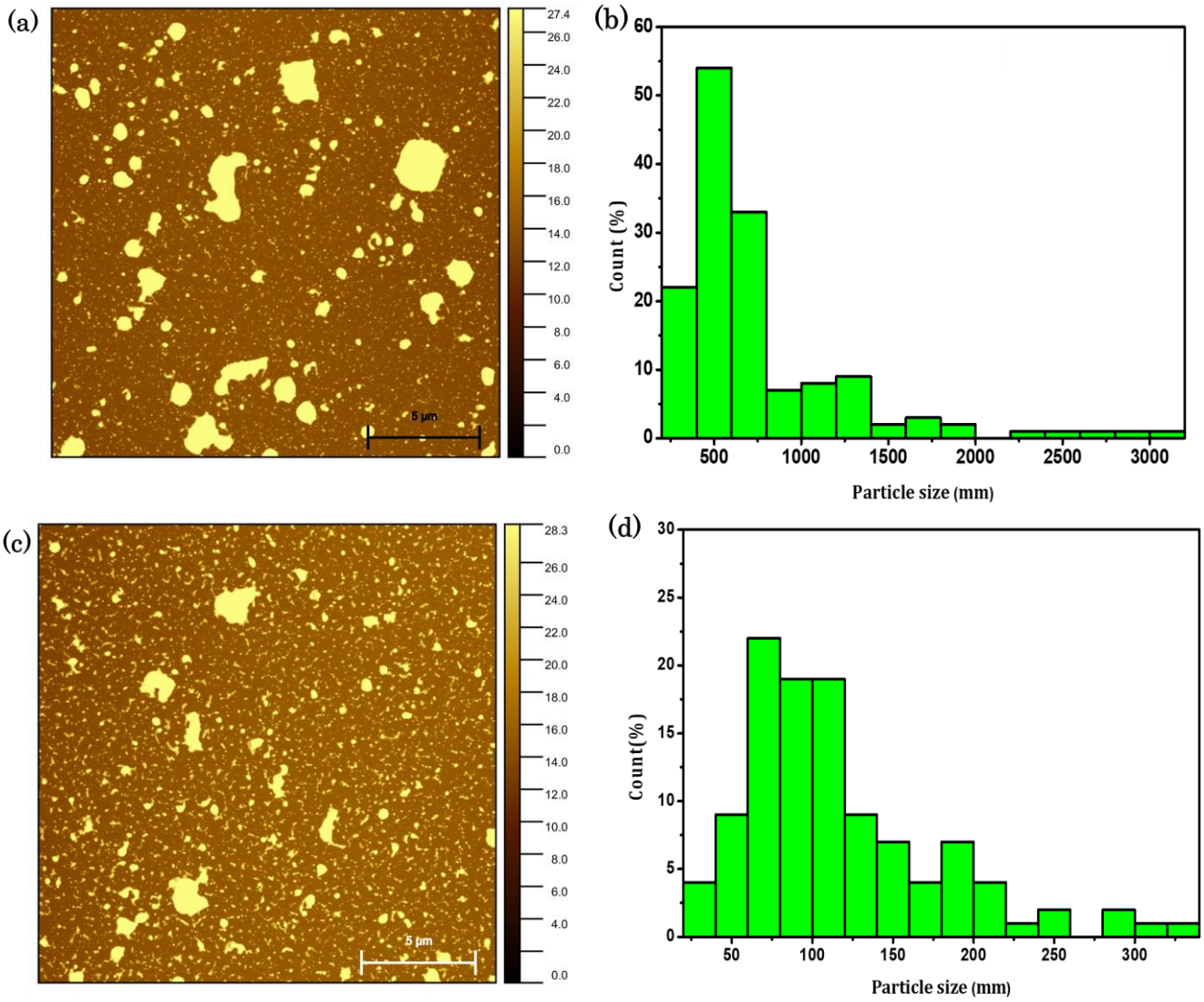

Figure 4.13: AFM topography images (a and c) and particle size (b and d) of the InSe after exfoliating them in IPA. (a, b) corresponding to the solution of 0,071 mg/ml of density and (c, d) 0,58 mg/ml.

For the rest of the LPE experiments, we analyzed our results through the electrochemical measurements of the doped LIG-MSCs because it is the faster characterization technique, and we compared the results with the best LIG-MSCs device (presented in the previous sections) made by our group; however, each time, pristine LIG, either rigid MSCs or flexible MSCs, were much better than the doped devices, Figure 4.14 is a Ragone plot presentation of some results we get depending to 2,8 W-80 mm/s laser power and scan rate respectively comparing to s-2,0-45 our best rigid MSC, and d2,8 the best flexible double pass sample.

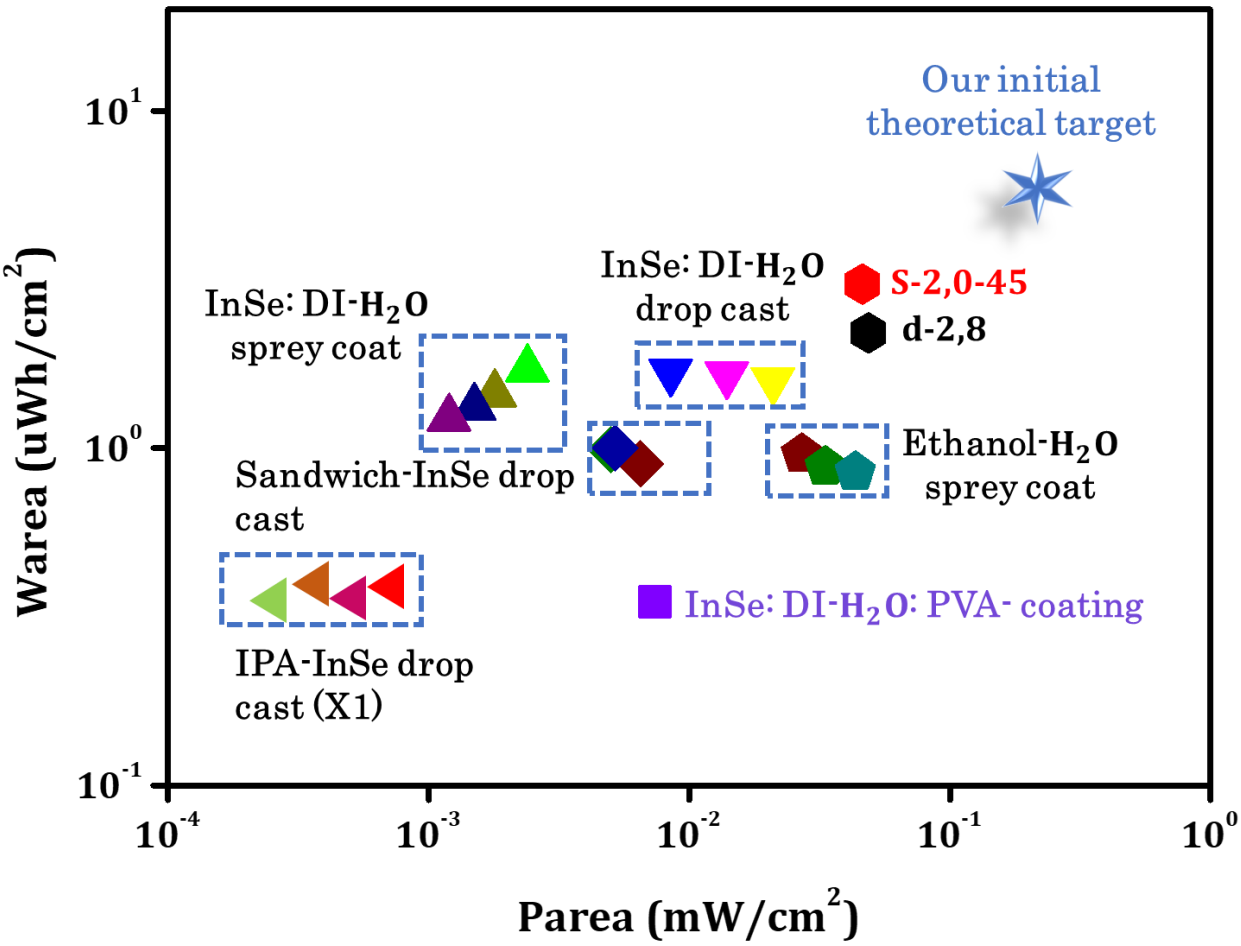

Figure 4.14: Ragon plot presents a comparison between our previous devices, which exhibited high electrochemical performance: s-2,0-45 rigid LIG MSCs (section 4.1.1), d-2,8 flexible LIG MSCs (section 4.1.2), and the InSe-doped LIG flexible MSCs

The LPE process of InSe in IPA proved to be successful because the resulted greenish color was comparable to that in the previous literature [121][116][32], [120] . However, challenges arose as the size of the resulting flakes was excessively large, hindering their fit into the pores created by a single or even double laser pass. Consequently, this led to a reduction in the pore size, which could cause blockages at the open electrode sites. This barrier could impede the penetration of the electrolyte into the LIG electrodes. InSe exfoliation through the filtration process produced a completely transparent solution, indicating that the flake size exceeded the filter's 0,2 µm capacity. This result was attributed to a short sonication time of 5 hours. Coating the LIG area with a mixture of DI water-InSe-

PVA showed promise, despite the PVA quantity being incompatible with the volume of DI water-InSe. This resulted in an overly thick solution. During the vacuum-assisted drying process, no bubbles were observed, raising concerns about the penetration of the coated layer into the LIG material. Similar observations were made when the electrolyte contained PVA.

Regarding doping methods, drop-casting appeared to be the most suitable choice for LIG doping, particularly when doping the hydrophobic Kapton film. The drop-by-drop application ensures successful and controllable doping. The spray coating method is beneficial for doping LIG under low pressure to ensure the doping of LIG. Spin coating, however, proved challenging for micro-areas and solutions with minimal density, as the LIG samples completely dried during various spin coating attempts.

Our goal in doping LIG with InSe is to enhance the performance of MSC devices compared to previous efforts. These trials provide insights into the optimal solvent (IPA), doping method (drop-casting), and laser parameters (double laser pass, creating large open pores). We strongly recommend post-LPE analysis of the flakes and the pore size to assess their compatibility with the LIG material after doping. This comprehensive approach ensures a clearer vision for achieving the best performing MSC device.

4.1.3.b. Conclusion and Perspectives

The utilization of InSe doping to enhance the performance of LIG-MSCs has been substantiated as an effective method, as demonstrated by a previous study involving graphene [113]. Nevertheless, two primary factors have impeded our progress. Firstly, the limited time available has constrained our efforts. Secondly, the LPE technique is considerably more intricate than it appears. It necessitates a multitude of attempts to regulate the conditions of sonication and centrifugation. Moreover, it is imperative to ensure that the particle size is suitable for the LIG pores without obstructing the path of the electrolyte. Despite these obstacles, we are persevering in our endeavours to improve the LPE process or explore

alternative doping techniques, as previously mentioned, such as the ink coating method, electrodepositing, or mixing PI powder and InSe powder to create a doped polymer from the outset. Our ultimate objective is to fabricate a superior polymer that exhibits desirable morphology and structure when subjected to laser application.

4.2. Laser-reduced graphene oxide reduction via UV and IR lasers

Graphene oxide reduction is a top-down method for synthesizing graphene on a large scale by chemically oxidizing graphite to obtain GO, which is then reduced thermally, via laser irradiation, or electrochemically to produce rGO, one of the most promising materials for various electronic, optical, and sensor applications. The laser reduction process is highly desirable among these techniques because of their rapid processing capabilities, affordability, scalability, accuracy, and selectiveness. This study analyses laser reductions on graphene oxide, initially obtained via the modified Hummer method. Here we will focus solely on the laser reduction of graphene oxide synthesized in our laboratory, performed using UV and IR lasers operating through photothermal IR using long-wavelength 10,6 μm CO_2 or by both photochemical and phtothermal effect using the UV 405 nm [56] The resulting rGO samples were structurally and chemically characterized using various techniques including SEM, XRD, BET, and Raman spectroscopy.Upon thorough analysis of the results, it became evident that the laser reduction of GO demonstrates a remarkable capability for highly localized reduction, direct, and flexible patterning at both micro and nanoscales. Remarkably, this process does not necessitate additional chemicals as it is a fast and one-step approach, making it exceptionally suitable for applications such as our field microsupercapacitors within the realm of flexible miniaturized electronics.

4.2.a. Outcomes and Interpretation

After conducting numerous experiments and tests to determine the optimal samples and conditions, as explained in the methodology section, we studied 6 samples, three each for the UV and IR lasers. These samples and the conditions of the experiments are listed in Table 4.6. The names of the samples were as follows: X-LrGO-Y, where X presents the type of laser IR or UV, Y presents the laser power in W in the case of IR CO_2 laser, and in the case of the UV laser, Y presents the laser exposure time of each point in ms/pi.

Table 4.6: Laser reduction samples presentation and experimental parameters Update from ref [32].

Reduction method	Sample	Power (W)	Scan speed (mm/s)	laser exposure time (ms/pi)	Laser type	Temperature
Laser reduction (LrGO)	IR-LrGO-1,6	1,6	100		CO_2	Ambient condition
	IR-LrGO-1,8	1,8				
	IR-LrGO-2,0	2,0				
	UV-LrGO-2			2	UV	
	UV-LrGO-10			10		
	UV-LrGO-50			50		

It is worth noting that for the UV-LrGO-50 sample, the preparation of the LrGO in this part was not finished because the UV laser used was damaged, thus due to the few amounts of UV-LrGO-50 powder, some characterizations such as SEM analysis and carbon percentage calculations were not made for this sample.

SEM analysis, which was performed to investigate the structural morphology of the LrGO samples, is presented in Figure 4.15. The rGO is well expanded, and the 3D open network structure is exfoliated in samples corresponding to the IR laser in Figure 4.15 (a-c) due to the fast release of gases during the reduction treatments of the OCGs applied to the samples [32][139]; However, for samples corresponding to the UV laser, as presented in Figure 4.15.d, showing a prominent 3D framework with overlapped rGO flakes [139], this may be attributed to the slower laser scanning process of UV-LrGO-2, resulting in a slower release of gases and flakes separation and exfoliation. On the contrary, with faster UV laser scanning, sample

UV-LrGO-10 presented in Figure 4.15.e, the surface morphology of rGO is noticeably altered, showing a more pronounced film expansion and approaching the structure observed in materials from the IR reduction process.

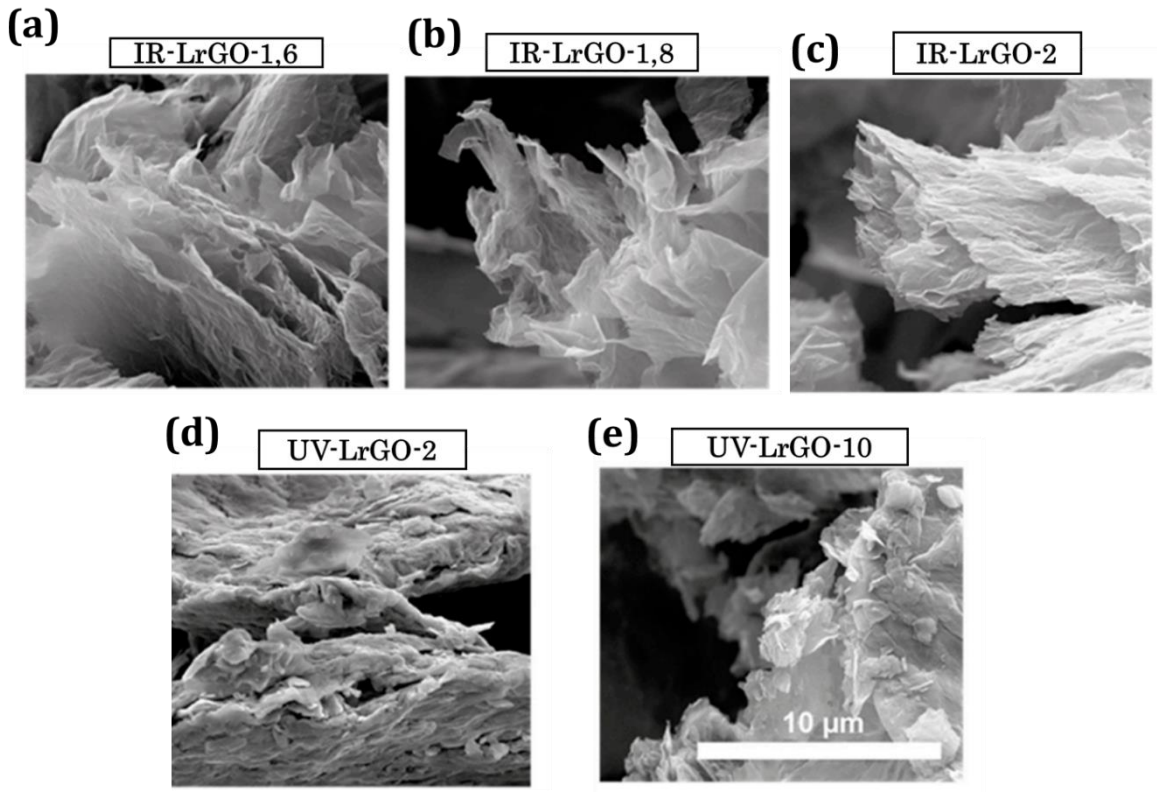

Figure 4.15: SEM images at a 10 µm scale of the GO laser treatments. Updated from ref [32].

The SSAs of the LrGO materials were measured based on the physical adsorption/desorption of nitrogen at 77 K, which was calculated using the BET method. The SSA values obtained from the various laser reduction techniques exhibited significant variability, as presented in Table 4.7; IR-LrGO samples presented an increased SSA and micropore volume when the IR laser power increased, while higher SSA was observed for samples UV-LrGO-10 and UV-LrGO-50 of 107 and 133 m^2/g, respectively with highly expanded micropores.

Table 4.7: Surface analysis of the reduced GO and microscopic porosity analysis of the different LrGO samples. Updated from ref [32].

Sample	SSA(m^2/g)	Micropore volume (cm^3/g)
IR-LrGO-1,6	68	0,0026
IR-LrGO-1,8	84	0,0019
IR-LrGO-2,0	75	0,0013
UV-LrGO-2	49	0,0080
UV-LrGO-10	107	0,010
UV-LrGO-50	133	0,034

The IR-LrGO-2,0, created using the highest power, exhibits a lower SSA than the IR-LrGO-1,8 sample. This difference can be attributed to the laser beam providing a highly localized temperature, a concentrated energy source, and excess power, which can lead to high gas liberations, opening more significant sites in the LrGO structure, and higher material loss [53]. On the other hand, with the UV-LrGO samples, the increase in exposure time at a fixed power value leads to a higher degree of OCG reduction and, consequently, a higher SSA that was observed upon longer exposure times than that of the IR-LrGO samples since the time in the case of UV laser is slower than the laser scanning time using the IR laser. This difference in SSA is believed to result from the OCG reduction mechanism [140], while the dominant GO reduction mechanism has been identified as the highly localized photothermal effect of the IR laser. This mechanism efficiently converts sp^3 carbon into sp^2 bonds [141][56], depending on the parameters used. The dominated photochemical mechanism effectively removes oxygen-containing groups and keeps on the significant SSA while performing on a larger micropore volume [142].

Figure 4.16 and Table 4.8 present the results of the XRD analysis of the GO reduction using the two-laser treatment. The diffraction peak (002) always appears between 25,8° and 25,9° for the IR-LrGO samples and between 26,4°-26,6° for the UV-LrGO samples; this is comparable to the graphite diffraction peak (002) of 26,43°[143].

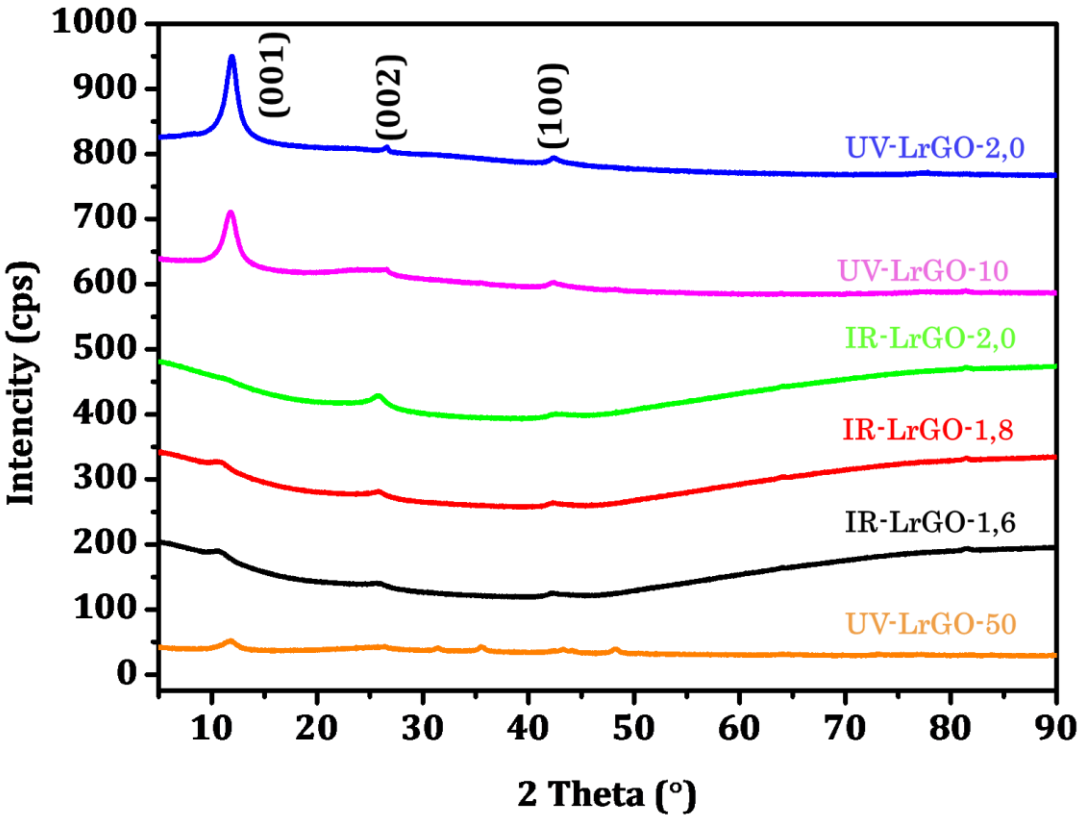

Figure 4.16: XRD peaks of GO were reduced using the two types of laser reduction. Updated from ref [32].

This result confirms that reduced materials tend to revert to the graphite structure after removing OCGs but with decreased crystallinity compared to graphite [144]. The statement suggests an increased distance between the sheets of rGO. In UV-LrGO-2 and UV-LrGO-10 samples, a more prominent peak at approximately 10 ° indicates the reflection of (001), the typical peak of GO due to the lower degree of reduction under these conditions [144]. The (001) reflection disappears slightly after increasing the exposure for the UV-LrGO-50 sample and displays the (002) peaks along with all IR-LrGO samples, indicating the higher degree of reduction, the enhancement of the rGO quality and the smaller distance (d) between the rGO layers, which was determined using Bragg Equation 3.2 applied to the reflection (002). The ideal graphite material has an interlayer spacing of 0,336 nm [145].

Table 4.8. Displays the FWHM values obtained for the reflection (002) measured in degrees 2θ (°); the parameter d represents the average distance between the

rGO layers. At the same time, D1 is the average height of each sample stacking nanolayer for the peak (002), with the constant of Scherrer's equation of 0,9 (Equation 3.3) [143], the parameter n represents the average number of LrGO layers in the graphene stacking nanolayer, and D2 which is the average diameter of each sample stacking nanolayer for the peak (100), with a constant of 1,84. All LrGO samples show an average d spacing of 0,34 nm corresponding to a peak of (002) similar to the interlayer graphite material, demonstrating an efficient GO reduction. The results are consistent with the Scherrer equation presented in Equation 3.3 [146] which was used to determine the size of the crystals in their original state.

Table 4.8: presentation of the structural parameters obtained from the XRD analysis of the IR and UV reduction samples. Updated from ref [32].

	(002) Peak					(100) Peak			
	2θ	**FWHM 2θ (°)**	**d (nm)**	**D1 (nm)**	**n**	**2θ**	**FWHM 2θ (°)**	**d (nm)**	**D2 (nm)**
IR-LrGO-1,6	25,9	1,07	0,34	16	46	42,2	0,80	0,214	43
IR-LrGO-1,8	25,8	1,74	0,34	10	28	42,3	0,80	0,214	43
IR-LrGO-2,0	25,8	0,94	0,34	18	53	42,2	0,94	0,214	37
UV-LrGO-2	26,6	0,30	0,33	57	169	42,4	0,49	0,213	71
UV-LrGO-10	26,6	0,27	0,34	64	190	42,4	0,49	0,213	71
UV-LrGO-50	26,4	0,54	0,34	32	94	43,3	0,49	0,209	71

Based on the calculated data, we can infer that the average diameter of the stacking layer D1 is relatively higher in the UV-laser-reduced samples, indicating a more significant size due to impurity removal and graphitization.

An additional diffraction peak, corresponding to the reflection (100) [147], appears near 2θ = 43 °, indicating a short-range order within the stacked graphene sheets. To evaluate the average diameter D2 of the stacking layers. The Scherrer equation was applied to this reflection (100), with a constant of 1,84 [143]. The resulting values for the average diameter of the stacking layers range from 43 to 71 nm in all LrGO samples (Table 4.8). According to the parameters calculated by XRD, LrGO samples formed of thick graphene layers with varying thicknesses ranging from 28 to 190, arranged in a stacking nanostructure with an average diameter of

around 33 nm × 56 nm and an interatomic distance of 0,34 nm between the graphene layers. In particular, the IR-LrGO samples had smaller stacking nanostructure D2 values than the UV-LrGO.

Another important analysis shows in Figure 4.17 the elemental carbon content in the synthesized rGO samples. These data enable us to evaluate the extent to which reduction has been achieved in the samples. UV-LrGO-2 and UV-LrGO-10 showed a lower carbon content due to an incomplete reduction of GO to rGO, as evident in Figure 4.16 where the peak of GO (001) appears in the XRD analysis. The LrGO materials produced using a UV laser have a carbon concentration that ranges from 49% to 55%. However, the LrGO materials made using an infrared laser have a higher concentration of carbon, ranging from 60% to 70%. It appears that the carbon concentration in the material increases as the exposure time increases when using the UV laser and with the increase of power when using the IR laser. During the laser treatment process, oxygen-containing groups (e.g., epoxy, hydroxyl, and carboxyl) are eliminated [148] primarily through the release of CO and CO_2. If numerous functional oxygen groups are located close to each other, the thermodynamic and kinetic processes of elimination are enhanced [144].

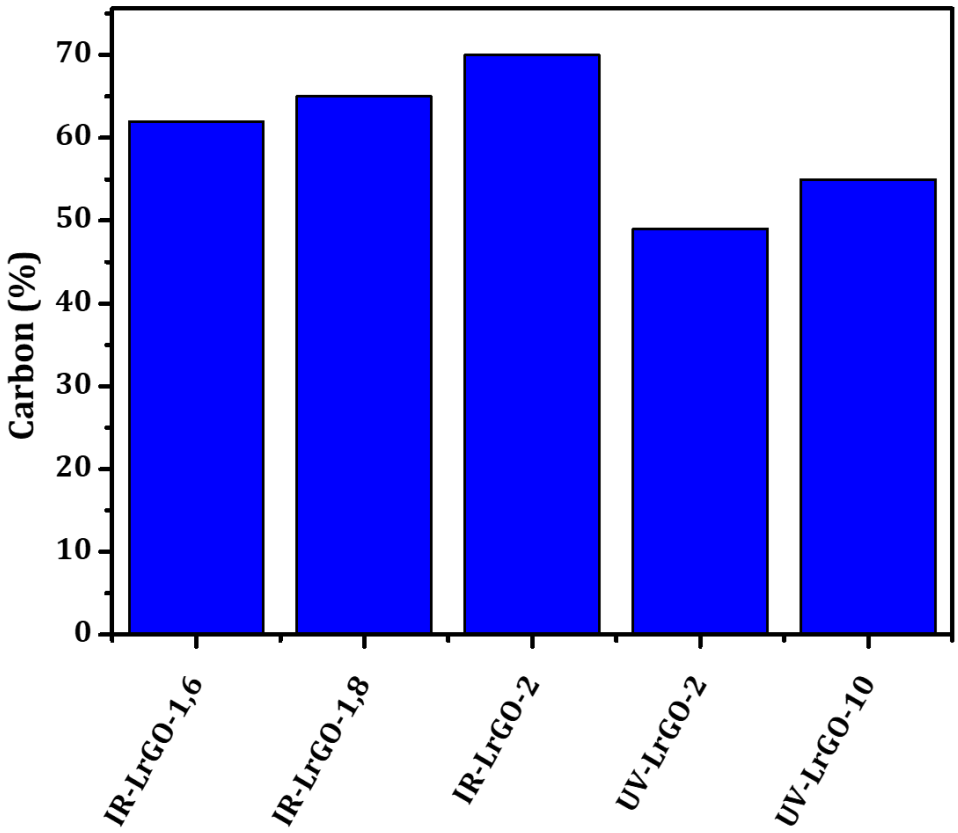

Figure 4.17: Carbon concentrations for the different rGO samples. Updated from ref [32].

Raman spectroscopy, which is an effective optical technique for assessing the architectures of graphene-derived materials, including disordered and defective structures [149] is illustrated in Figure 4.18. For each LrGO sample, three Raman spectra were obtained from different points, which were subsequently analyzed and compared. The similarity of the acquired spectra for each sample confirmed the homogeneity of the samples. The two characteristic graphene peaks, the D band, which is induced by defects in the graphene lattice and is not usually seen in highly ordered graphene layers located approximately ~1350 cm^{-1} and the G band, which results from in-plane vibrations of sp^2 carbon atoms of sp^2 and is the most prominent feature of most graphitic materials that appear at ~1590 cm^{-1}, were exhibited by all samples [150] in addition to the 2D band which appeared slightly and is much more prominent in graphene than in bulk graphite oxide [149].

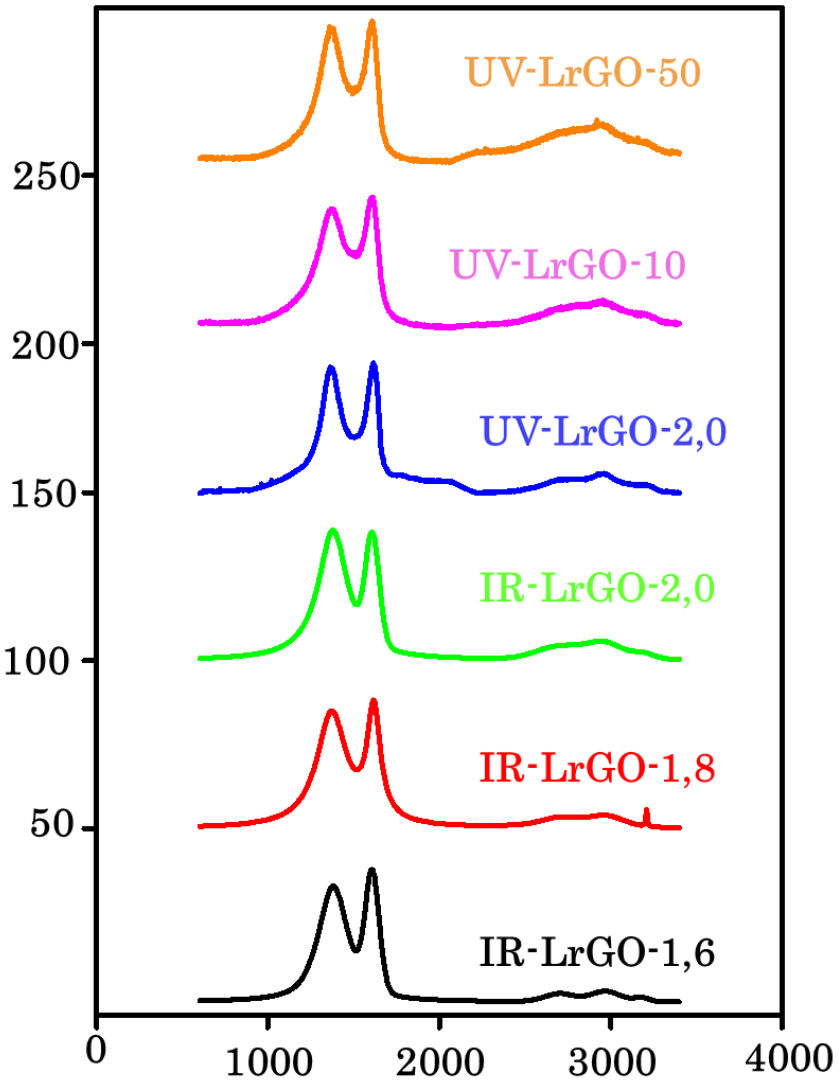

Figure 4.18: Raman spectra profile for IR and UV LrGO samples, and (c) I_D/I_G and I_{2D}/I_G ratios were calculated from Raman spectroscopy of all the TrGO and LrGO samples. Updated from [32].

It is well known that the values of the I_D/I_G and I_{2D}/I_G ratios are widely used to provide structural information about graphene films. These values are calculated and presented in Table 4.9. A higher value of the I_D/I_G ratio is related to the presence of more disordered carbon and/or functionalities attached to the graphene sheets. Meanwhile, a higher value of the I_{2D}/I_G ratio, as well as an increase in intensity and a decrease in the width of the 2D band, is commonly used to indicate the restoration of sp^2-hybridized carbon-carbon bonds in the graphitic structure and the presence of fewer graphene layers [139][151].

Table 4.9: I_D/I_G and I_{2D}/I_G ratio in Raman analysis. Updated from ref [32].

Sample	I_D/I_G	I_{2D}/I_G
IR-LrGO-1,6	1,143	0,092
IR-LrGO-1,8	1,028	0,093
IR-LrGO-2,0	1,233	0,169
UV-LrGO-2	1,040	0,182
UV-LrGO-10	1,067	0,152

IR-LrGO-1,6 sample presents the lowest I_D/I_G ~1,028 hence the less defective and the most graphitized material along with UV-LrGO samples which show comparable I_D/I_G ratios, IR-LrGO-1,6 which exhibits a highly defective material this due to the low power which generates a lower photothermal effect insufficient to reduce the GO, for higher power we suggest that the highly localized temperature induced defects however in terms of I_{2D}/I_G the higher values corresponding to this sample confirmed that 2 W is a high power enough to exfoliate the GO as we have seen before from the SEM characterization, but not to reduce it without damaging the material. The UV samples also demonstrate a few layers of graphene structure.

4.2.b. Conclusion

Graphene oxide laser reduction is a low cost, practical, and a fast process. This study is based on the reduction of graphene oxide using two types of lasers, UV (405 nm) and IR (10,6 μm). The materials produced via the IR reductions exhibited well-exfoliated and expanded LrGO layers, while the UV-LrGO showed a high layer SSA with an expanded micropores morphology, and a stuck sheet that starts to separate slightly with the increasing of the laser exposure time. The average carbon percentage using an IR laser was higher than that of the UV samples; however, in both cases the carbon percentage was increasing with the laser parameters increasing. This technique of LrGO offers a distinct advantage, primarily due to its ability to create precise, detailed patterns with free geometry on thin films. This technique is especially relevant for micro and nanoelectronics

applications that demand miniaturized and flexible devices, such as microsupercapacitors, because of their localized and low-penetration properties. This study demonstrates that graphene materials can be synthesized with custom properties to suit their designated purpose. When factors such as surface area, carbon content, and X-ray and Raman spectra are examined, the resulting material can be identified through its distinctive features, enabling ideal utilization.

5. Conclusions

This Ph.D. thesis has achieved almost all the study objectives that were set at the beginning. The thesis is divided into four parts, including manufacturing solid-state LIG-MSCs, making flexible ones, integrating graphene with 2D materials to improve device performance, and producing graphene in large quantities for various applications.

The first two parts were accomplished successfully, creating solid LIG-MSCs with high-performance and flexible MSCs that retained their performance even after many tests of bending and charging-discharging them 10 K times. The fourth part involved producing large quantities of rGO, which was effectively used in energy storage and flexible-wearable electronic applications. Although the integration of LIG with 2D materials showed great promise in improving the MSC's productivity and the 2D material, InSe is a good choice for our work based on several studies; however, the time constraint of the doctoral program led to the presentation of initial results.

The revised goals of this research aimed to develop energy storage devices that were high-performance, cost-effective, scalable, eco-friendly, and versatile. The work presented in this thesis has significantly contributed to achieving these goals. It has demonstrated substantial progress in enhancing the performance of MSCs using LIG, resulting in improved energy storage capabilities suitable for a wide range of applications. The transition from rigid to flexible substrates has made these devices adaptable to diverse form factors, expanding their utility in addition, we have proved the versatility of this approach not only in the MSCs field but also in strain sensors also. Another notable contribution was the development of Laser-Induced Graphene Oxide, which offers a low-cost and large-area solution for energy storage. This innovation has the potential to disrupt conventional energy storage technologies, opening doors for the creation of more affordable and scalable energy storage systems, flexible, and wearable electronic devices.

The low-cost fabrication technique employed through DLW has the potential to revolutionize the manufacturing of microsupercapacitors, enabling their

widespread deployment. Additionally, incorporating micropore networks and doping with 2D materials nanoparticles has significantly improved their performance, further cementing their viability in energy storage applications. We have demonstrated that this LIG-modern multipurpose technology has the potential to be used in different applications.

The work presented in this thesis represents a significant advancement in energy storage technology and paves the way for a promising future in this field. The outlook for this research includes continued exploration of novel LIG-based energy storage devices that are stretchable and wearable. Enhancing their performance through doping will enable commercialization and integration into various applications. Additionally, further research on the scalability, durability, and environmental impact of LIG-based technologies is essential to ensure their long-term viability. We aim to continue with the InSe-LIG doping by trying more doping techniques like electrodeposition, inkjet, and preparing doped precursors. We will focus more on the electrolyte properties like ion size and their suitability with the LIG porose size. Changing the other laser parameters like the scan line, the beam size, the temperature, and the focus distance, trying to combine two laser types, for example, continuous and pulsed laser, and doping the LIG with more than one dopant material. LrGO is an attractive material for our applications, as we conclude from our comparison study. It is a promising material that produces flexible and wearable microelectronic devices.

To conclude, the findings and contributions of this Ph.D. thesis provide a robust foundation for the development of advanced energy storage solutions based on Laser-Induced Graphene technology. These innovations could reshape the landscape of energy storage technologies, making them more efficient, cost-effective, and sustainable. As the world continues to seek sustainable energy solutions, this research is poised to play a pivotal role in addressing the growing energy challenges of the future.

References

[1] "International Database." Accessed: Mar. 30, 2024. https://www.census.gov/datatools/demo/idb/#/dashboard?COUNTRY_YEAR=2024&COUNTRY_YR_ANIM=2024

[2] "Executive summary – Electricity Market Report – Update 2023 – Analysis - IEA." Accessed: Mar. 31, 2024. [Online]. Available: https://www.iea.org/reports/electricity-market-report-update-2023/executive-summary

[3] "Taking Stock: How Close Are We to a Sustainable Energy Transition? | Freedom of Mobility Forum." Accessed: Mar. 31, 2024. [Online]. Available: https://www.freedomofmobility.stellantis.com/en/featured-content/2023/taking-stock-how-close-are-we-to-a-sustainable-energy-transition

[4] "THE 17 GOALS | Sustainable Development." Accessed: Mar. 31, 2024. [Online]. Available: https://sdgs.un.org/goals

[5] P. Simon and Y. Gogotsi, "Materials for electrochemical capacitors," nature materials |, vol. 7, pp. 845–854, 2008, Accessed: Feb. 28, 2024. [Online]. Available: https://doi.org/10.1038/nmat2297

[6] P. Simon and Y. Gogotsi, "Perspectives for electrochemical capacitors and related devices," 2020. doi: 10.1038/s41563-020-0747-z.

[7] "53-Materials for electrochemical capacitors".

[8] J. Mitali, S. Dhinakaran, and A. A. Mohamad, "Energy storage systems: a review," Energy Storage and Saving, vol. 1, no. 3. Elsevier B.V., pp. 166–216, Sep. 01, 2022. doi: 10.1016/j.enss.2022.07.002.

[9] C. Zhong, Y. Deng, W. Hu, J. Qiao, L. Zhang, and J. Zhang, "A review of electrolyte materials and compositions for electrochemical supercapacitors," Chemical Society Reviews, vol. 44, no. 21. Royal Society of Chemistry, pp. 7484–7539, Nov. 07, 2015. doi: 10.1039/c5cs00303b.

[10] K. A. Madurani, S. Suprapto, N. I. Machrita, S. L. Bahar, W. Illiya, and F. Kurniawan, "Progress in Graphene Synthesis and its Application: History, Challenge and the Future Outlook for Research and Industry," ECS Journal of Solid State Science and Technology, vol. 9, no. 9, p. 093013, Oct. 2020, doi: 10.1149/2162-8777/abbb6f.

[11] K. S. Novoselov et al., "Electric Field Effect in Atomically Thin Carbon Films," Kluwer, 2000. [Online]. Available: http://science.sciencemag.org/

[12] A. K. Geim and K. S. Novoselov, "The rise of graphene." [Online]. Available: www.nature.com/naturematerials

[13] Y. Bin Tan and J. M. Lee, "Graphene for supercapacitor applications," J Mater Chem A Mater, vol. 1, no. 47, pp. 14814–14843, Dec. 2013, doi: 10.1039/c3ta12193c.

[14] A. K. Geim, "Random walk to graphene (Nobel lecture)," Angewandte Chemie - International Edition, vol. 50, no. 31. pp. 6966–6985, Jul. 25, 2011. doi: 10.1002/anie.201101174.

[15] C. V. Kumar and A. Pattammattel, "Discovery of graphene and beyond," in Introduction to Graphene, Elsevier, 2017, pp. 1–15. doi: 10.1016/b978-0-12-813182-4.00001-5.

[16] A. K. Geim, "Graphene prehistory," Phys Scr, no. T146, Jan. 2012, doi: 10.1088/0031-8949/2012/T146/014003.

[17] K. S. Novoselov et al., "Electric Field Effect in Atomically Thin Carbon Films," Kluwer, 2004. [Online]. Available: http://science.sciencemag.org/

[18] C. Berger et al., "Ultrathin epitaxial graphite: 2D electron gas properties and a route toward graphene-based nanoelectronics," Journal of Physical Chemistry B, vol. 108, no. 52, pp. 19912–19916, Dec. 2004, doi: 10.1021/jp040650f.

[19] C. Soldano, A. Mahmood, and E. Dujardin, "Production, properties and potential of graphene," Carbon, vol. 48, no. 8. pp. 2127–2150, Jul. 2010. doi: 10.1016/j.carbon.2010.01.058.

[20] J. Wang, F. Ma, and M. Sun, “Graphene, hexagonal boron nitride, and their heterostructures: properties and applications,” RSC Advances, vol. 7, no. 27. Royal Society of Chemistry, pp. 16801–16822, 2017. doi: 10.1039/c7ra00260b.

[21] D. R. Cooper et al., “Experimental Review of Graphene,” ISRN Condensed Matter Physics, vol. 2012, pp. 1–56, Apr. 2012, doi: 10.5402/2012/501686.

[22] G. Yang, L. Li, W. B. Lee, and M. C. Ng, “Structure of graphene and its disorders: a review,” Science and Technology of Advanced Materials, vol. 19, no. 1. Taylor and Francis Ltd., pp. 613–648, Dec. 31, 2018. doi: 10.1080/14686996.2018.1494493.

[23] M. O. Goerbig, “Electronic properties of graphene in a strong magnetic field,” Rev Mod Phys, vol. 83, no. 4, Nov. 2011, doi: 10.1103/RevModPhys.83.1193.

[24] A. R. Urade, I. Lahiri, and K. S. Suresh, “Graphene Properties, Synthesis and Applications: A Review,” JOM, vol. 75, no. 3. Springer, pp. 614–630, Mar. 01, 2023. doi: 10.1007/s11837-022-05505-8.

[25] K. S. Novoselov, V. I. Fal’Ko, L. Colombo, P. R. Gellert, M. G. Schwab, and K. Kim, “A roadmap for graphene,” Nature, vol. 490, no. 7419. pp. 192–200, Oct. 11, 2012. doi: 10.1038/nature11458.

[26] D. S. Schulman, A. J. Arnold, and S. Das, “Contact engineering for 2D materials and devices,” Chemical Society Reviews, vol. 47, no. 9. Royal Society of Chemistry, pp. 3037–3058, May 07, 2018. doi: 10.1039/c7cs00828g.

[27] K. Zhang, Y. Feng, F. Wang, Z. Yang, and J. Wang, “Two dimensional hexagonal boron nitride (2D-hBN): Synthesis, properties and applications,” Journal of Materials Chemistry C, vol. 5, no. 46. Royal Society of Chemistry, pp. 11992–12022, 2017. doi: 10.1039/c7tc04300g.

[28] Y. Xu, Z. Shi, X. Shi, K. Zhang, and H. Zhang, “Recent progress in black phosphorus and black-phosphorus-analogue materials: Properties, synthesis and applications,” Nanoscale, vol. 11, no. 31. Royal Society of Chemistry, pp. 14491–14527, Aug. 21, 2019. doi: 10.1039/c9nr04348a.

[29] Y. Gogotsi and B. Anasori, “The Rise of MXenes,” ACS Nano, vol. 13, no. 8. American Chemical Society, pp. 8491–8494, Aug. 27, 2019. doi: 10.1021/acsnano.9b06394.

[30] N. R. Glavin et al., “Emerging Applications of Elemental 2D Materials,” Advanced Materials, vol. 32, no. 7. Wiley-VCH Verlag, Feb. 01, 2020. doi: 10.1002/adma.201904302.

[31] R. S. Edwards and K. S. Coleman, “Graphene synthesis: Relationship to applications,” Nanoscale, vol. 5, no. 1, pp. 38–51, Jan. 2013, doi: 10.1039/c2nr32629a.

[32] M. B. Gómez-Mancebo et al., “Comparison of Thermal and Laser-Reduced Graphene Oxide Production for Energy Storage Applications,” Nanomaterials, vol. 13, no. 8, Apr. 2023, doi: 10.3390/nano13081391.

[33] A. Razaq, F. Bibi, X. Zheng, R. Papadakis, S. H. M. Jafri, and H. Li, “Review on Graphene-, Graphene Oxide-, Reduced Graphene Oxide-Based Flexible Composites: From Fabrication to Applications,” Materials, vol. 15, no. 3. MDPI, Feb. 01, 2022. doi: 10.3390/ma15031012.

[34] A. R. Urade, I. Lahiri, and K. S. Suresh, “Graphene Properties, Synthesis and Applications: A Review,” JOM, vol. 75, no. 3. Springer, pp. 614–630, Mar. 01, 2023. doi: 10.1007/s11837-022-05505-8.

[35] C. Huo, Z. Yan, X. Song, and H. Zeng, “2D materials via liquid exfoliation: a review on fabrication and applications,” Science Bulletin, vol. 60, no. 23. Science in China Press, pp. 1994–2008, Dec. 01, 2015. doi: 10.1007/s11434-015-0936-3.

[36] J. Shen et al., “Surface Tension Components Based Selection of Cosolvents for Efficient Liquid Phase Exfoliation of 2D Materials,” Small, vol. 12, no. 20, pp. 2741–2749, May 2016, doi: 10.1002/smll.201503834.

[37] H. Li et al., “Liquid phase exfoliation of indium selenide: Achieving the optimum exfoliating parameters and unraveling the mechanism,” Progress in Natural Science: Materials International, vol. 32, no. 6, pp. 700–704, Dec. 2022, doi: 10.1016/j.pnsc.2022.10.006.

[38] C. Huo, Z. Yan, X. Song, and H. Zeng, "2D materials via liquid exfoliation: a review on fabrication and applications," Science Bulletin, vol. 60, no. 23. Science in China Press, pp. 1994–2008, Dec. 01, 2015. doi: 10.1007/s11434-015-0936-3.

[39] Y. Xu, H. Cao, Y. Xue, B. Li, and W. Cai, "Liquid-phase exfoliation of graphene: An overview on exfoliation media, techniques, and challenges," Nanomaterials, vol. 8, no. 11. MDPI AG, Nov. 09, 2018. doi: 10.3390/nano8110942.

[40] H. Tetlow, J. Posthuma de Boer, I. J. Ford, D. D. Vvedensky, J. Coraux, and L. Kantorovich, "Growth of epitaxial graphene: Theory and experiment," Physics Reports, vol. 542, no. 3. Elsevier B.V., pp. 195–295, Sep. 20, 2014. doi: 10.1016/j.physrep.2014.03.003.

[41] A. Gutiérrez-Cruz, A. R. Ruiz-Hernández, J. F. Vega-Clemente, D. G. Luna-Gazcón, and J. Campos-Delgado, "A review of top-down and bottom-up synthesis methods for the production of graphene, graphene oxide and reduced graphene oxide," Journal of Materials Science, vol. 57, no. 31. Springer, pp. 14543–14578, Aug. 01, 2022. doi: 10.1007/s10853-022-07514-z.

[42] M. Bahri et al., "Recent advances in chemical vapour deposition techniques for graphene-based nanoarchitectures: From synthesis to contemporary applications," Coordination Chemistry Reviews, vol. 475. Elsevier B.V., Jan. 15, 2023. doi: 10.1016/j.ccr.2022.214910.

[43] M. S. A. Bhuyan, M. N. Uddin, M. M. Islam, F. A. Bipasha, and S. S. Hossain, "Synthesis of graphene," International Nano Letters, vol. 6, no. 2. Springer Science and Business Media, LLC, pp. 65–83, Jun. 01, 2016. doi: 10.1007/s40089-015-0176-1.

[44] R. Muñoz and C. Gómez-Aleixandre, "Review of CVD synthesis of graphene," Chemical Vapor Deposition, vol. 19, no. 10–12. pp. 297–322, Dec. 2013. doi: 10.1002/cvde.201300051.

[45] Y. Zhang, L. Zhang, and C. Zhou, "Review of chemical vapor deposition of graphene and related applications," Acc Chem Res, vol. 46, no. 10, pp. 2329–2339, Oct. 2013, doi: 10.1021/ar300203n.

[46] R. You, Y. Q. Liu, Y. L. Hao, D. D. Han, Y. L. Zhang, and Z. You, "Laser Fabrication of Graphene-Based Flexible Electronics," Advanced Materials, vol. 32, no. 15, Apr. 2020, doi: 10.1002/adma.201901981.

[47] G. Li, "Direct laser writing of graphene electrodes," J Appl Phys, vol. 127, no. 1, Jan. 2020, doi: 10.1063/1.5120056.

[48] Z. Wan, X. Chen, and M. Gu, "Laser scribed graphene for supercapacitors," Opto-Electronic Advances, vol. 4, no. 7. Chinese Academy of Sciences, 2021. doi: 10.29026/oea.2021.200079.

[49] J. Lin et al., "Laser-induced porous graphene films from commercial polymers," Nat Commun, vol. 5, 2014, doi: 10.1038/ncomms6714.

[50] V. Strong et al., "Patterning and electronic tuning of laser scribed graphene for flexible all-carbon devices," ACS Nano, vol. 6, no. 2, pp. 1395–1403, Feb. 2012, doi: 10.1021/nn204200w.

[51] Y. Li et al., "Laser-Induced Graphene in Controlled Atmospheres: From Superhydrophilic to Superhydrophobic Surfaces," Advanced Materials, vol. 29, no. 27, Jul. 2017, doi: 10.1002/adma.201700496.

[52] A. Lamberti et al., "New insights on laser-induced graphene electrodes for flexible supercapacitors: Tunable morphology and physical properties," Nanotechnology, vol. 28, no. 17, Apr. 2017, doi: 10.1088/1361-6528/aa6615.

[53] A. Velasco, Y. K. Ryu, A. Hamada, A. de Andrés, F. Calle, and J. Martinez, "Laser-Induced Graphene Microsupercapacitors: Structure, Quality, and Performance," Nanomaterials, vol. 13, no. 5, Mar. 2023, doi: 10.3390/nano13050788.

[54] M. F. El-Kady and R. B. Kaner, "Scalable fabrication of high-power graphene micro-supercapacitors for flexible and on-chip energy storage," Nat Commun, vol. 4, 2013, doi: 10.1038/ncomms2446.

[55] Y. Chyan, R. Ye, Y. Li, S. P. Singh, C. J. Arnusch, and J. M. Tour, "Laser-Induced Graphene by Multiple Lasing: Toward Electronics on Cloth, Paper, and Food," ACS Nano, vol. 12, no. 3, pp. 2176–2183, Mar. 2018, doi: 10.1021/acsnano.7b08539.

[56] G. Li, “Direct laser writing of graphene electrodes,” J Appl Phys, vol. 127, no. 1, Jan. 2020, doi: 10.1063/1.5120056.

[57] T. S. D. Le et al., “Recent Advances in Laser-Induced Graphene: Mechanism, Fabrication, Properties, and Applications in Flexible Electronics,” Advanced Functional Materials, vol. 32, no. 48. John Wiley and Sons Inc, Nov. 24, 2022. doi: 10.1002/adfm.202205158.

[58] C. Zhou et al., “Laser-induced bi-metal sulfide/graphene nanoribbon hybrid frameworks for high-performance all-in-one fiber supercapacitors,” J Power Sources, vol. 438, Oct. 2019, doi: 10.1016/j.jpowsour.2019.227044.

[59] E. C. Cho et al., “PEDOT-modified laser-scribed graphene films as bginder– and metallic current collector–free electrodes for large-sized supercapacitors,” Appl Surf Sci, vol. 518, Jul. 2020, doi: 10.1016/j.apsusc.2020.146193.

[60] W. Song et al., “Flexible, Stretchable, and Transparent Planar Microsupercapacitors Based on 3D Porous Laser-Induced Graphene,” Small, vol. 14, no. 1, Jan. 2018, doi: 10.1002/smll.201702249.

[61] W. Wang et al., “A Highly Stretchable Microsupercapacitor Using Laser-Induced Graphene/NiO/Co3O4 Electrodes on a Biodegradable Waterborne Polyurethane Substrate,” Adv Mater Technol, vol. 5, no. 2, Feb. 2020, doi: 10.1002/admt.201900903.

[62] W. Wang et al., “Tailoring the surface morphology and nanoparticle distribution of laser-induced graphene/Co3O4 for high-performance flexible microsupercapacitors,” Appl Surf Sci, vol. 504, Feb. 2020, doi: 10.1016/j.apsusc.2019.144487.

[63] H. Wu, W. Zhang, S. Kandambeth, O. Shekhah, M. Eddaoudi, and H. N. Alshareef, “Conductive Metal–Organic Frameworks Selectively Grown on Laser-Scribed Graphene for Electrochemical Microsupercapacitors,” Adv Energy Mater, vol. 9, no. 21, Jun. 2019, doi: 10.1002/aenm.201900482.

[64] L. Li et al., “High-Performance Pseudocapacitive Microsupercapacitors from Laser-Induced Graphene,” Advanced Materials, vol. 28, no. 5, pp. 838–845, Feb. 2016, doi: 10.1002/adma.201503333.

[65] H. Liu et al., “Laser-oxidized Fe3O4 nanoparticles anchored on 3D macroporous graphene flexible electrodes for ultrahigh-energy in-plane hybrid micro-supercapacitors,” Nano Energy, vol. 77, Nov. 2020, doi: 10.1016/j.nanoen.2020.105058.

[66] C. Zhang et al., “High-energy all-in-one stretchable micro-supercapacitor arrays based on 3D laser-induced graphene foams decorated with mesoporous ZnP nanosheets for self-powered stretchable systems,” Nano Energy, vol. 81, Mar. 2021, doi: 10.1016/j.nanoen.2020.105609.

[67] Z. Peng et al., “Flexible Boron-Doped Laser-Induced Graphene Microsupercapacitors,” ACS Nano, vol. 9, no. 6, pp. 5868–5875, Jun. 2015, doi: 10.1021/acsnano.5b00436.

[68] H. Liu et al., “Laser-induced and KOH-activated 3D graphene: A flexible activated electrode fabricated via direct laser writing for in-plane micro-supercapacitors,” Chemical Engineering Journal, vol. 393, Aug. 2020, doi: 10.1016/j.cej.2020.124672.

[69] F. Clerici et al., “In situ MoS2 Decoration of Laser-Induced Graphene as Flexible Supercapacitor Electrodes,” ACS Appl Mater Interfaces, vol. 8, no. 16, pp. 10459–10465, Apr. 2016, doi: 10.1021/acsami.6b00808.

[70] S. Han et al., “One-step fabrication of nitrogen-doped laser-induced graphene derived from melamine/polyimide for enhanced flexible supercapacitors,” CrystEngComm, vol. 24, no. 10, pp. 1866–1876, 2022, doi: 10.1039/d1ce01608c.

[71] K. Y. Kim, H. Choi, C. Van Tran, and J. Bin In, “Simultaneous densification and nitrogen doping of laser-induced graphene by duplicated pyrolysis for supercapacitor applications,” J Power Sources, vol. 441, Nov. 2019, doi: 10.1016/j.jpowsour.2019.227199.

[72] M. Khandelwal, C. Van Tran, J. Lee, and J. Bin In, “Nitrogen and boron co-doped densified laser-induced graphene for supercapacitor applications,” Chemical Engineering Journal, vol. 428, Jan. 2021, doi: 10.1016/j.cej.2021.131119.

[73] M. Khandelwal, C. Van Tran, and J. Bin In, “Nitrogen and phosphorous Co-Doped Laser-Induced Graphene: A High-Performance electrode material for supercapacitor applications,” Appl Surf Sci, vol. 576, Feb. 2022, doi: 10.1016/j.apsusc.2021.151714.

[74] M. Khandelwal, A. P. Nguyen, C. Van Tran, and J. Bin In, “Simple fabrication of Co3O4nanoparticles on N-doped laser-induced graphene for high-performance supercapacitors,” RSC Adv, vol. 11, no. 61, pp. 38547–38554, Nov. 2021, doi: 10.1039/d1ra08048b.

[75] R. Xu, Z. Wang, L. Gao, S. Wang, and J. Zhao, “Effective design of MnO2 nanoparticles embedded in laser-induced graphene as shape-controllable electrodes for flexible planar microsupercapacitors,” Appl Surf Sci, vol. 571, Jan. 2022, doi: 10.1016/j.apsusc.2021.151385.

[76] M. Yuan et al., “Facile and Scalable Fabrication of High-Performance Microsupercapacitors Based on Laser-Scribed in Situ Heteroatom-Doped Porous Graphene,” ACS Appl Mater Interfaces, vol. 13, no. 19, pp. 22426–22437, May 2021, doi: 10.1021/acsami.1c03219.

[77] Z. Peng et al., “High-energy all-in-one micro-supercapacitors based on ZnO mesoporous nanosheet-decorated laser-induced porous graphene foams,” J Mater Res, vol. 36, no. 9, pp. 1927–1936, May 2021, doi: 10.1557/s43578-021-00228-z.

[78] W. Yang et al., “In situ formation of phosphorus-doped porous graphene via laser induction,” RSC Adv, vol. 10, no. 40, pp. 23953–23958, Jun. 2020, doi: 10.1039/d0ra03363d.

[79] Y. Rao, M. Yuan, F. Luo, H. Li, J. Yu, and X. Chen, “Laser In-Situ synthesis of metallic cobalt decorated porous graphene for flexible In-Plane microsupercapacitors,” J Colloid Interface Sci, vol. 610, pp. 775–784, Mar. 2022, doi: 10.1016/j.jcis.2021.11.116.

[80] M. Yuan et al., “Laser synthesis of superhydrophilic O/S co-doped porous graphene derived from sodium lignosulfonate for enhanced microsupercapacitors,” J Power Sources, vol. 513, Nov. 2021, doi: 10.1016/j.jpowsour.2021.230558.

[81] H. Liu et al., “Laser-induced nitrogen-self-doped graphite nanofibers from cyanate ester for on-chip micro-supercapacitors,” Chemical Engineering Journal, vol. 404, Jan. 2021, doi: 10.1016/j.cej.2020.126375.

[82] Y. Rao et al., “One-step laser fabrication of phosphorus-doped porous graphene electrodes for high-performance flexible microsupercapacitor,” Carbon N Y, vol. 180, pp. 56–66, Aug. 2021, doi: 10.1016/j.carbon.2021.05.001.

[83] C. Chen and C. Yang, “Laser-Induced Nitrogen-doped Graphene for High-Performance Flexible Supercapacitors; Laser-Induced Nitrogen-doped Graphene for High-Performance Flexible Supercapacitors,” 2020.

[84] R. Xu, P. Liu, G. Ji, L. Gao, and J. Zhao, “Versatile strategy to design flexible planar-integrated microsupercapacitors based on Co3O4-decorated laser-induced graphene,” ACS Appl Energy Mater, vol. 3, no. 11, pp. 10676–10684, Nov. 2020, doi: 10.1021/acsaem.0c01744.

[85] S. Bai et al., “Phosphor copper-based flexible high voltage supercapacitors fabricated via laser irradiation and three-dimensional packaging,” J Power Sources, vol. 507, Sep. 2021, doi: 10.1016/j.jpowsour.2021.230257.

[86] H. He, Y. Liu, P. R. Shearing, G. He, and D. J. L. Brett, “Mesoporous Carbon for Supercapacitors,” 2022, pp. 147–163. doi: 10.1007/978-3-030-99302-3_7.

[87] T. An et al., “A Wearable Second Skin-Like Multifunctional Supercapacitor with Vertical Gold Nanowires and Electrochromic Polyaniline,” Adv Mater Technol, vol. 4, no. 3, Mar. 2019, doi: 10.1002/admt.201800473.

[88] X. Li et al., “High-Voltage Flexible Microsupercapacitors based on Laser-induced Graphene,” 2018. [Online]. Available: http://pubs.acs.org

[89] S. Sollami Delekta, M. M. Laurila, M. Mäntysalo, and J. Li, “Drying-Mediated Self-Assembly of Graphene for Inkjet Printing of High-Rate Micro-supercapacitors,” Nanomicro Lett, vol. 12, no. 1, Jan. 2020, doi: 10.1007/s40820-020-0368-8.

[90] A. Philip and A. Ruban Kumar, “Recent advancements and developments employing 2D-materials in enhancing the performance of electrochemical supercapacitors: A review,” Renewable and Sustainable Energy Reviews, vol. 182. Elsevier Ltd, Aug. 01, 2023. doi: 10.1016/j.rser.2023.113423.

[91] W. Dong, M. Xie, S. Zhao, Q. Qin, and F. Huang, “Materials design and preparation for high energy density and high power density electrochemical supercapacitors,” Materials Science and Engineering R: Reports, vol. 152. Elsevier Ltd, Feb. 01, 2023. doi: 10.1016/j.mser.2022.100713.

[92] M. Conte, “Supercapacitors technical requirements fornew applications,” Fuel Cells, vol. 10, no. 5. John Wiley and Sons Ltd, pp. 806–818, 2010. doi: 10.1002/fuce.201000087.

[93] A. Noori, M. F. El-Kady, M. S. Rahmanifar, R. B. Kaner, and M. F. Mousavi, “Towards establishing standard performance metrics for batteries, supercapacitors and beyond,” Chemical Society Reviews, vol. 48, no. 5. Royal Society of Chemistry, pp. 1272–1341, Mar. 07, 2019. doi: 10.1039/c8cs00581h.

[94] S. Kim and P. H. Chou, “Energy harvesting: Energy harvesting with supercapacitor-based energy storage,” in Smart Sensors and Systems, Springer International Publishing, 2015, pp. 215–241. doi: 10.1007/978-3-319-14711-6_10.

[95] M. Yaseen et al., “A review of supercapacitors: Materials design, modification, and applications,” Energies, vol. 14, no. 22. MDPI, Nov. 01, 2021. doi: 10.3390/en14227779.

[96] J. O. Dennis et al., “A Review of Current Trends on Polyvinyl Alcohol (PVA)-Based Solid Polymer Electrolytes,” Molecules, vol. 28, no. 4. MDPI, Feb. 01, 2023. doi: 10.3390/molecules28041781.

[97] D. Qi, Y. Liu, Z. Liu, L. Zhang, and X. Chen, “Design of Architectures and Materials in In-Plane Micro-supercapacitors: Current Status and Future Challenges,” Advanced Materials, vol. 29, no. 5. Wiley-VCH Verlag, Feb. 02, 2017. doi: 10.1002/adma.201602802.

[98] N. Kurra and Q. Jiang, “Supercapacitors,” in Storing Energy: with Special Reference to Renewable Energy Sources, Elsevier, 2022, pp. 383–417. doi: 10.1016/B978-0-12-824510-1.00017-9.

[99] V. S. Marin Halper James C Ellenbogen, “Supercapacitors: A Brief Overview MITRE MITRE MITRE MITRE,” 2006. [Online]. Available: http://www.mitre.org/tech/nanotech

[100] M. Conte, “Supercapacitors technical requirements fornew applications,” Fuel Cells, vol. 10, no. 5. John Wiley and Sons Ltd, pp. 806–818, 2010. doi: 10.1002/fuce.201000087.

[101] H. C. Li, H. R. Shen, Y. Shi, L. Wen, and F. Li, “Progress and prospects of graphene for in-plane micro-supercapacitors,” Xinxing Tan Cailiao/New Carbon Materials, vol. 37, no. 5. Institute of Metal Research Chinese Academy of Sciences, pp. 781–801, Oct. 01, 2022. doi: 10.1016/S1872-5805(22)60640-1.

[102] A. Tiliakos, C. Ceaus, S. M. Iordache, E. Vasile, and I. Stamatin, “Morphic transitions of nanocarbons via laser pyrolysis of polyimide films,” J Anal Appl Pyrolysis, vol. 121, pp. 275–286, Sep. 2016, doi: 10.1016/j.jaap.2016.08.007.

[103] A. Vashisth, M. Kowalik, J. C. Gerringer, C. Ashraf, A. C. T. Van Duin, and M. J. Green, “ReaxFF Simulations of Laser-Induced Graphene (LIG) Formation for Multifunctional Polymer Nanocomposites,” ACS Appl Nano Mater, vol. 3, no. 2, pp. 1881–1890, Feb. 2020, doi: 10.1021/acsanm.9b02524.

[104] W. Zhang, Y. Lei, Q. Jiang, F. Ming, P. M. F. J. Costa, and H. N. Alshareef, “3D Laser Scribed Graphene Derived from Carbon

Nanospheres: An Ultrahigh-Power Electrode for Supercapacitors," Small Methods, vol. 3, no. 5, May 2019, doi: 10.1002/smtd.201900005.

[105] C. A. Barbero and D. F. Acevedo, "Manufacturing Functional Polymer Surfaces by Direct Laser Interference Patterning (DLIP): A Polymer Science View," Nanomanufacturing, vol. 2, no. 4, pp. 229–264, Nov. 2022, doi: 10.3390/nanomanufacturing2040015.

[106] A. Vashisth, M. Kowalik, J. C. Gerringer, C. Ashraf, A. C. T. Van Duin, and M. J. Green, "ReaxFF Simulations of Laser-Induced Graphene (LIG) Formation for Multifunctional Polymer Nanocomposites," ACS Appl Nano Mater, vol. 3, no. 2, pp. 1881–1890, Feb. 2020, doi: 10.1021/acsanm.9b02524.

[107] S. J. Kim, K. Choi, B. Lee, Y. Kim, and B. H. Hong, "Materials for Flexible, Stretchable Electronics: Graphene and 2D Materials," Annu Rev Mater Res, vol. 45, pp. 63–84, Jul. 2015, doi: 10.1146/annurev-matsci-070214-020901.

[108] Y. Shao, J. Li, Y. Li, H. Wang, Q. Zhang, and R. B. Kaner, "Flexible quasi-solid-state planar micro-supercapacitor based on cellular graphene films," Mater Horiz, vol. 4, no. 6, pp. 1145–1150, Nov. 2017, doi: 10.1039/c7mh00441a.

[109] W. Wang et al., "A Highly Stretchable Microsupercapacitor Using Laser-Induced Graphene/NiO/Co3O4 Electrodes on a Biodegradable Waterborne Polyurethane Substrate," Adv Mater Technol, vol. 5, no. 2, Feb. 2020, doi: 10.1002/admt.201900903.

[110] F. Vivaldi et al., "Sweat analysis with a wearable sensing platform based on laser-induced graphene," APL Bioeng, vol. 6, no. 3, Sep. 2022, doi: 10.1063/5.0093301.

[111] A. Dallinger, K. Keller, H. Fitzek, and F. Greco, "Stretchable and Skin-Conformable Conductors Based on Polyurethane/Laser-Induced Graphene," ACS Appl Mater Interfaces, vol. 12, no. 17, pp. 19855–19865, Apr. 2020, doi: 10.1021/acsami.0c03148.

[112] R. You, Y. Q. Liu, Y. L. Hao, D. D. Han, Y. L. Zhang, and Z. You, "Laser Fabrication of Graphene-Based Flexible Electronics," Advanced Materials, vol. 32, no. 15, Apr. 2020, doi: 10.1002/adma.201901981.

[113] C. Mu et al., "High-performance flexible all-solid-state micro-supercapacitors based on two-dimensional InSe nanosheets," J Power Sources, vol. 482, Jan. 2021, doi: 10.1016/j.jpowsour.2020.228987.

[114] D. W. Boukhvalov et al., "The advent of indium selenide: Synthesis, electronic properties, ambient stability and applications," Nanomaterials, vol. 7, no. 11. MDPI AG, Nov. 01, 2017. doi: 10.3390/nano7110372.

[115] G. Han, Z. G. Chen, J. Drennan, and J. Zou, "Indium selenides: Structural characteristics, synthesis and their thermoelectric performances," Small, vol. 10, no. 14. Wiley-VCH Verlag, pp. 2747–2765, Jul. 23, 2014. doi: 10.1002/smll.201400104.

[116] Q. Hao et al., "Surface-Modified Ultrathin InSe Nanosheets with Enhanced Stability and Photoluminescence for High-Performance Optoelectronics," ACS Nano, vol. 14, no. 9, pp. 11373–11382, Sep. 2020, doi: 10.1021/acsnano.0c03556.

[117] H. Pan et al., "Broadband Nonlinear Optical Response of InSe Nanosheets for the Pulse Generation from 1 to 2 μm," ACS Appl Mater Interfaces, vol. 11, no. 51, pp. 48281–48289, Dec. 2019, doi: 10.1021/acsami.9b18632.

[118] G. Han, Z. G. Chen, J. Drennan, and J. Zou, "Indium selenides: Structural characteristics, synthesis and their thermoelectric performances," Small, vol. 10, no. 14. Wiley-VCH Verlag, pp. 2747–2765, Jul. 23, 2014. doi: 10.1002/smll.201400104.

[119] Y. Liao, Y. Shan, L. Wu, Y. Xiang, and X. Dai, "Liquid-Exfoliated Few-Layer InSe Nanosheets for Broadband Nonlinear All-Optical Applications," Adv Opt Mater, vol. 8, no. 9, May 2020, doi: 10.1002/adom.201901862.

[120] H. Li et al., "Liquid phase exfoliation of indium selenide: Achieving the optimum exfoliating parameters and unraveling the mechanism,"

Progress in Natural Science: Materials International, vol. 32, no. 6, pp. 700–704, Dec. 2022, doi: 10.1016/j.pnsc.2022.10.006.

[121] J. Kang et al., "Solution-Based Processing of Optoelectronically Active Indium Selenide," Advanced Materials, vol. 30, no. 38, Sep. 2018, doi: 10.1002/adma.201802990.

[122] Y. Liao, Y. Shan, L. Wu, Y. Xiang, and X. Dai, "Liquid-Exfoliated Few-Layer InSe Nanosheets for Broadband Nonlinear All-Optical Applications," Adv Opt Mater, vol. 8, no. 9, May 2020, doi: 10.1002/adom.201901862.

[123] S. A. Evlashin et al., "Ambient Condition Production of High Quality Reduced Graphene Oxide," Adv Mater Interfaces, vol. 5, no. 18, Sep. 2018, doi: 10.1002/admi.201800737.

[124] R. K. Singh, R. Kumar, and D. P. Singh, "Graphene oxide: Strategies for synthesis, reduction and frontier applications," RSC Advances, vol. 6, no. 69. Royal Society of Chemistry, pp. 64993–65011, 2016. doi: 10.1039/c6ra07626b.

[125] A. C. Ferrari and J. Robertson, "Interpretation of Raman spectra of disordered and amorphous carbon," Phys Rev B Condens Matter, vol. 61, no. 20, pp. 14095–-14107, 2000, doi: https://doi.org/10.1103/physrevb.61.14095.

[126] X. Díez-Betriu et al., "Raman spectroscopy for the study of reduction mechanisms and optimization of conductivity in graphene oxide thin films," J Mater Chem C Mater, vol. 1, no. 41, pp. 6905–6912, Nov. 2013, doi: 10.1039/c3tc31124d.

[127] Z. Ni, Y. Wang, T. Yu, and Z. Shen, "Raman spectroscopy and imaging of graphene," Nano Res, vol. 1, no. 4, pp. 273–291, Oct. 2008, doi: 10.1007/s12274-008-8036-1.

[128] D. L. Silva et al., "Raman spectroscopy analysis of number of layers in mass-produced graphene flakes," Carbon N Y, vol. 161, pp. 181–189, May 2020, doi: 10.1016/j.carbon.2020.01.050.

[129] A. Velasco et al., "Recent trends in graphene supercapacitors: From large area to microsupercapacitors," Sustainable Energy and Fuels,

vol. 5, no. 5. Royal Society of Chemistry, pp. 1235–1254, Mar. 07, 2021. doi: 10.1039/d0se01849j.

[130] P. Mustarelli, E. Quartarone, C. Tomasi, and A. Magistris, "New materials for polymer electrolytes," 2000. [Online]. Available: www.elsevier.com/locate/ssi

[131] Z. Peng, J. Lin, R. Ye, E. L. G. Samuel, and J. M. Tour, "Flexible and stackable laser-induced graphene supercapacitors," ACS Appl Mater Interfaces, vol. 7, no. 5, pp. 3414–3419, Feb. 2015, doi: 10.1021/am509065d.

[132] P. Zaccagnini and A. Lamberti, "A perspective on laser-induced graphene for micro-supercapacitor application," Appl Phys Lett, vol. 120, no. 10, Mar. 2022, doi: 10.1063/5.0078707.

[133] M. Liu, J. N. Wu, and H. Y. Cheng, "Effects of laser processing parameters on properties of laser-induced graphene by irradiating CO2 laser on polyimide," Sci China Technol Sci, vol. 65, no. 1, pp. 41–52, Jan. 2022, doi: 10.1007/s11431-021-1918-8.

[134] A. Kaidarova, M. T. Vijjapu, K. Telegenov, A. Przybysz, K. N. Salama, and J. Kosel, "Enhanced Graphene Sensors via Multi-Lasing Fabrication," IEEE Sens J, vol. 21, no. 17, pp. 18562–18570, Sep. 2021, doi: 10.1109/JSEN.2021.3088348.

[135] "Raman spectroscopy as a versatile tool for studying the properties of graphene".

[136] K. Muzyka and G. Xu, "Laser-induced Graphene in Facts, Numbers, and Notes in View of Electroanalytical Applications: A Review," Electroanalysis, vol. 34, no. 4. John Wiley and Sons Inc, pp. 574–589, Apr. 01, 2022. doi: 10.1002/elan.202100425.

[137] J. B. Lee, J. Jang, H. Zhou, Y. Lee, and J. Bin In, "Densified laser-induced graphene for flexible microsupercapacitors," Energies (Basel), vol. 13, no. 24, Dec. 2020, doi: 10.3390/en13246567.

[138] A. Lamberti et al., "All-SPEEK flexible supercapacitor exploiting Laser-induced graphenization," 2d Mater, vol. 4, no. 3, Sep. 2017, doi: 10.1088/2053-1583/aa790e.

[139] E. Ghoniem, S. Mori, and A. Abdel-Moniem, “Low-cost flexible supercapacitors based on laser reduced graphene oxide supported on polyethylene terephthalate substrate,” J Power Sources, vol. 324, pp. 272–281, Aug. 2016, doi: 10.1016/j.jpowsour.2016.05.069.

[140] B. S. de Lima, M. I. B. Bernardi, and V. R. Mastelaro, “Wavelength effect of ns-pulsed radiation on the reduction of graphene oxide,” Appl Surf Sci, vol. 506, Mar. 2020, doi: 10.1016/j.apsusc.2019.144808.

[141] M. J. Low et al., “Laser-induced reduced-graphene-oxide micro-optics patterned by femtosecond laser direct writing,” Appl Surf Sci, vol. 526, Oct. 2020, doi: 10.1016/j.apsusc.2020.146647.

[142] S. J. Yang, T. Kim, H. Jung, and C. R. Park, “The effect of heating rate on porosity production during the low temperature reduction of graphite oxide,” Carbon N Y, vol. 53, pp. 73–80, Mar. 2013, doi: 10.1016/j.carbon.2012.10.032.

[143] Wei. Lei, Xiaobing. Zhang, Zhiwei. Zhao, and C. NANOcarbon (2010 : Nanjing Shi, Proceedings 2010 8th International Vacuum Electron Sources Conference and NANOcarbon : October 14-16, 2010, Nanjing, China. IEEE, 2010.

[144] L. Stobinski et al., “Graphene oxide and reduced graphene oxide studied by the XRD, TEM and electron spectroscopy methods,” J Electron Spectros Relat Phenomena, vol. 195, pp. 145–154, 2014, doi: 10.1016/j.elspec.2014.07.003.

[145] D. Bhattacharjya, C. H. Kim, J. H. Kim, I. K. You, J. Bin In, and S. M. Lee, “Fast and controllable reduction of graphene oxide by low-cost CO 2 laser for supercapacitor application,” Appl Surf Sci, vol. 462, pp. 353–361, Dec. 2018, doi: 10.1016/j.apsusc.2018.08.089.

[146] A. L. Patterson, “The Scherrer Formula for I-Ray Particle Size Determination,” 1939.

[147] H. R. Naderi, P. Norouzi, M. R. Ganjali, and H. Gholipour-Ranjbar, “Synthesis of a novel magnetite/nitrogen-doped reduced graphene oxide nanocomposite as high performance supercapacitor,” Powder

Technol, vol. 302, pp. 298–308, Nov. 2016, doi: 10.1016/j.powtec.2016.08.054.

[148] Y. L. Zhang, L. Guo, H. Xia, Q. D. Chen, J. Feng, and H. B. Sun, "Photoreduction of Graphene Oxides: Methods, Properties, and Applications," Adv Opt Mater, vol. 2, no. 1, pp. 10–28, Jan. 2014, doi: 10.1002/adom.201300317.

[149] X. Cai, X. Shen, L. Ma, Z. Ji, and L. kong, "Facile synthesis of nickel–cobalt sulfide/reduced graphene oxide hybrid with enhanced capacitive performance," RSC Adv, vol. 5, no. 72, pp. 58777–58783, 2015, doi: 10.1039/c5ra09447j.

[150] R. Arul, R. N. Oosterbeek, J. Robertson, G. Xu, J. Jin, and M. C. Simpson, "The mechanism of direct laser writing of graphene features into graphene oxide films involves photoreduction and thermally assisted structural rearrangement," Carbon N Y, vol. 99, pp. 423–431, Apr. 2016, doi: 10.1016/j.carbon.2015.12.038.

[151] X. Mao et al., "The preparation and characteristic of poly (3,4-ethylenedioxythiophene)/reduced graphene oxide nanocomposite and its application for supercapacitor electrode," Materials Science and Engineering: B, vol. 216, pp. 16–22, Feb. 2017, doi: 10.1016/j.mseb.2016.10.002.

Annexes

Publications

- ✓ A. Velasco, Y. K. Ryu, A. Hamada, A. de Andrés, F. Calle, and J. Martinez. "Laser-Induced Graphene Microsupercapacitors: Structure, Quality, and Performance". Nanomaterials, vol. 13, no. 5, Mar. 2023, doi: 10.3390/nano13050788.
- ✓ M. B. Gómez-Mancebo, R. Fernández-Martínez, A. Ruiz-Perona, V. Rubi, P. Bastante, F. García-Pérez, F. Borlaf, M. Sánchez, A. Hamada, A. Velasco, Y. K. Ryu, F. Calle, L. J. Bonales, A. J. Quejido, J. Martínez, and I. Rucandio. "Comparison of Thermal and Laser-Reduced Graphene Oxide Production for Energy Storage Applications". Nanomaterials, vol. 13, no. 8, Apr. 2023, doi: 10.3390/nano13081391.

- A. Martinez Barja, Y. K. Ryu, S. Tarancón, E. Tejada, A. Hamada, A. Velasco, J. Martinez." Laser Induced Graphene Strain Sensors for Body Movement Monitoring". Under review in ACS Omega.
- A. Hamada, Y. K. Ryu, A. Velasco, M. B. Gómez-Mancebo, S. Fernandez Carretero, F. Calle, J. Martinez." Double Pass Effect on Laser Induced Graphene Microsupercapacitors" Manuscript to be submitted to Applied Surface Science. (Under Preparation).

Conferences

- ✓ 14th Spanish Conference on Electronic Devices (CED 2023). Valencia, from 6th to 8th of June of 2023. Poster presentation. "Laser-Induced Graphene Flexible MicroSupercapacitors."

Activities

- ✓ European Night of Researchers (2021, Madrid)

- ✓ Science and Innovation Week (2021, Madrid).
- ✓ International Women's Day and the Girl in Science Under the slogan “From Argelia to Madrid our Ph.D. travel discovering graphene for a sustainable world”.
- ✓ European Night of Researchers (30th September 2022, Madrid).
- ✓ Science and Innovation Week (11th November 2022, Madrid)